

Calibration of a Field Spectroradiometer

Calibration and Characterization of a Non-Imaging Field Spectroradiometer Supporting Imaging Spectrometer Validation and Hyperspectral Sensor Modelling

Dissertation

zur

**Erlangung der naturwissenschaftlichen Doktorwürde
(Dr. sc. nat.)**

vorgelegt der

**Mathematisch-naturwissenschaftlichen Fakultät
der
Universität Zürich**

von

Michael Ellert Schaepman

von

Zürich / ZH

Begutachtet von
Prof. Dr. Klaus I. Itten

Zürich 1998

Die vorliegende Arbeit wurde von der Mathematisch–naturwissenschaftlichen Fakultät der Universität Zürich auf Antrag von Prof. Dr. Klaus I. Itten und Prof. Dr. Harold Haefner als Dissertation angenommen.

Summary

Spectroradiometry is the technology to measure the power of optical radiation in narrow wavelength intervals. Spectroradiometric measurement equipment plays a key role in the quantitative measurement of contiguous spectral radiance and irradiance in remote sensing. The direct and indirect identification of surface constituents using quantitative descriptors relies on the associated uncertainties of the involved measurement equipment and the geophysical algorithms.

Well calibrated measurement equipment includes a characterization process, describing the instruments behaviour with respect to the arriving photons, and the calibration reports on the traceability of the measurements to a predefined standard.

The laboratory characterization of a ground based spectroradiometer is based on a measurement plan for a $\leq 10\%$ uncertainty calibration. The individual steps include the characterization for measures such as the signal to noise ratio, the noise equivalent signal, the dark current, the wavelength calibration, the spectral sampling interval, the nonlinearity, directional and positional effects, spectral scattering, determination of the field of view, polarization, size-of-source effect, and the temperature dependence of these measurements.

The traceability of the radiance calibration is established to a secondary NIST (National Institute of Standards and Technology, USA) calibration standard using a 95% confidence interval and defines an expanded uncertainty. This results in a measurement uncertainty of less than $\pm 7.1\%$ for all radiometer channels.

The field characterization includes the characterization procedures of the laboratory calibration, but also defines the short-term variations of the atmosphere and the sun as a natural illumination source. The traceability of the reflectance measurements is again traced to NIST reflectance values using a Spectralon reference panel. Assuming short-term atmospheric changes to be 0.1%, the expanded uncertainty is well below $\pm 6.2\%$ for most of the channels. A more realistic scenario agrees on 2% short-term variations of the atmosphere and therefore assigns a higher uncertainty of maximum $\pm 7.3\%$ for the traceability to NIST using a 95% confidence interval. Reflectance measurements eliminate most of the systematic errors so that the total uncertainty remains below the radiance calibration uncertainty.

Reflectance measurements are an important input parameter for use with radiative transfer codes in support of vicarious calibration experiments. These experiments require in addition the proper characterization of the atmosphere to validate and possibly update the laboratory calibration of an imaging spectrome-

ter. In the case of the presented DAIS 7915 overflight in Switzerland in the years 1996 and 1997, a complete ground measurement plan is presented and the sampling strategy discussed.

Using the previously gained knowledge about relevant calibration processes and their associated uncertainties, as well as performing an experiment under real conditions, contributes to the formulation of a new basis for an airborne imaging spectrometer concept—namely APEX—in support of the calibration, validation, and application development of the future ESA Land Surface Processes Interactions Mission called PRISM. The concept includes a radiometric performance analysis as well as a sensor model to evaluate the respective figures of merit.

The calibration effort has been underestimated or even been neglected for a long time. The scientific value of imaging spectroscopy data is not only in direct proportion to the development in sensor technology in general, but also in the calibration effort. It has been proven that the introduction of the uncertainty measure to ground based spectroradiometric measurements significantly increases the reliability of the measured data.

Zusammenfassung (German)

Mit spektoradiometrischen Messungen kann die Energie optischer Strahlung in kleinen Wellenlängenintervallen erfasst werden. Spektoradiometer spielen in der Fernerkundung eine wesentliche Rolle in der quantitativen Analyse der spektralen Einstrahlung. Die Möglichkeit, direkte und indirekte Identifikation von Oberflächenmaterialien durchzuführen, ist von der Messgenauigkeit der verwendeten Instrumente und den entsprechenden geophysikalischen Algorithmen abhängig. Gut kalibrierte Messinstrumente, welche bezüglich ihrer Eigenschaft als Photonen-zähler charakterisiert worden sind und auch entsprechend kalibriert wurden, ermöglichen eine Rückführung der Messungen auf einen vordefinierten Referenzstandard.

Die im Labor durchgeführte Charakterisierung des verwendeten Spektoradiometers basiert auf dem Messplan mit einer erwarteten Kalibrationsgenauigkeit von $\pm 10\%$. Die im Einzelnen durchgeführten Charakterisierungsschritte schließen die Untersuchung folgender Größen mit ein: das Signal-Rausch-Verhalten, das dem Rauschen entsprechende Signal, den Dunkelstrom, die Wellenlängenkalibration, das spektrale Auflösungsvermögen, die Nichtlinearitäten, direktionale sowie positionale Effekte, Streueffekte, die Bestimmung des räumlichen Öffnungswinkels, die Polarisierung, die Größenabhängigkeit der Beleuchtungsquelle, sowie die Temperaturempfindlichkeit.

Die Rückführung der Laborkalibration wurde auf einen sekundären Standard, welcher durch das NIST (National Institute of Standards and Technology, USA) zertifiziert wurde, mit einem Vertrauensintervall von 95% etabliert. Die

Unsicherheiten betragen dabei weniger als $\pm 7.1\%$ für alle Spektrometerkanäle.

Die Kalibrierung für die Feldmessungen basiert auf der oben erwähnten Laborcharakterisierung, bezieht sich aber auf die Sonne als natürliche Beleuchtungsquelle und berücksichtigt dabei die kurzzeitig auftretenden atmosphärischen Schwankungen. Auch hier wird mit einem Reflektanzstandard (Spectralon) gearbeitet, der die Rückführung auf den NIST-Standard gewährleistet. Betragen die kurzzeitigen atmosphärischen Schwankungen innerhalb einer Messung 0.1% , resultiert daraus eine Messunsicherheit von weniger als $\pm 6.2\%$ für alle Kanäle des Spektrometers. Eine realistischere Annahme der atmosphärischen Schwankungen im Bereich von 2% erhöht die Unsicherheiten auf $\pm 7.3\%$, jeweils in einem Vertrauensintervall von 95% . Reflektanzmessungen eliminieren die meisten systematischen (Mess)Fehler, so dass die im Feld auftretenden Unsicherheiten kleiner als die der absoluten Strahlungskalibrierung im Labor sind.

Reflektanzmessungen, die im Feld durchgeführt werden, sind wichtige Eingangsgrößen für die Kalibrierung von abbildenden Spektrometern. Die Messungen erfordern zusätzlich eine sorgfältige Charakterisierung der Atmosphäre damit beim Überfliegen die vorgängige Laborkalibrierung des abbildenden Spektrometers validiert und aufdatiert werden kann. Mit den Befliegungen des abbildenden Spektrometers DAIS 7915 in der Schweiz 1996 und 1997 werden derartige Validierungsexperimente vorgestellt. Zusätzlich werden die Datenerhebungsstrategie und die Modellierung der Reflektanzmessungen am Boden unter Berücksichtigung der Atmosphäre bis zur Höhe des Sensors diskutiert.

Basierend auf den Erkenntnissen der Labor- und Felderkalibrierung sowie dem Validierungsexperiment wird ein Sensormodell für ein neues, abbildendes Spektrometer APEX (Airborne PRISM Experiment) entwickelt. APEX dient nach seiner Fertigstellung der Unterstützung der Kalibration, der Validierung und der Anwendungsentwicklung einer zukünftigen ESA Mission (LSPIM, Land Surfaces Processes and Interactions Mission), welche unter dem Namen PRISM (Processes Research of an Imaging Space Mission) realisiert wird. Das entwickelte Sensormodell beruht auf realistischen Eingangsgrößen des zu erwartenden Strahlenhaushaltes sowie auf der Evaluation der radiometrischen Leistung dieses Instrumentes.

Kalibrationsanstrengungen im Zusammenhang mit tragbaren Bodenspektroradiometern wurden lange Zeit unterschätzt oder sogar vernachlässigt. Der wissenschaftliche Wert von abbildenden Spektrometerdaten ist aber sowohl direkt vom technischen Fortschritt, als auch von der Kalibrationsgenauigkeit abhängig. Es konnte gezeigt werden, dass die Charakterisierung des Bodenspektroradiometers und dessen Messunsicherheiten die Zuverlässigkeit der gemessenen Daten signifikant verbessert und damit einen Beitrag an die zuverlässige Validierung und Modellierung von abbildenden Spektrometern liefert.

Table of Contents

Summary.....	I
Table of Contents.....	V
List of Figures.....	IX
List of Tables.....	XIII
Chapter 1: Introduction and Problem Description	
1.1 Introduction.....	1
1.2 Problem Description.....	2
1.3 The Structure of this Study.....	3
Chapter 2: Spectroradiometry	
2.1 Introduction.....	5
2.2 The Measurement Equation.....	8
2.3 Absolute and Relative Measurements.....	8
2.4 Sources of Uncertainty.....	9
Chapter 3: Spectroradiometric Measurement Equipment	
3.1 Introduction.....	11
3.2 Evaluation Criteria for a Field Spectroradiometer.....	11
3.3 The GER3700 Instrument.....	14
3.3.1 Technical Description.....	14
3.3.2 Major Measurement Campaigns and Use.....	16
3.4 Other Supporting Equipment.....	18
Chapter 4: Laboratory Calibration	
4.1 Introduction.....	23
4.2 Selection of a Calibration Strategy.....	23
4.2.1 Introduction.....	23
4.2.2 The Measurement Plan.....	24
4.3 Calibration Standards.....	26
4.3.1 Spectral Irradiance and Radiance Standards.....	27
4.3.2 Integrating Sphere Calibration Standard.....	27
4.4 Wavelength Standards.....	30
4.5 Selection and Characterization of the Measurement Setup.....	31
4.5.1 Selection of Instrument Parameters.....	31
4.5.2 Measurement Setup.....	31
4.6 Characterization Process.....	32

4.6.1	Signal to Noise Ratio.....	32
4.6.2	Noise Equivalent Signal (NES) and Noise Equivalent Radiance (NER)	35
4.6.3	Dark Current or Dark Signal.....	36
4.6.4	Wavelength Calibration and Spectral Sampling Interval.....	38
4.6.5	Nonlinearity	46
4.6.6	Directional and Positional Effects	51
4.6.7	Spectral Scattering	51
4.6.8	Field of View (FOV).....	53
4.6.9	Polarization	56
4.6.10	Size-of-Source Effect.....	64
4.6.11	Temperature	64

Chapter 5: Field Reflectance Spectroradiometry

5.1	Introduction.....	69
5.2	Measurement of Reflectance	69
5.3	Field Standards	71
5.3.1	Spectralon Reflectance Standard.....	72
5.3.2	Other Field Standards	74
5.4	Measurement Plan.....	75
5.5	Reflectance Measurement	75
5.5.1	Sampling Strategy.....	77
5.6	Performing the Measurement.....	78

Chapter 6: Calibration Uncertainty Estimation

6.1	Uncertainty in Spectroradiometric Measurements	79
6.1.1	Introduction.....	79
6.1.2	Determination of Uncertainty in Spectroradiometry.....	81
6.2	Laboratory Calibration Uncertainty.....	82
6.2.1	Uncertainty Report	82
6.3	Absolute Radiance Calibration	85
6.3.1	Linear Calibration Model	85
6.3.2	Temperature Dependent Calibration Model	85
6.4	Absolute Reflectance Calibration.....	87
6.4.1	Uncertainty Report	87
6.5	Conclusions.....	91

Chapter 7: Vicarious Calibration

7.1	Introduction.....	93
7.2	Vicarious Calibration	94
7.3	Vicarious Calibration Experiment (Reflectance Based Approach).....	95
7.3.1	Experiment Description	95
7.3.2	Modelling the At-Sensor-Radiance.....	99

Chapter 8: APEX – Airborne PRISM Experiment

8.1	Introduction.....	103
8.2	The Airborne PRISM Experiment.....	103
8.3	APEX – The Instrument.....	104
8.3.1	The Imaging Spectrometer Optomechanical Subsystem	105
8.3.2	Detectors and Front End Electronics.....	106

Table of Contents

8.3.3	Electronics Unit.....	107
8.3.4	Auxiliary Components.....	108
8.3.5	The Aircraft and Navigation.....	108
8.3.6	The Calibration.....	108
8.3.7	Data Handling	110
8.3.8	Operationalization	111
8.4	Radiometric Specifications for APEX.....	111
8.4.1	Introduction.....	111
8.4.2	Specifications.....	112
8.5	Radiometric Modelling of At–Sensor–Radiances	112
8.5.1	PRISM Specifications	112
8.5.2	Selection of Radiative Transfer Code and Model Comparison.....	113
8.5.3	Input Parameters for the APEX Model.....	114
8.6	Determination of SNR and NE Δr for APEX.....	116
8.7	Conclusions.....	120
Chapter 9: Conclusions and Outlook		
9.1	Conclusions.....	123
9.2	Outlook.....	124
Glossary.....		127
Appendix		131
References.....		137
Acknowledgements.....		145

List of Figures

Figure 2.1:	Contributing sources to a spectroradiometric measurement.....	6
Figure 2.2:	Three different measurement modi for spectroradiometers [97].	7
Figure 3.1:	GER3700 spectroradiometer mounted on a tripod with laptop computer, batteries and Spectralon reflectance standard.....	15
Figure 3.2:	Center wavelength and FWHM of the GER3700 as provided by the manufacturer [35].....	16
Figure 3.3:	Sun-photometer during Langley-calibration.	19
Figure 3.4:	The FIGOS (Field Goniometer System) in operation on a soccer field.	20
Figure 4.1:	Integrating sphere calibration setup with spectroradiometer attached.....	28
Figure 4.2:	Color temperature calibration values for the integrating sphere [64].	28
Figure 4.3:	Integrating sphere NIST calibrated spectral radiance [64].....	30
Figure 4.4:	Three types of measurement setups for the characterization process.	32
Figure 4.5:	SNR determination using 200 fL luminance setting.	34
Figure 4.6:	SNR determination using 2200 fL luminance setting.	34
Figure 4.7:	NES and NER for the GER3700 spectroradiometer.	36
Figure 4.8:	Dark current (bottom) and lowest measured signal (upper).	37
Figure 4.9:	Spectral resolution, spectral sampling interval, FWHM, and center wavelength of a Gaussian response function.....	38
Figure 4.10:	Tunable dye laser setup for the wavelength calibration.....	40
Figure 4.11:	Tunable dye laser laboratory setup: cavity (top) and spectrometer (bottom).....	41
Figure 4.12:	Spectroradiometer response to a dye laser line at 593.6 nm.	41
Figure 4.13:	Differences between laser and spectroradiometer center wavelength.....	42
Figure 4.14:	Extrapolation of center wavelengths to the Si detector.....	43
Figure 4.15:	Gaussian fit and FWHM determination for 593.6 nm.....	44
Figure 4.16:	Center wavelength and FWHM for selected channels.	45
Figure 4.17:	Original and calibrated FWHM (y-axis) and center wavelengths (x-axis) for each spectroradiometer channel.....	46
Figure 4.18:	Linear (75–6700 fL) and non-linear regions (< 75 and > 6700 fL) for one selected channel (568 nm).....	47
Figure 4.19:	Comparison of NIST radiance values [64], calibration radiances and modeled Spectralon [53] radiances	48
Figure 4.20:	Linearity fit and residuals within the predefined calibration range of the spectroradiometer.	49
Figure 4.21:	Nonlinearity correction factor within the calibration range.....	50
Figure 4.22:	Geometric relations of the field-of-view for a fixed-focus spectroradiometer.	54
Figure 4.23:	Measurement of FOV and the corresponding linear fit.....	56
Figure 4.24:	Polarization measurement setup.	59

Figure 4.25:	Apparent transmittance of a polarizer at 649.4 nm.....	63
Figure 4.26:	Polarization sensitivity and polarization dependent loss.	63
Figure 4.27:	Radiometer temperature readings for three experiments: heat once, cool down passive (cool); heat once, cool down active (burst); and heat and cool three times (sine).....	66
Figure 4.28:	Temperature fit for three selected PbS1 detector channels.....	67
Figure 4.29:	Offset values for temperature model in the PbS1 detector.....	68
Figure 5.1:	Percentual change of atmospheric transmittance over time in three selected wavelengths (410 nm, 670 nm, and 940 nm).....	71
Figure 5.2:	Differences of a perfect lambertian assumption (100% reflector) and the Spectralon reference standard.....	72
Figure 5.3:	NIST calibrated Spectralon 8° hemispherical reflectance factor [53]..	74
Figure 5.4:	Field reflectances of different objects under solar illumination in comparison with Spectralon reflectance.	75
Figure 5.5:	Calibrated absolute reflectance spectrum of an artificial blue coating.	78
Figure 6.1:	Calibration gain and calibration offset for all 704 GER3700 spectroradiometer channels.	86
Figure 6.2:	Comparison of temperature calibrated (according to eq. (6.11)) and uncalibrated radiance calibration (according to eq. (6.10)) at the detector transition zone.	86
Figure 6.3:	NIST calibrated field reflectance spectrum using a 95% confidence interval.....	90
Figure 6.4:	Uncertainty change at 2200 nm of the NIST calibrated reflectance spectrum.....	90
Figure 7.1:	DAIS 7915 vicarious calibration site in Central Switzerland (Thermal IR left image, VIS right image).	96
Figure 7.2:	Corresponding spectral signatures to the objects listed in Figure 7.1.....	97
Figure 7.3:	Artificial green soccer field covered with quartz sand measured in the two calibration campaigns.	98
Figure 7.4:	Green soccer field measured in two different calibration campaigns.	98
Figure 7.5:	Four modeling approaches for the prediction of at-sensor- radiance of the DAIS 7915 in selected spectral channels [91].	100
Figure 7.6:	Comparison of DAIS calibrated radiance data and MODTRAN predicted at-sensor-radiance of an artificial green soccer field [111].	100
Figure 7.7:	Percent deviation of the comparison in Figure 7.6, omitting bands with a SNR < 5 [111].	100
Figure 7.8:	Partial DAIS 7915 scene (recorded August 9, 1997) over Central Switzerland (VIS left image, thermal IR right image; data processing courtesy by P. Strobl, DLR).....	101
Figure 8.1:	Schematic APEX block diagram [44].	105
Figure 8.2:	APEX instrument layout (visualization courtesy OIP n.v.) [28].	106
Figure 8.3:	PRISM radiometric specifications for minimum, typical and maximum at-sensor-radiances (solid dots indicate modeling points) [55].....	113
Figure 8.4:	Comparison of 6S and MODTRAN radiative transfer codes using equivalent input parameters.	114

List of Figures

Figure 8.5:	Differences between 6S and MODTRAN in the 1.9–2.5 μm region using the same atmospheric conditions and a constant albedo of 0.4.	114
Figure 8.6:	APEX radiometric specifications for minimum, validation and maximum at-sensor-radiances.	115
Figure 8.7:	Comparison of PRISM [55] and APEX radiometric specifications at the typical, validation and minimum levels.	116
Figure 8.8:	Comparison of PRISM [55] and APEX radiometric specifications at the maximum level.	116
Figure 8.9:	SNR for all APEX channels for the maximum, validation and minimum levels.	119
Figure 8.10:	$NE\Delta\rho$ for each APEX channel.	119
Figure 8.11:	Digital numbers (or grey levels) for the three specified radiance levels.	120

List of Tables

Table 3.1:	RSL specifications for the spectroradiometer evaluation (n.s. = not specified by RSL for evaluation).	12
Table 3.2:	GER3700 factory specifications [35].	14
Table 3.3:	Major measurement campaigns using the GER3700 spectroradiometer (1995–1998) (n.a. = no literature available).	16
Table 4.1:	Measurement plan for the GER3700 spectroradiometer (Adapted following [50]).	25
Table 4.2:	Properties of integrating sphere calibration standard [63].	29
Table 4.3:	Average SNR over all detector channels.	35
Table 4.4:	Corresponding noise-to-signal of the SNR measurements.	35
Table 5.1:	Properties of Spectralon reflectance material [54].	73
Table 5.2:	Measurement Plan for the GER3700 in Field Measurements.	76
Table 6.1:	Uncertainties for a $\leq 10\%$ laboratory calibration of the GER3700 spectroradiometer at 200 fL.	83
Table 6.2:	Combined uncertainty for the GER3700 spectroradiometer.	84
Table 6.3:	Expanded uncertainty for the GER3700 spectroradiometer ($k=2$).	84
Table 6.4:	Expanded uncertainty for the GER3700 spectroradiometer using a 95% confidence interval.	84
Table 6.5:	GER3700 spectroradiometer laboratory calibration uncertainty.	84
Table 6.6:	Uncertainties for a field reflectance calibration of the GER3700 spectroradiometer.	87
Table 6.7:	Combined uncertainty for the GER3700 spectroradiometer.	88
Table 6.8:	Expanded uncertainty for the GER3700 spectroradiometer ($k=2$).	89
Table 6.9:	Expanded uncertainty for the GER3700 spectroradiometer using a 95% confidence interval.	89
Table 6.10:	Field calibration uncertainties of the GER3700 spectroradiometer for three different atmospheric conditions including the Spectralon uncertainty for higher wavelengths.	89
Table 6.11:	Suggested figures for the comparison of field spectroradio- meters.	92
Table 7.1:	Ground equipment for two validation experiments in Central Switzerland.	95
Table 8.1:	Processing levels of the APEX processing and archiving facility (PAF) [28].	110
Table 8.2:	Initial APEX specifications [28].	112
Table 8.3:	Average SNR for each detector and level.	118
Table 8.4:	Average for each Detector and Level	118
Table A.1:	DAIS characteristics (radiometric).	133
Table A.2:	DAIS characteristics (spatial).	133
Table A.3:	APEX atmospheric model input parameter.	134
Table A.4:	PRISM atmospheric model input parameter.	134
Table A.5:	APEX sensor model input parameter.	135

Chapter 1:

Introduction and Problem Description

1.1 Introduction

Spectroradiometry is the technology of measuring the power of optical radiation in narrow wavelength intervals. Spectroradiometric measurements have played a key role in the development of the quantum theory. The intrinsic lineshapes of spectra are defined by complex processes on the atomic or molecular level. These processes include dephasing phenomena, vibrational and rotational effects of molecules, and Doppler effects in molecular spectra among others.

The consistent reproduction of such complex phenomena depends closely on high quality measurement instrumentation. Difficulties associated with such measurements are strongly dependent on the presence of high technology measurement equipment and appropriate calibration strategies. Reliable measurement of spectroradiometric quantities is still fraught with difficulties and calibration issues remain unsatisfactorily resolved.

The measurement of contiguous spectral radiance and irradiance in remote sensing helps to directly and indirectly identify surface constituents. The quantitative characterization of these constituents is the goal of spectroradiometry in remote sensing.

By measuring the upwelling spectral radiance from any spatial extent on the earth's surface, direct or indirect detection and identification of the surface material can be made using the specific molecular absorption features present in the spectra. The superimposing of atmospheric effects in field measured spectra increases the complexity of these features and thus the difficulty to explain them.

Another dimension of complexity is introduced from extrapolating the non-imaging ground sampling technique to a contiguous coverage of the surface. Imaging spectrometers acquire data in hundreds of contiguous spectra in adjacent pixels and lines. The spatial extent of the recorded constituents by imaging spectrometers helps to build quantitative distribution maps of the earth's surface. This is called the science of imaging spectroscopy. The promise of imaging spectroscopy is to quantitatively characterize the surface by interpreting these measured spectra. Without appropriate methods to relate measured photon

quantities to radiance values, however, these data enjoy minimal scientific utility. Methods relating these quantities include the calibration process to link these recorded photons as electrons to radiometric quantities expressed in SI units.

1.2 Problem Description

Calibration for non-imaging ground spectroradiometers has not been satisfactorily solved. The problem discussed within this work is a definition of a laboratory and field calibration strategy helping to reduce model uncertainties of vicarious calibration campaigns and sensor modeling tasks based on predefined field reflectance measurements.

The term calibration is often used as an abbreviation for the complex process of

- **characterizing,**
- **calibrating, and**
- **validating**

the performance of an instrument. The characterization process is the description of the instrument's behavior with respect to the arriving photons. A few characterization terms such as nonlinearity, responsivity, polarization sensitivity among others are responsible for instrument-specific behavior.

The calibration takes such behavior into account, compensates for, or even removes them and establishes ultimately a traceability of the characterized instrument to a predefined standard. These calibration standards can be of the type working-, secondary- or even primary standards. The process of calibration is never able to substitute or compensate for a poor system performance or design. Rather it is the process of introducing the possible sources of errors in the calibration and defining the uncertainties associated with the measurement instrument. In the broadest sense calibration introduces the measure of uncertainty to your data. This introduction of uncertainty is the first problem to be assessed within this work.

Validation addresses the question of reproducibility. Only a characterized, calibrated and validated instrument is of significant value to the scientific user community.

The final goal for spectroradiometric measurements in support of hyperspectral data analysis is to quantitatively derive physical parameters in the reflected part of the electromagnetic spectrum.

Because each calibration process is sensor dependent, a generalized calibration concept does not exist at present and a calibration strategy for each type of sensor must be evaluated from scratch. The final result of the calibration process is a sensor independent signal that can be used for further analysis.

Well characterized and calibrated ground instruments support the successful modeling of at-sensor-radiances of airborne or spaceborne imaging spectrometers. This modeling process relies on the figures of merit of the spectroradiometric

measurement equipment used, as well on the ground equipment in support of the quantification of the spatial, temporal and atmospheric changes. The sampling strategy is always specially adopted for this task. In the case of a simultaneous overflight of an imaging spectrometer, the performance of the imaging spectrometer can be validated, and a radiance or reflectance based vicarious calibration experiment can be carried out. This specific type of experiment supports the validation of the laboratory calibration of the imaging instrument.

Using all previous experience it must finally be proven that a sensor model to derive radiometric specifications for a new, airborne pushbroom imaging spectrometer (namely APEX: Airborne PRISM Experiment) for use as a precursor instrument for the planned Land Surface Processes Interaction Mission (LSPIM) and its space segment called Process Research by an Imaging Space Mission (PRISM) of the European Space Agency (ESA) is feasible.

1.3 The Structure of this Study

This work addresses the problem of development of a calibration process for a ground based spectroradiometer used for remote sensing applications. Many of the problems discussed here can in some way be extrapolated to similar instruments and problems. Some of the experiments carried out throughout this work are state of the art experiments that rely on measurement equipment available only to a limited number of researchers; mainly because of their associated costs. Most of them are, however, well suited to derive representative figures of merit for spectroradiometric measurements.

In Chapter 2 on Spectroradiometry the measurement equation for spectroradiometric applications is defined and the types of measurements and their associated errors in the context of this thesis are discussed.

Before any measurements are taken, an appropriate description of the instrumentation used is provided in the chapter on ‘Spectroradiometric Measurement Equipment’.

The Chapter 4 focuses on calibration in a controlled laboratory environment free of uncertainties introduced by the atmosphere. The chapter on ‘Field Reflectance Spectroradiometry’ on the other hand discusses the calibration of field instruments with the sun as a (natural) illumination source.

The next chapter, Calibration Uncertainty Estimation, discusses the uncertainties associated with both types of calibration and summarizes the uncertainties associated with these measurements. It also states figures of merit for the comparison of ground spectroradiometric measurement equipment.

The use of a well characterized and calibrated spectroradiometer in the validation process of an airborne imaging spectrometer is discussed in the chapter on ‘Vicarious Calibration’. These calibration experiments are carried out in Central Switzerland and are discussed with respect to their validation capabilities.

Based on the experience of the vicarious calibration experiments and the

laboratory calibration of ground spectroradiometric instruments, a new airborne imaging spectrometer is proposed and its radiometric performance assessed in the chapter called 'APEX – Airborne PRISM Experiment'.

Chapter 9 draws conclusions on the results achieved in this work. All useful terms and model input parameters used throughout this book are gathered in the Glossary and the Appendix.

A complete list of the literature cited throughout this work is listed in the last chapter, the References.

Chapter 2:

Spectroradiometry

2.1 Introduction

Radiometry is the measurement of the energy constant of electromagnetic radiation fields and how this energy is transferred from a source, through a medium, to a detector. The result is a measurement in units of power, i.e., in watts [123].

Spectroradiometers are instruments designed to measure the wavelength distribution of radiation in a given wavelength interval. The incoming radiation is usually dispersed by optical elements such as prisms, diffraction gratings, or in a special case, interferometers onto a detection device. Optical radiation is typically measured in the wavelength region between 1 nm and 1 mm. The results in spectroradiometric measurements are usually expressed in spectral radiance or spectral irradiance and are the measurements most commonly taken.

Spectroradiometric measurements are one of the least reliable of all physical measurements. ([50], p. 2)

Sources of errors are widespread and must be taken into account when such measurements are to be used for further analysis. A key source of errors is the instability of measurement or reference instruments; standards to calibrate spectroradiometric devices as well as the measuring instruments themselves. It is often common to spectroradiometric measurements to state a value for an absolute or relative measurement with an estimate of uncertainty and the degree of confidence. It is not unusual that such measurements are uncertain with 10% or more in a confidence interval of 95%.

The amount of this high uncertainty relies not only on the type of instrumentation used, but also on the sources that finally make up the total radiance present at the spectroradiometer. Spectroradiometric measurements are optimized to measure the energy distribution dependent on *one* parameter, where all the other parameters are assumed to be constant or must be integrated for. Another reason for the uncertainty is that radiometric measurement systems together with all of their parts continuously scatter, absorb, and emit.

The contributing sources of radiation onto a spectroradiometric measurement device under solar illumination in the field are visualized in Figure 2.1.

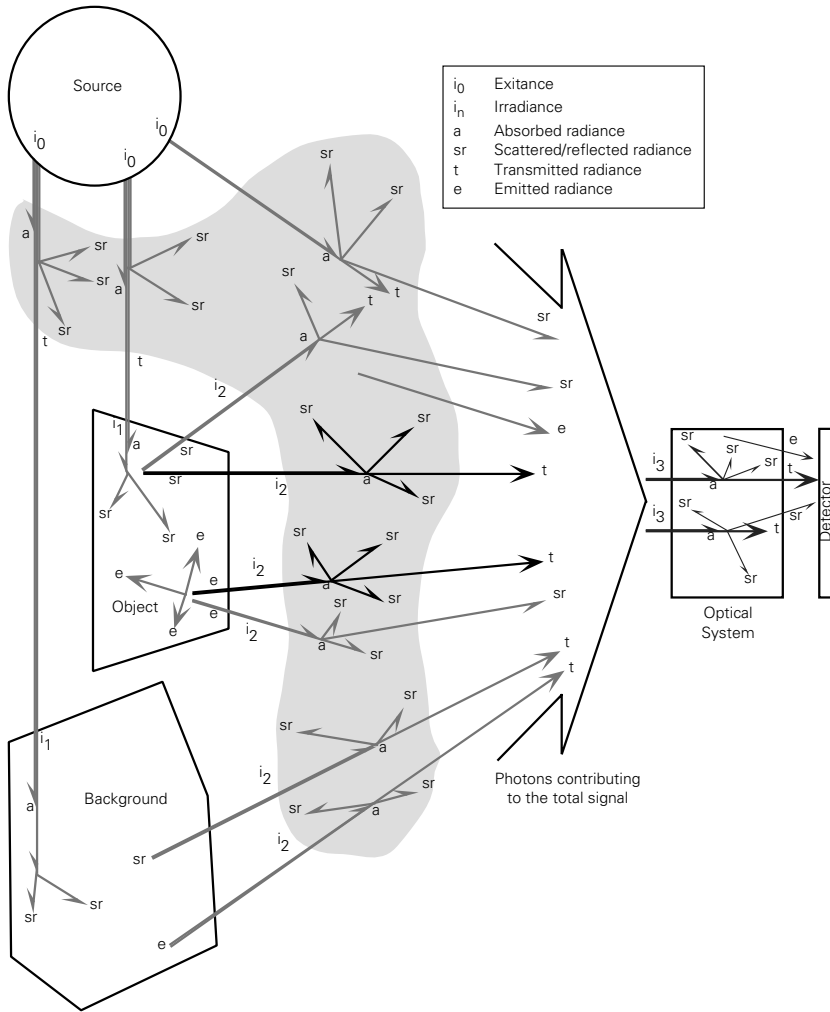


Figure 2.1: Contributing sources to a spectroradiometric measurement.

Progress in the development of detector-technology is strongly related to the success of spectroradiometric measurements [96]. In addition, the total system performance very often depends on the quality of the electronics or the signal processing unit. Many spectroradiometric measuring systems are limited in their performance due to the signal processing chain (i.e. limitation of read-out frequency and traumatization (A/D converter)).

The primary focus of this thesis is on non-imaging spectroradiometers. The primary use of such instruments is the generation of a measurement that is integrated over time, a solid angle and a wavelength. The resulting curve is a spectrum characterizing the electromagnetic energy reflected, emitted, or transmitted from a surface or space.

In general, a non-imaging sensor consists of three major elements:

- an optical system,
built of lenses, mirrors, dispersion elements, and apertures,
- a detector (or more than one)
that converts a signal proportional to the incident radiation on its surface
from photons into electrons, and
- a signal-processor
which converts the electrons into an appropriate output signal.

When performing measurements using a spectroradiometer, three fundamental *measurement methods* may be identified (see Figure 2.2). The major differences between these methods are based on the presence of an object in the transmission medium and the orientation of the optical system with respect to the measurement type (reflectance, transmittance) [97]. In field spectroradiometry the illumination source will always be the sun whereas the transmission medium will be the atmosphere.

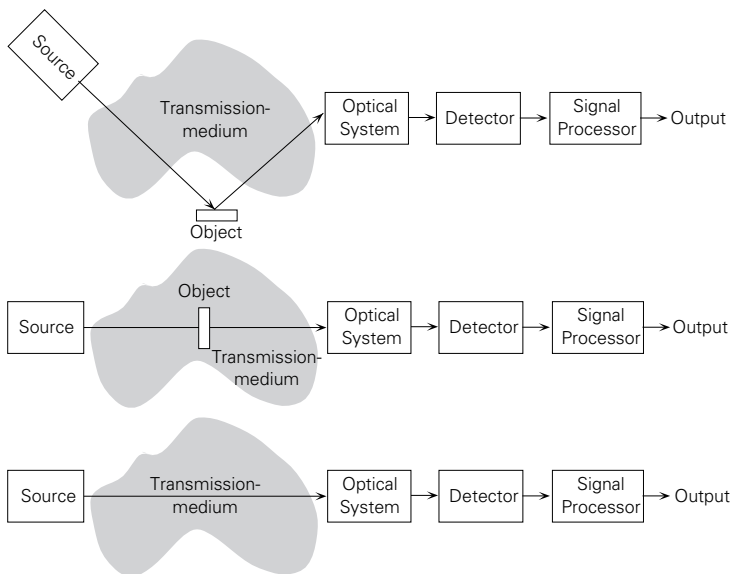


Figure 2.2: Three different measurement modi for spectroradiometers [97].

One of the major characteristics of the atmosphere is its inherent variability. Variations of temperature, pressure, water content and the distribution of molecules generate a highly temporal variability of the atmospheric optical properties. In addition the spatial variability in the vertical structure of the atmosphere introduces another uncertainty when measured over long periods. Field reflectance spectroscopy always focuses on the first type of measurement setup presented in Figure 2.2, and is the one most often performed in remote sensing.

2.2 The Measurement Equation

The measurement equation helps to derive a general description of the performance of a spectroradiometer. R_λ , the *spectral responsivity* of the radiometer is the change in the output signal (ΔS) divided by the change in the radiant power $\Delta\Phi_\lambda$ [80]¹:

$$R_\lambda = \frac{\Delta S}{\Delta\Phi_\lambda} \quad (2.1)$$

Since the major interest here is to measure the average spectral radiance for a given wavelength interval and area, the measurement equation is written as [50]:

$$S = R \cdot L_\lambda \cdot \Delta\lambda \cdot \Delta A \quad (2.2)$$

where S is the output signal of the spectroradiometer. L_λ is the radiant power in the entrance aperture of the area ΔA and $\Delta\lambda$ is the wavelength interval defined by the bandpass filter of the spectroradiometer, and R is the responsivity for this flux. The radiant power reaching the detector is therefore dependent on the field-of-view of the radiometer. The spectral response is determined by the nature of the detector and the dispersion elements used in the optical system of the radiometer. Finally, the signal processing influences the SNR² of the instrument.

2.3 Absolute and Relative Measurements

Absolute measurements are measurements in one of the internationally recognized SI base units. In many cases, absolute accuracy is established by using a transfer standard (such as an integrating sphere) to obtain traceability to SI units. Absolute accuracy is dependent on the measurement quality of the instrument and the transfer standard to be used. In addition, the defined accuracy of the to be traced SI unit is another source of uncertainty. Transfer standards are available from different national standards laboratories. They also define the absolute accuracy of their standards and specify the traceability of the unknown to this standard [116]. One of the best known laboratory for standards is the National Institute of Standards and Technology (NIST) in the USA.

When performing *relative measurements*, the traceability to SI units is not required. In general, relative measurements are obtained by the ratio of two measurements. The accuracy of a relative measurement is assured by the linearity of the measurement instrument (or by the exact knowledge of its nonlinearity function), and by the elimination of differences in the two measurements being divided [104].

¹. A detailed description of all symbols and their associated SI units used throughout this study may be found in the Glossary.

². All acronyms used in this study are available in the Appendix.

2.4 Sources of Uncertainty

A spectroradiometric measurement is a multidimensional problem because the measured value is not only influenced by the variables defined in eq. (2.2), but also by other factors such as the polarization of the incoming light, the position of it in the entrance aperture, its direction and the wavelength distribution.

The proper identification of uncertainties within a measurement process allows not only the release of a quantitative indication of the quality of the result but also allows a better comparison. Uncertainties associated with error sources are part of the error analysis. Yet even if all sources of errors are identified and an uncertainty (or accuracy) associated with each, it is still doubtful how well the absolute measurement represents the value of the quantity being measured.

In section 6.1 a detailed discussion of uncertainties associated with spectroradiometric measurements can be found. Two major categories of uncertainties can be discriminated:

- **Type A**

Method of evaluation of uncertainty based upon statistical analysis of a series of observations

- **Type B**

Method of evaluation of uncertainty by means other than a statistical analysis of a series of observations.

All possible sources of uncertainty in spectroradiometric measurements are identified during the characterization and calibration processes throughout this work.

Chapter 3:

Spectroradiometric Measurement Equipment

3.1 Introduction

In this chapter, the measurement equipment used in this investigation is described and pointers to relevant sources indicated. Special emphasis is placed on the evaluation for the field spectroradiometer characterized and calibrated in the following chapters.

3.2 Evaluation Criteria for a Field Spectroradiometer

Evaluation and procurement of a field portable spectroradiometer operating in the solar reflected wavelength range between 400–2500 nm is a difficult endeavor. Only a few companies worldwide offer such instruments and the international demand for portable spectroradiometer covering the requested wavelength range does not exceed more than hundred instruments a year. In addition to space constraints, power consumption limitations and the complexity of an optical path designed for such small devices make these instruments technically complex and therefore affordable only for a limited number of users.

During the evaluation process, a list of criteria based on the specific needs of RSL has been compiled which contains mostly functional specifications (see Table 3.1). An important issue by defining these specifications is the cost envelope. Overspecification can significantly contribute to the total cost of the system. Since RSL is an applied user of the instrumentation being evaluated, no component or assembly specifications are required. The level of detail of any specifications depends strongly on the planned use of the instrument. In most applications it is satisfactory to use a well characterized instrument for reflectance measurements. The core equipment for this application is the spectroradiometer and a diffuse reflectance standard. Using the spectroradiometer for relative or absolute radiometric applications, such as the vicarious calibration, a traceability to a standard must be established. This requires additional calibration equipment and a characterization, calibration and validation procedure.

Functional Group	Specification	Requirement
Environmental Specifications	Operating temperature Humidity	-10 to 40° C 15 to 80%, non condensing
Special Operating Conditions	Shock Vibration Storage environment Radiation environment	n.s. n.s. n.s. n.s.
Functional Specifications	Ease of use Remote operation (up to 6 m) Compatibility with FIGOS Rapid data takes No moving or moveable parts Adjustable FOV Cost target Finish quality of the optical system Size Weight	important strict strict ≤ 5 s / scan strict fixed at 2 focal lengths ≤ 70'000 US\$ n.s. ≤ 30 x 30 x 30 cm ≤ 12 kg
Optical Specifications	Focal length <i>f</i> -number FOV MTF Magnification Wavelength range Diffraction elements	n.s. n.s. n.s. n.s. n.s. 400 to 2500 nm gratings
Coating Specifications	Lenses Beam splitter	transmittant over wavelength range n.s.
Material Specifications	Lenses Optical manufacture Housing	n.s. optimized for athermalization optimized for athermalization
Detector Specifications	Detector types D*	Si / PbS line arrays n.s.
Performance Specifications	Spectral sampling interval Spectral resolution / FWHM NER	≤ 12 nm ≤ 10 nm n.s.
Accuracy Specifications	Wavelength accuracy Wavelength repeatability Radiometric accuracy	±0.2 nm ±0.1 nm < 10% uncertainty

Table 3.1: RSL specifications for the spectroradiometer evaluation (n.s. = not specified by RSL for evaluation).

Functional Group	Specification	Requirement
Additional Specifications	Options	Fore-optics (cosine receptor, larger FOV)
	Expansibility	n.s.
	Upgrade/sidegrade possibilities	n.s.
	Services Support	Recalibration Hotline
Contractual Specifications	Terms of reference	FOB factory
	Warranty	1 year full
	Payment procedure	check, after acceptance tests

Table 3.1: RSL specifications for the spectroradiometer evaluation (n.s. = not specified by RSL for evaluation).

Special emphasis is put on evaluation criteria such as the transportation concept for the spectroradiometer. If the instrument is operated by many different users, the ease-of-use must be granted. A special measurement protocol is set up to record attribute data for every measurement taken in the field. In many cases it is necessary to discriminate and label spatial entities before the actual measurement campaign. The total number of measurements to be taken in one period can be increased substantially using this approach.

If the spectroradiometer is not mounted on a tripod during field measurements, or used in the laboratory calibration on an optical bench, it may also be mounted on a goniometer (FIGOS). This system requires remote operation from approximately 6 m, and thus a separation of the optical head from the computer controlling the instrument. Using an alternative method with fibre optics at 6 m is dropped from the evaluation, because of the low transmission of fibres in wavelengths higher than 2000 nm.

The spectroradiometer must have sufficient short integration times in order to minimize the total duration of an hemispherical scan on the goniometer and to prevent measuring positional drifts of the sun. Single detector instruments using a scanning mechanism exceeding a measurement time of 30 s are therefore not evaluated.

Variable or adjustable FOV is another important criterion. Measuring isolated minerals for spectral libraries in a laboratory environment requires a smaller FOV than assessing the homogeneity of a meadow for vegetation analysis. Certainly the sampling strategy for both applications is also different.

The final evaluation led to the decision to buy a GER3700 spectroradiometer manufactured by GER Corp. in Millbrook, NY.

3.3 The GER3700 Instrument

The GER3700 spectroradiometer used in this study was operational in Switzerland starting in spring, 1995. It is the second instrument ever produced in this series (SN# 3700–1002) and has undergone substantial enhancements over the past few years. The enhancements not only affected this specific instrument, but subsequently were incorporated into its successors. The present design and the features of these instruments were significantly influenced by the CCRS and RSL [110]. The initial GER3700 factory specifications are listed in Table 3.2.

Parameter	Description
Spectral Range	300–2500 nm
Channels	704
Linear Arrays	1 Si & 2 PbS
Bandwidth	1.5 nm (300–1050 nm) 6.2 nm (1050–1840 nm) 8.6 nm (1950–2500 nm)
Scan Time	≥ 50 ms
FOV	Dependent on fore-optic
Head Size	286 x 305 x 114 mm
Weight	6.4 kg
Battery Life / Voltage	4 h / 12 V (6.8 Ah)
Digitization	16 Bit
Wavelength Accuracy/Repeatability	± 1 nm / ± 0.1 nm
Spectrum Averaging	Yes
Dark Current Correction	Automatic
Operating Environment	10–90% Humidity / -10° to 50° C

Table 3.2: GER3700 factory specifications [35].

3.3.1 Technical Description

The GER3700 is a single FOV spectroradiometer operating in the visible, near- and short-wavelength-infrared (VIS, NIR, SWIR). The wavelength range covered is 400–2500 (or 280–2490) nm, depending on the positioning of the diffraction gratings. The reflected radiance is measured using three detectors. The first detector is a silicon (Si) line array with 512 elements. The two remaining detectors are lead sulfide (PbS) line arrays with 128 and 64 elements respectively. Because the PbS detectors are operated in an uncooled environment, ambient (or room) temperature operation (ATO) types have been chosen. The cutoff wavelength for the Si detector can be adjusted by software between 980 and 1030 nm,

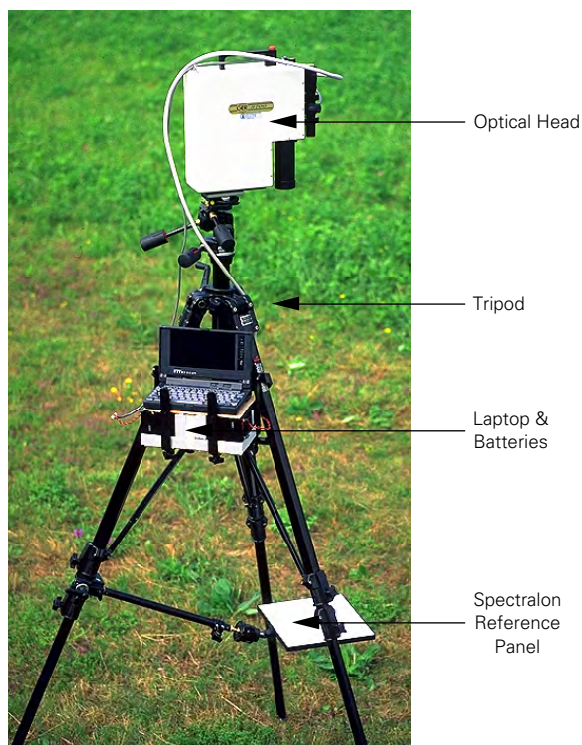


Figure 3.1: GER3700 spectroradiometer mounted on a tripod with laptop computer, batteries and Spectralon reflectance standard.

the transition between the PbS1 and PbS2 detector is fixed near 1900 nm. This results in a setup with 512 channels covering the 400–1000 nm range, 128 channels covering the 1000–1900 nm range, and 64 channels covering the 1900–2500 nm range. In total, 704 spectral channels are recorded simultaneously [19][121] (see Figure 3.2).

The GER3700 optical head weighs about 10 kg and can be mounted on a variety of platforms. The major use is a tripod for field reflectance measurements. The measurement altitude of the tripod may be adjusted to heights of 70 to 270 cm above ground. On the tripod the laptop computer controlling the instrument and the batteries are kept in a specially designed holder. The optical head can easily be removed from the tripod and put in a carrying case for transportation (see Figure 3.1).

The field use of the GER3700 instrument requires at least 2 persons to carry the tripod, the spectroradiometer, the reflectance standard and the computer. During data acquisition, one person operates the laptop computer and controls the instrument's behavior, while the other person records the measurements and handles the Spectralon reference panel.

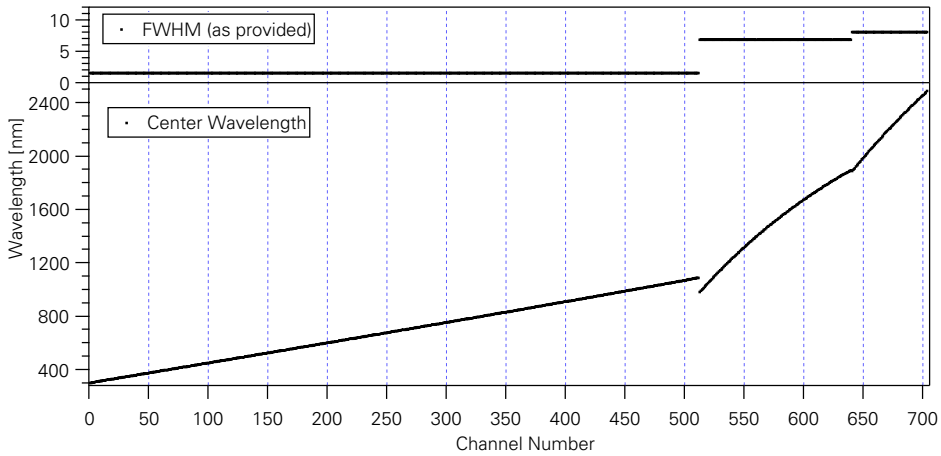


Figure 3.2: Center wavelength and FWHM of the GER3700 as provided by the manufacturer [35].

There are a number of fore-optics available for the GER3700. In the RSL configuration the standard optic has a FOV of 2°. The standard fore-optic can be exchanged with either a 50 cm fibre-optic cable or a 10° FOV lens.

The integration time and the averaging of the measurements is controlled by software. The integration time can be set individually for the Si and the PbS detectors. There are no moving parts in the instrument except for a chopper for the SWIR channels. The advantage of having no moving parts is a substantial reduction of acquisition time for one spectrum and greater insensitivity of the instrument against low-frequency vibrations.

3.3.2 Major Measurement Campaigns and Use

Many different measurement campaigns have been carried out in a variety of applications in the past few years using the GER3700. The following table (Table 3.3) presents an overview of all measurements.

Type	Description	Measurements	Period	Ref.
FIGOS	Grass meadow	432	5/1995	[83]
Calibration	Acceptance tests	539	7/1995	n.a.
FIGOS	Grass meadow	288	7/1995	[85]
Reflectance	Land use	243	8/1995	n.a.
Calibration	Radiance calibration	396	9/1995	n.a.

Table 3.3: Major measurement campaigns using the GER3700 spectroradiometer (1995–1998) (n.a. = no literature available).

Type	Description	Measurements	Period	Ref.
Calibration	Reflectance calibration	180	3/1996	n.a.
Calibration	SNR / Linearity	141	4/1996	n.a.
EGO	Rye-grass, watercress, Spectralon, concrete slab	1761	4/1996	[86]
FIGOS	Concrete slab, rye-grass	360	5/1996	n.a.
FIGOS	Rye-grass	144	6/1996	n.a.
Calibration	SNR	46	7/1996	n.a.
FIGOS	Tartan	288	7/1996	n.a.
Vicarious calibration	DAIS 7915 vicarious calibration	59	7/1996	[91] [111]
FIGOS	Concrete	156	8/1996	n.a.
Radiance	Adjacency effects measurement	232	9/1996	[90]
Calibration	Dye laser	320	9/1996	this study
Calibration	Langley plot method	900	1/1997	n.a.
Spectral Library	Minerals	112	2/1997	[27]
Calibration	Full characterization	13320	9/96–3/97	this study
FIGOS	Rye-grass	76	4/1997	n.a.
Reflectance	Biodiversity assessment	87	6/1997	[112]
Reflectance	Geology	24	7/1997	[27]
FIGOS	Rye-grass	639	7/1997	n.a.
Reflectance	Biodiversity assessment	71	7/1997	[112]
Reflectance	Alpine meadow	124	8/1997	[60]
Vicarious calibration	DAIS 7915 vicarious calibration	66	8/1997	[93]
Reflectance	Land use	166	8/1998	[47]
Reflectance	Biodiversity assessment	321	8/1997	[112]
Reflectance	Biodiversity assessment	106	9/1997	[112]
Spectral Library	Geology	189	9/1997	[27]
Reflectance	DAIS 7915 vicarious calibration	110	6/1998	n.a.
Reflectance	Artificial objects	160	6/1998	n.a.

Table 3.3: Major measurement campaigns using the GER3700 spectroradiometer (1995–1998) (n.a. = no literature available).

The major types discriminated are the collection of reflectance data in the field, data collection for spectral libraries in the laboratory, vicarious calibration in support of the validation of hyperspectral sensors, goniometer measurements, and measurements for the characterization, calibration and validation of the performance of the spectroradiometer itself. Roughly over 20'000 measurements have been collected in the three year operating period.

3.4 Other Supporting Equipment

a) University of Arizona Auto Sun-Tracking 10 Channel Solar Radiometer Instrument

The Reagan sun-photometer is a sun-looking ground based instrument for atmospheric measurements. It is used as an atmospheric ground truthing instrument in field campaigns (see Figure 3.3). Its continuous monitoring of the state of the atmosphere allows further conclusions on atmospheric stability and daily developments of aerosol contents and water vapor to be made [95].

The sun-photometer was manufactured by the Department of Electrical Engineering, University of Tucson, Arizona, in 1995 (Serial Number 14). The technical specifications are given as follows:

- 10 channel parallel colligned FOV tube with FOV $\approx 3.2^\circ$
- Channels at 382, 410, 501, 611, 669, 721, 780, 872, 940, and 1033 nm.
- Narrow band three-cavity interference filters with FWHM of ≈ 8 to 12 nm
- Digitization 16 bits
- Temperature stability at $\approx 43 \pm 0.5^\circ\text{C}$ by heater control
- Data logger for 2-3 days of data acquisition (32 K byte non volatile RAM)
- Automatic sun tracking, $\pm 17^\circ$ tracking capability
- 12 V Power supply or battery for one day of independent usage
- Average power consumption 15 W
- Fully transportable (total weight: ca. 13.5 kg plus boxes).

b) Field Goniometer System (FIGOS)

In order to obtain bidirectional reflectance factor (BRF) data under natural atmospheric and illumination conditions, a transportable field-goniometer has been constructed. FIGOS (field-goniometer system) allows for measuring the target reflectance over the hemisphere by user-defined viewing angles. It is operated together with the GER3700 spectroradiometer.

The field-goniometer was built by Willy Sandmeier under the support of Lehner + Co AG, and in cooperation with the RSL. It consists of three major parts: a zenith arc, an azimuth arc, and a motor driven sled on which the spectroradiometer is mounted. The azimuth arc consists of twelve sockets on which a rail of 2 m radius onto which the zenith arc is mounted. The zenith arc is mounted eccentrically on the azimuth rail in order to prevent shadowing of the target when measuring in the solar principal plane. The minimum distance between the cen-



Figure 3.3: Sun-photometer during Langley-calibration.

ter of the target and the shadow of the zenith arc aligned in the solar principal plane is 14 cm. As the field of view of the GER3700 is approx. 2° , measurements within the solar principal plane are free from shadow of the zenith arc. FIGOS always points to the same spot in the center of the hemisphere, i.e. all hemispherical data correspond to the same target in the center of the azimuth arc.

Freely applicable labels on the zenith arc allow for an automated positioning of the spectroradiometer. It is also possible to drive the sled-motor manually from a remote control unit to any desired position on the zenith arc. The positioning precision on the zenith arc is within $\pm 0.2^\circ$. The azimuth view angle is given by a scale engraved in the azimuth basement. At the current status the zenith arc is positioned manually with the help of a pointer. By default an increment of 30° is set on the azimuth arc resulting in 6 measurement profiles, each containing 11 measurements on the zenith arc. Thus, to cover the full hemisphere 66 measurements are needed. A full hemisphere is covered in approx. 15 minutes, including



Figure 3.4: The FIGOS (Field Goniometer System) in operation on a soccer field.

time for repositioning of the zenith arc, and for actually taking the measurements (see Figure 3.4).

The total weight of the field-goniometer amounts to about 230 kg. The maximum weight of a single part is 61 kg which is the zenith arc itself with the sled to be mounted on the azimuth rail. It is therefore possible for two people to transport and assemble the goniometer. Less than 2 hours are needed for setting it up [83][84][89].

c) Labsphere Spectralon Diffuse Reflectance Standard

Labsphere Inc. is a supplier of diffuse reflectance standards, which are calibrated and traceable to NIST. Diffuse reflectance coatings for any reflectance application are manufactured upon customer request. The Spectralon diffuse reflectance standard is discussed in detail in section 5.3.1 [53][54].

d) Optronic Laboratories Integrating Sphere Calibration Standard

Optronic Laboratories, Inc. is a company specializing in the measurement of optical radiation. Radiometric standards, calibration services and spectroradiometers are their products. The integrating sphere calibration standard used for the absolute radiometric calibration of the GER3700 is discussed in detail in section 4.3.2 [63][64].

e) Coherent Ring Dye Laser

The laser manufactured by Coherent is provided by the Department of Physics of the University of Zürich. It is installed in their facilities and is normally used in quantum optics for spatiotemporal nonlinear interactions between light and matter [16][23][67].

Chapter 4:

Laboratory Calibration

4.1 Introduction

A full calibration of a remote sensing system includes the characterization, calibration, and validation process. This chapter presents the characterization and calibration process for a ground based spectroradiometer. All these processes are very costly in terms of time consumption, repeatability, degrading of calibration equipment, automatization and human resources. Since the usability and the reliability of spectroradiometric instrumentation is directly proportional to the calibration effort, however, it is worthwhile to unlock these details.

Every calibration is sensor dependent. A general calibration methodology cannot be given easily since every single calibration step relies on the hardware and resources available and the accuracy needed.

It has been proven in the special case of imaging spectroscopy, however, that an extensive calibration effort enhances the user community's trust in the instrument, increase its reliability and generate more scientific feedback to the operators of these instruments [12][61][111]. Extensive use of calibrated spectrometer data relies on the trustworthiness of the instrument and its calibration.

An absolute radiometric measurement is a measurement that is based upon (or derived from) one of the internationally recognized units of physical measurements. These units are known as the SI units. A convenient method for achieving these is to obtain traceability to one of the SI units via a calibration standard issued by one of the national standard laboratories (e.g. NIST, National Institute of Standards and Technology).

A relative measurement is one that does not need be traceable to one of the SI units. Relative measurements are usually obtained from the ratio of two measurements. They are independent of SI units.

4.2 Selection of a Calibration Strategy

4.2.1 Introduction

The successful selection of an appropriate calibration strategy relies on many fac-

tors which need to be determined before the actual calibration begins. Different users have different ideas about the calibration effort. For more technically oriented scientists, the full characterization of the instrument is the primary interest, whereas an applied user typically has concerns about algorithm robustness for the calibration uncertainty. These days there are remote sensing instruments where there is neither a published calibration sheet nor user access to this data. Using uncalibrated data, the user has to choose from some image based calibration processes to convert the sensor values into apparent reflectances [34][52][78][79].

The laboratory calibration is the most cost and time effective calibration. The accuracy desired from this type of calibration must be carefully determined in advance in order to assure user satisfaction. There is a fundamental difference in selecting a calibration strategy for uncertainties of 1% or 10%. Many calibration standards do not supply an uncertainty of 1% or less simply because their traceability to a primary standard degrades over time because of ageing of the lamp standard. In addition, it might be important to measure many quantities in a very short period for a 1% calibration to avoid drifts associated with the measurement process. Both are very cost efficient processes in terms of resources and money.

It is therefore important to set up a measurement plan that provides a high level of detail for which quantity is to be measured and how the measurement is performed. The final outcome of this plan is the characterization and calibration of the spectroradiometer including a detailed error analysis and an uncertainty report.

Field reflectance measurements using a well characterized instrument use the same detailed measurement plan. The plan is established for the laboratory calibration but strongly depends on the sampling strategy used in the field and the sun as illumination source. The measurement plan for field reflectance measurements is discussed in Chapter 5.

4.2.2 The Measurement Plan

A generalized measurement plan has been developed by Kostkowski (p. 417, [50]) for an irradiance calibration, and is adapted here for the special case of the calibration of a spectroradiometer for radiance measurements in the 400–2500 nm region of the electromagnetic spectrum (see Table 4.1). The calibration action undertaken is discussed in the respective section in the ‘Discussion / Error’ column in Table 4.1, if not otherwise stated in the text.

Major Plan	Detailed Plan	Discussion / Error
Detailed description of the quantity to be measured including the accuracy desired	Quantity to be measured Wavelengths to be measured Measurement accuracy desired Geometry of quantity Relative spectral distribution Approximate magnitude Stability Polarization	Spectral radiance 400–2500 nm ≤ 10% Nadir looking measurement of radiances 400–2500 nm <700 W/(m ² sr μm) ≤ 5% ≤ 2%
Identification of potential error sources and their estimation of their magnitude (can also be according to specifications or literature search)	Noise to signal Nonlinearity Directional effects Spectral scattering Spectral distortion Polarization effects Size-of-source effect Wavelength instability Detector instability Uncertainty of the standard Instability of the standard Instability of the quantity being measured Noise in the measurement data	< 1% ≤ 0.5% < 1% < 0.75% < 0.8% ≤ 2% << 0.5% < 0.6% 0.7% ± 3 to ± 6% ± 2% ± 1% < 1%
Selection of the radiance standard	Source standard	chapt. 4.3.2
Selection of the spectroradiometer	Selecting the fore-optics Selecting the system setup	2° FOV chapt. 3.3
Select the wavelength standard	Line irradiance or radiance Separation from neighbouring lines Number and distribution of lines	chapt. 4.6.4 0.1 nm / 1 MHz 300, evenly spaced 450–750 nm
Instrument assembly and preliminary checks	Establishing the optical axis Setting up the fore-optics Checking the output signal Checking the wavelength readout	chapt. 4.5.2 chapt. 4.5.2 chapt. 4.6.1 chapt. 4.6.1

Table 4.1: Measurement plan for the GER3700 spectroradiometer (Adapted following [50]).

Major Plan	Detailed Plan	Discussion / Error
Characterize the spectroradiometer for all potential errors	SNR, NER, and dark current Wavelength characterization Nonlinearity characterization Directional and positional characterization Spectral scattering characterization FOV Polarization characterization Size of source characterization Temperature characterization	chapt. 4.6.1 chapt. 4.6.4 chapt. 4.6.5 chapt. 4.6.6 chapt. 4.6.7 chapt. 4.6.8 chapt. 4.6.9 chapt. 4.6.10 chapt. 4.6.11
Select and characterize the measurement setup	Selection Characterization	selected according to characterization process, details in respective chapters
Select the measurement design	Design	depending on requirement (between 10–500 measurements)
Acquire the data and calculate the quantity desired	Carrying out the measurements	individual subchapters in chapt. 4.6.n
Prepare the uncertainty report	All sources of uncertainty Error 'Type A' or 'Type B' Degrees of freedom Combined uncertainty Expanded uncertainty Unidentified sources of uncertainty	chapt. 6.2.1.a chapt. 6.2.1.b chapt. 6.2.1.c chapt. 6.2.1.d chapt. 6.2.1.e chapt. 6.2.1.a

Table 4.1: Measurement plan for the GER3700 spectroradiometer (Adapted following [50]).

4.3 Calibration Standards

Accurate measurement of optical radiation involves not only the use of a stable, well-characterized spectroradiometer or imaging spectrometer, but also the use of standard(s). In general, three types of standards may be identified:

- Primary standards
are calibrated by national laboratories,
- Secondary standards
are calibrated by secondary laboratories using national laboratories' primary

standards to establish traceability, and

- Working standards

are generally calibrated inhouse as compared to primary or secondary standards.

In most cases, the access to primary standards is difficult because they are located at the standardization authorities only. Most laboratories therefore use secondary standards to establish a traceability of their instruments to a primary standard. The secondary standard is then used as a calibration transfer device. The traceability established in this work relies on secondary standards such as the integrating sphere calibration standard and the Spectralon reflectance standard except the dye laser used (working standard).

The major uncertainty with secondary standards is instability over time. A life cycle determination or an uncertainty change over time is always included with these standards.

4.3.1 Spectral Irradiance and Radiance Standards

The use of irradiance standards for absolute calibration is dominated by the FEL 1000-watt tungsten halogen lamp [10]. Other standards such as deuterium lamps, argon arcs do exist. The uncertainty of the associated NIST calibration of these lamps is generally better than 1%. They are operated on direct current (DC) and use current stabilized power supplies.

In the wavelength range between 300–2500 nm, tungsten strip lamps (tungsten ribbon filament lamp) are used as spectral radiance standards. The lamps must be handled very carefully and usually the current is slowly ramped up to assure the full functionality of the tungsten cycle (evaporated and redeposited tungsten on the lamp filament) during the operation.

4.3.2 Integrating Sphere Calibration Standard

Integrating spheres are widely used to calibrate spectroradiometric measurement devices. Several types of measurements such as diffuse reflectance, specular reflectance and diffuse transmittance can be performed using an integrating sphere. In general an integrating sphere is a hollow sphere which has its interior coated with a substance that is nearly perfectly diffuse or lambertian. For the accurate radiance calibration of a spectroradiometer, the sphere as a source of uniform radiation as a secondary standard is discussed.

The exit port of the integrating sphere is a circular lambertian source. It has only an apparent radiance because it is actually the sphere wall which is radiant. The luminance across the plane of the exit port is also extremely uniform and therefore independent of the viewing angle.

The integrating sphere calibration standard consists of two parts. One part is the optics head that is calibrated for luminance, color temperature and spectral radiance. The light source is a 150 W tungsten quartz–halogen lamp. A shutter mechanically separates the irradiance exiting the lamp and the integrating sphere.



Figure 4.1: Integrating sphere calibration setup with spectroradiometer attached.

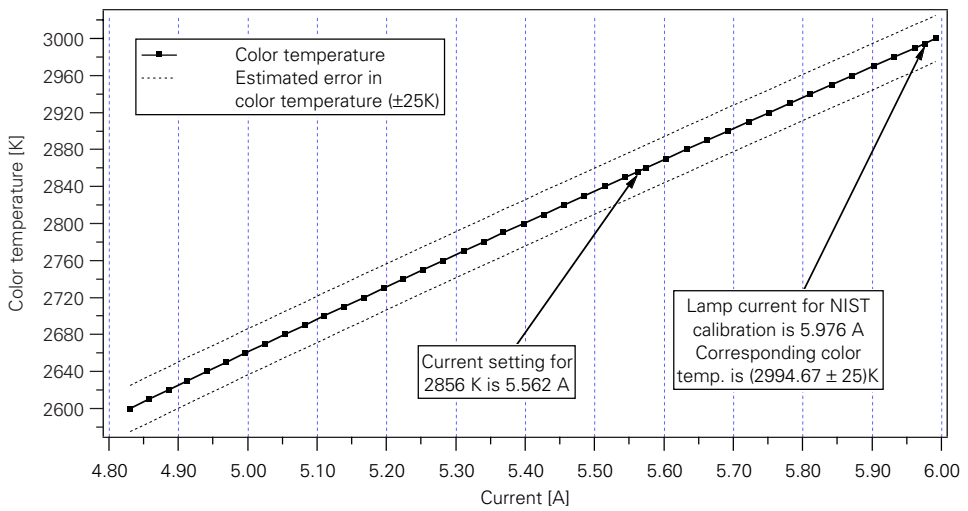


Figure 4.2: Color temperature calibration values for the integrating sphere [64].

A variable aperture controls the luminance level without changing the color temperature. Inside the sphere, a precision silicon detector with a filtered CIE photopic response is mounted and monitors the sphere luminance (see Figure 4.1). The color temperature of the source is a function of the lamp current. The variation of the color temperature is calibrated up to 3000 K at 10 K intervals. The luminance and color temperature calibration relative to standards supplied by NIST are given in Figure 4.2. The NIST traceable luminance accuracy is less than $\pm 2\%$ (± 0.005 fL) and the estimated uncertainty in color temperature is ± 25 K. The calibrated current setting for 2856 K is 5.562 A [64].

The spectral radiance calibration is obtained for a specific lamp current and luminance setting. In order to achieve a relatively high level of spectral radiance, the nominal color temperature for the spectral radiance calibration corresponds to (2994.67 ± 25) K (whereas the sun has a color temperature of 5770 K). The listed spectral radiance values are calibrated for the given lamp current of 5.976 A, and the luminance is set to 12284 Footlambert (fL) (see Table 4.2).

Name	Data
Sphere Diameter	8 inch
Exit Port Diameter	2 inch
Luminance Uncertainty (relative to NIST)	$\pm 2\%$
Spectral Radiance Calibration (relative to NIST)	± 3 to $\pm 6\%$
Colour Temperature Range	2000–3000 K
Colour Temperature Uncertainty	± 25 K
Luminance Stability	$\pm 0.5\%$
Maximum Luminance at 2856 K	3000 fL
Maximum Luminance at 3000 K	5000 fL
Minimum Luminance	0.001 fL

Table 4.2: Properties of integrating sphere calibration standard [63].

The second part of the calibration standard is a precision constant current regulator to operate the 150 W tungsten lamp. A current ramp up/ramp down circuit is employed to prevent shocking the lamp and to enhance calibration source life. Despite these electronic supporting means, the luminance stability of the lamp is $\pm 0.5\%$ after 15 minutes warm-up and $\pm 2\%$ for 100 hours of use, or 1 year.

The uncertainty of the calibration standard is relatively high compared to the total uncertainty expected from this kind of measurement. In addition a comparison by Walker et. al. [117] demonstrates that a calibration traceable to NIST varies between the 11 National Laboratories tested with an uncertainty of up to $\pm 8\%$. The NIST calibrated spectral radiance for this sphere is given in Figure 4.3.

The current produced by the photometric detector is converted to luminance values (fL) and can be calibrated to zero out any photometer offset current, or any signal due to stray light (dark current calibration). The same null level calibration is also available for the lamp current setting .

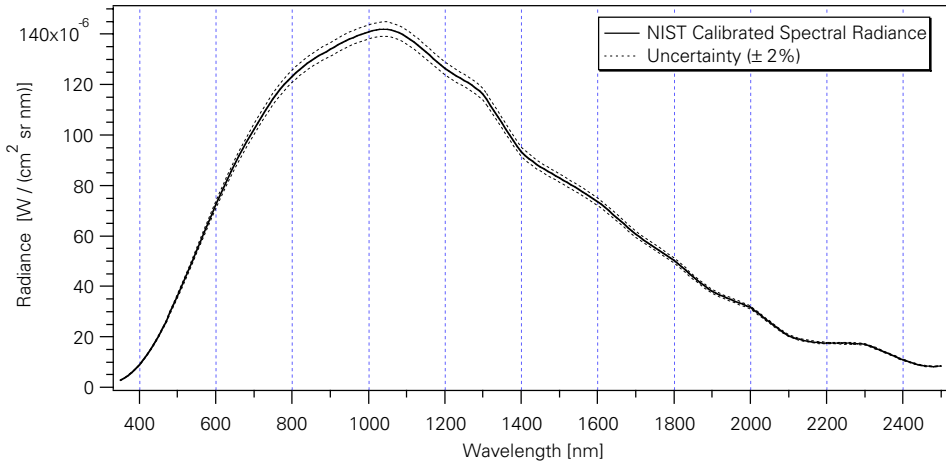


Figure 4.3: Integrating sphere NIST calibrated spectral radiance [64].

4.4 Wavelength Standards

Wavelength standards are needed to calibrate spectroradiometers for wavelength position and accuracy. Atomic emission lines are normally used for wavelength calibration and they are obtained from sources such as discharge lamps, gas cell absorption lines, laser lines, and interferometric spectrometers.

Since the calibration performed throughout this work focuses only on the solar reflected portion of the electromagnetic spectrum, wavelength standards are limited to the operation in the 400–2500 nm range. In this range most atomic emission lines from discharge lamps such as mercury or helium or lasers (i.e He–Ne, Ar, Kr, etc.) are best suited [10].

Selecting the right wavelength standard depends on five principal selection criteria. The wavelength uncertainty of the standard must be < 0.1 nm. In spectroradiometry it is usual to deal with spectral bandpasses of 0.1 to 10 nm. The second selection criterion is that the spectral wavelength standard must have a much narrower line width than the spectral bandpass of the spectroradiometer. The irradiance of the standard must be sufficiently high to produce an acceptable SNR at the spectroradiometer. Using a monochromator as wavelength standard illuminated by a tungsten lamp, the resulting flux might not generate enough signal to obtain a good result. Another point is the separation of spectral lines. If the

discharge lamp has more than one line in the bandpass of the spectroradiometer, the result is a combined signal of both lines. Assuming a very high resolution of your wavelength standard (i.e. 0.1 nm) it would require 21'000 lines to fully describe the above-mentioned wavelength range in detail. Interference problems are serious if the spectroradiometer to be calibrated has an excellent spectral resolution (< 1 nm). The last factor to be considered is the distribution of calibration lines over the observed wavelength range. The goal is to avoid any significant gap over the full range. Also, with a reduced number of emission lines it is possible to calibrate for wavelength centers. The most accurate calibration uses as much as possible emission lines, such as lines from tunable dye lasers or reference monochromators.

4.5 Selection and Characterization of the Measurement Setup

4.5.1 Selection of Instrument Parameters

All calibrations—if not otherwise stated—are performed using the GER3700 (SN# 3700–1002) spectroradiometer with special operating software supplied with the instrument (Rev. 3). All calibrations are performed using the 2° FOV.

The integration times for the detectors are set to one for the Si detector and 8 for the PbS detector. The number of measurements averaged is always set to 9, which is a compromise between good SNR and measurement speed. Since over 13'000 measurements have been performed throughout the laboratory measurement period, the averaging time is a substantial contributor to the overall measurement duration.

4.5.2 Measurement Setup

In general, three different measurement setups are used throughout the characterization process (see Figure 4.4). The first one is the spectroradiometer coupled to the integrating sphere, the second is the spectroradiometer on the optical bench of the tunable dye laser and the third one uses the spectroradiometer on a tripod for reflectance measurements.

Type 1 is the one most often used. The placeholder is specifically manufactured to couple the fore-optic of the spectroradiometer to the integrating sphere. The homogeneity of the sphere output is considered as a function of distance of the exit port [1]. Therefore a special black anodized aluminum holder mechanically and optically fits the spectroradiometer tightly to the sphere's exit port.

Type 2 measurements have been performed on the optical bench of the tunable dye laser. The term 'optical elements' is discussed in detail in section 4.6.4.

Type 3 measurements are performed to measure the FOV and is also the normal setup used in the field. There the illuminating source is the sun (Type 3b) instead of tungsten halogen lamps (Type 3a).

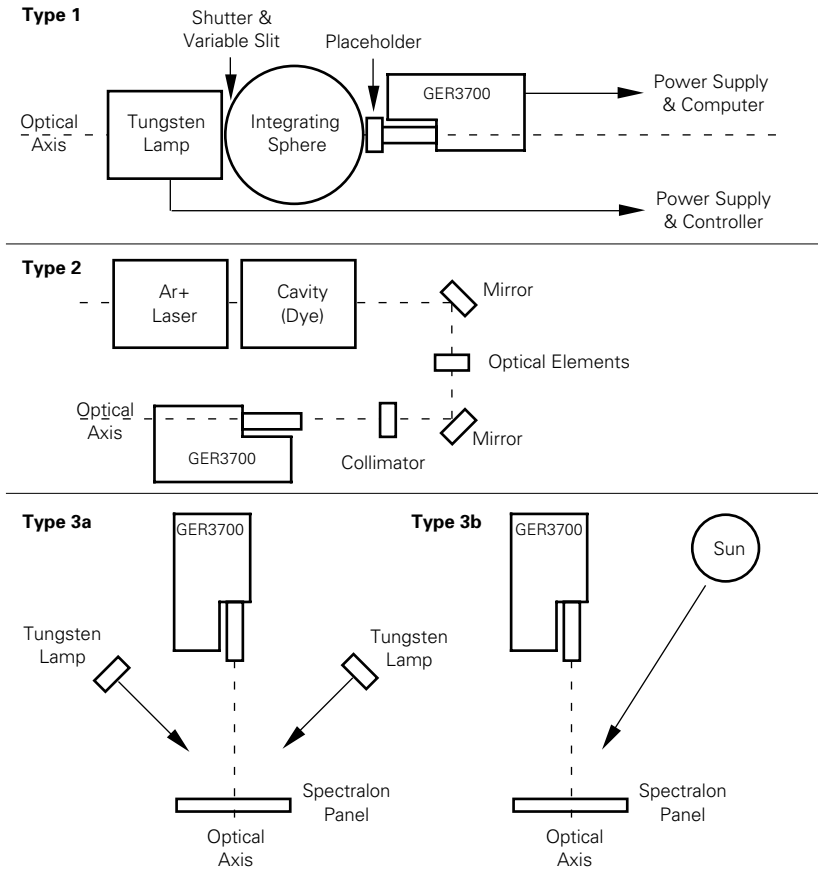


Figure 4.4: Three types of measurement setups for the characterization process.

4.6 Characterization Process

4.6.1 Signal to Noise Ratio

a) Introduction

Noise may be present in the radiant flux arriving at the detector. This external noise may be generated in the processing of the optical signal by mechanical vibrations of the optical components, inadequate spectral filtering, inadequate definition of the required field of view, random scattering of stray light (dependent on the radiance distribution of the target) and other random systematic sources of unwanted variation of the flux incident on the detector. In addition, electrical noise may be generated in the system (including the detectors) by electromagnetic fields originating from chopper motors and other sources. Most of

the unwanted flux variations can be minimized through proper design and construction. However, quantum noise generated by the random arrival of photons from a constant source cannot be eliminated. Internal noise is produced due to the detectors and the signal processing. The major sources are the detector, the detector-bias circuit, the preamplifier, and in chopped systems the nonrandom demodulation residuals.

The other components of the measured quantity is defined as the signal. This noiseless part of a measurement carries the information of interest [98]. Most instruments aim to achieve the highest number of signal to noise, simply to maximize the quantifiable amount of usable information.

b) Theory

There are many definitions of SNR available in remote sensing. The complexity of a reliable and reproducible SNR definition relies on the meaningfulness of the terms noise and signal. Since this calibration focuses primarily on laboratory calibration of non-imaging sensors, a detailed discussion of the definition of SNR for other than this application is omitted. The SNR definition used here relies on noise in a signal that is defined as the standard deviation of that signal [50]:

$$SNR = \frac{S}{N} = \frac{R_{DN, total} - R_{DN, dark}}{\sqrt{\sigma^2(R_{DN, total}) + \sigma^2(R_{DN, dark})}} \quad (4.1)$$

where

R_{DN}	Measured signal (either the dark current or the total signal)
σ	Standard deviation.

c) Measuring the SNR

The SNR in the laboratory is measured using the integrating sphere calibration standard serving as a constant radiation source. At least 30 measurements for each radiation level are taken. The first measurement records the radiant flux from the integrating sphere. Then, after inserting the shutter, the dark current is determined without any signal incident on the spectroradiometer. Following eq. (4.1) the measurements are repeated for both radiance levels, the minimum and maximum respectively.

d) Results

The advantage of laboratory determined SNR is the absence of significant changes in the optical path. The integrating sphere as an inherently stable radiance source exhibits only a very small standard deviation in luminance over time. The expected SNR values are therefore high and are not comparable to vicarious calibration experiments derived SNR values using the sun as an illumination source. The setup used in the laboratory is optimized for field measurement situations. This includes the averaging settings as well as the luminance settings (Si integration: 1, PbS integration: 8, averaging: 9).

The dynamic range of the radiometer is approximately 30'000 DN's before

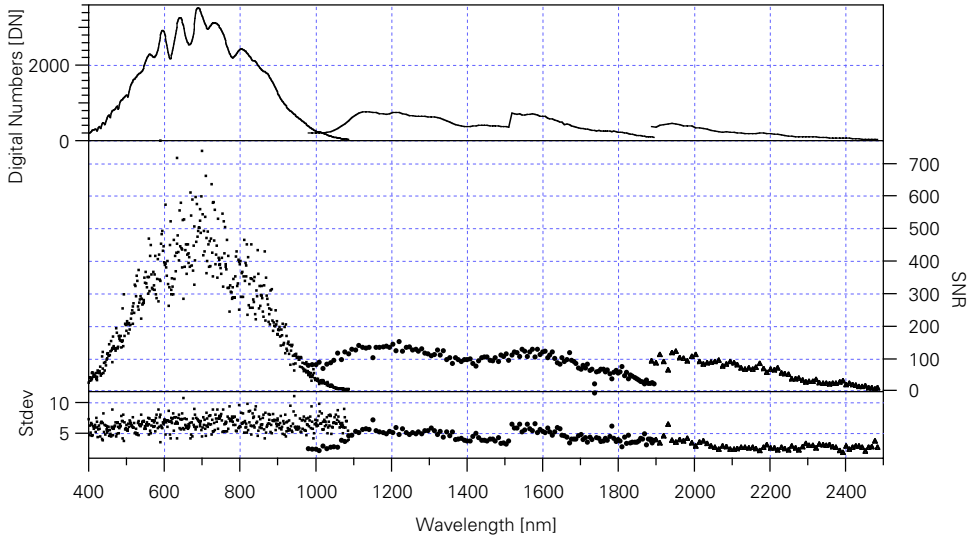


Figure 4.5: SNR determination using 200 fL luminance setting.

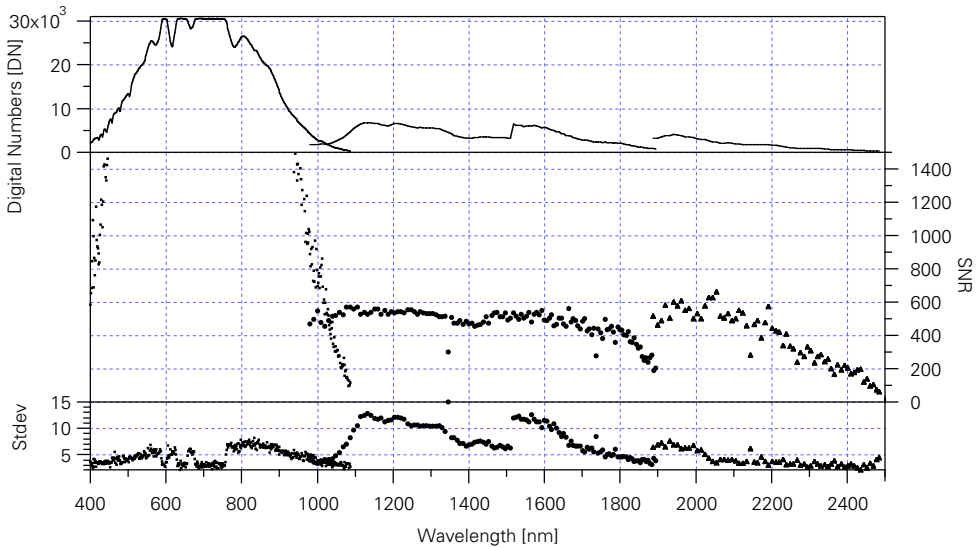


Figure 4.6: SNR determination using 2200 fL luminance setting.

saturation of the Si detector. Using the 200 fL luminance setting, the values do not exceed 3'000 DN's. The resulting SNR values are plotted in Figure 4.5 using the scale on the right side. Averaging all individual detector channels, the mean SNR for each detector are listed in Table 4.3.

SNR vs. Detector	Si Detector	PbS1 Detector	PbS2 Detector
Average SNR at 2200 fL (n=38)	≥ 3493	471	377
Average SNR at 200 fL (n=64)	219	93	59

Table 4.3: Average SNR over all detector channels.

NSR vs. Detector	Si Detector	PbS1 Detector	PbS2 Detector
Average NSR at 2200 fL (n=38)	≤ 0.03%	0.21%	0.27%
Average NSR at 200 fL (n=64)	0.46%	1.08%	1.69%

Table 4.4: Corresponding noise-to-signal of the SNR measurements.

The determination of the corresponding noise present in these two configurations is calculated using NSR (noise to signal ratio). The measurement noise therefore is listed in Table 4.4 for each detector individually.

The estimated NSR is < 0.5% and for the 2200 fL measurements as well as for the Si detector in the 200 fL measurement the values are better than the estimation. Both PbS detectors at low radiance levels exhibit more noise. In this case, it is possible to program the spectroradiometer to a longer integration time and therefore reduce the noise proportional to eq. (4.2):

$$NSR = \frac{N}{S} \propto \frac{1}{\sqrt{\tau}} \tag{4.2}$$

where

τ Integration time of the spectroradiometer.

4.6.2 Noise Equivalent Signal (NES) and Noise Equivalent Radiance (NER)

a) Introduction

In some cases it might be interesting to obtain details about one specific SNR level: SNR = 1. This level is referred to as the noise equivalent signal. If the measurement of the SNR is performed using radiances, the term noise equivalent radiance, or NER, is used.

b) Theory

The formulae for NES and NER can be derived from eq. (4.1) by setting $SNR = 1$. Therefore, they are given as:

$$NES = \sqrt{\sigma^2(R_{DN, total}) + \sigma^2(R_{DN, dark})} \tag{4.3}$$

$$NER = NES \cdot C_{gain}$$

where

NES	Noise Equivalent Signal
NER	Noise Equivalent Radiance
C_{gain}	Calibration gain (discussed in section 6.3).

c) Measuring the NES

The measurement technique used for the NES is a side product from the SNR and dark current measurement (see section 4.6.1). The standard deviation from the SNR measurements is used to calculate the NES, whereas the NER is calculated using the calibration gain for the spectroradiometer.

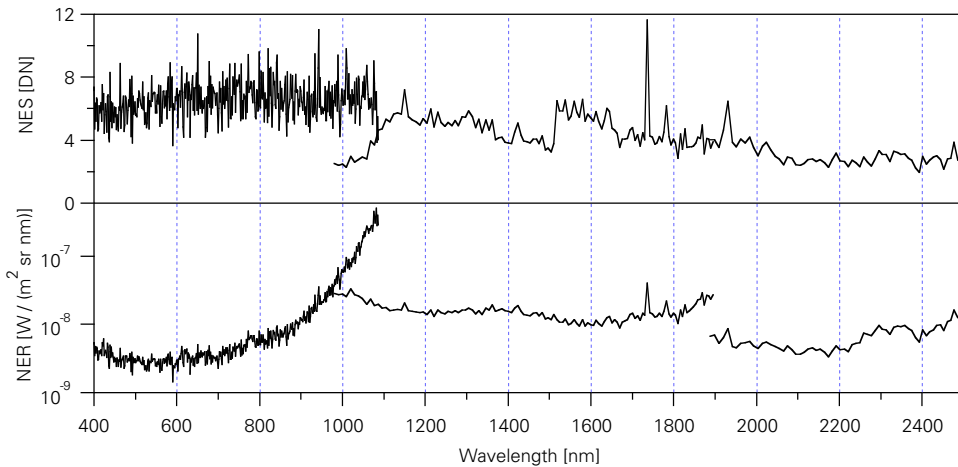


Figure 4.7: NES and NER for the GER3700 spectroradiometer.

d) Results

The NES has an average values of 5 DN, which is in fact not much different from the dark current (approx. 1.5 DN, see next chapter). The instruments sensitivity in general can therefore be stated as excellent, given a noise of approx. 3.5 DN.

4.6.3 Dark Current or Dark Signal

a) Introduction

A measurement performed with no input signal applied is called a dark current, or dark signal measurement. It is achieved simply by closing the shutter of the integrating sphere and subsequently measuring the resulting signal. It is important to verify that no stray light is incident between the sphere and the fore-optics of the spectroradiometer. The measured signal is a combination of radiometric and electronic offset and must be compensated for.

b) Theory

The dark current is defined as the average of all measurements where no input

signal is incident on the instrument. This is performed either with closing the shutter of the integrating sphere when the instrument is attached to the sphere or by completely darkening the aperture of the spectroradiometer using a black cap or similar means:

$$R_{dark} = \frac{1}{n} \cdot \sum_{i=1}^n R_0 = \overline{R_0} \tag{4.4}$$

where

R_0 is the measured signal with no flux incident on the instrument (shutter closed).

c) Dark Current Measurement

The dark current of the spectroradiometer is defined using the instrument attached to the integrating sphere calibration standard. A black anodized aluminum baffles the fore-optics of the spectroradiometer to the sphere. The sphere is optically separated from the lamp using a shutter. By leaving the shutter closed, the measurements are performed.

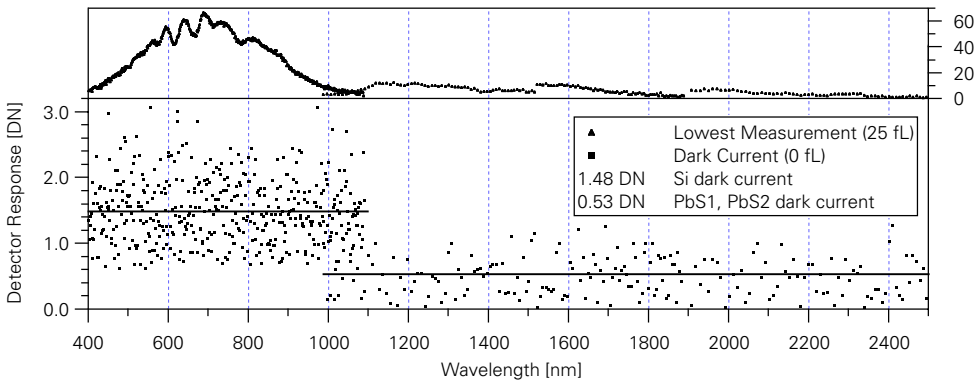


Figure 4.8: Dark current (bottom) and lowest measured signal (upper).

d) Results

Since the GER3700 has a built in offset subtraction, the total dark current measured is extremely low. The average dark current is for all channels less than 1.5 DN. Compared with the saturation level around 30'000 DN, the dark current measured (n=138) is negligible. Figure 4.8 plots the dark current measured in the lower part (sphere luminance = 0 fL) and in the upper part the lowest possible signal generated by the sphere (sphere luminance = 25 fL). This signal already significantly differs from the dark current.

e) Conclusion

The measured dark current is almost negligible. Due to the inherent capability of the spectroradiometer subtracting the dark current, neglecting an electronic or

radiometric offset contributes only marginally to the total uncertainty. Nevertheless, the dark current is included in the final error budget of the instrument.

4.6.4 Wavelength Calibration and Spectral Sampling Interval

a) Introduction

There is a classical discussion on the spectral resolution and spectral sampling interval of a spectroradiometer. The full width at half maximum (FWHM) of the point spread function (PSF) is the definition of resolution given a Gaussian or Lorentian shaped bandpass or response function. The spectral sampling interval is the measure of distance (in wavelength units) between two adjacent points sampled in the spectrum. The center wavelength finally is the peak response of the radiometer to an infinitely small emission line (see Figure 4.9).

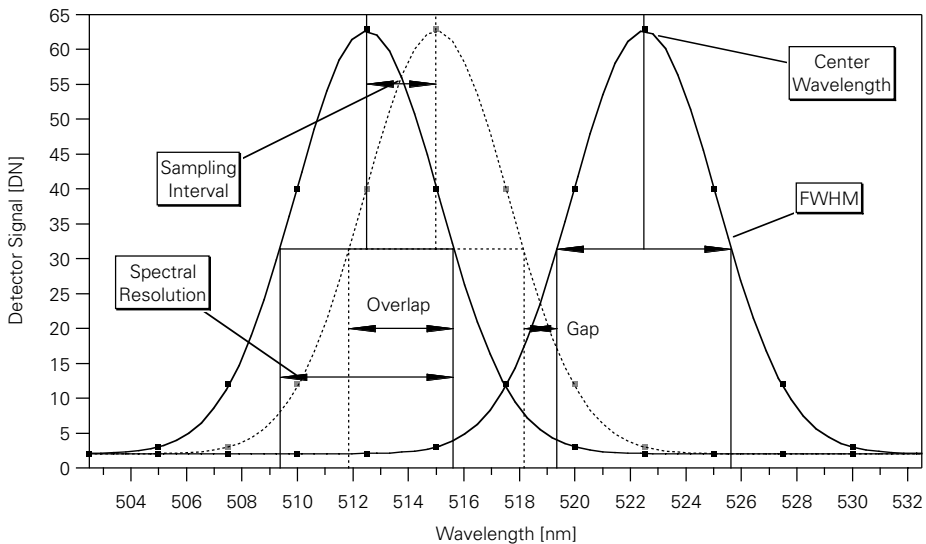


Figure 4.9: Spectral resolution, spectral sampling interval, FWHM, and center wavelength of a Gaussian response function.

Important for spectroradiometric measurement techniques is that each FWHM overlaps to a defined extent ($\leq 50\%$ of the FWHM) the following FWHM. Otherwise the spectrum is oversampled and fully overlapping bands could be eliminated. If there are gaps between the spectral resolution intervals, the spectrum is undersampled and irreproducible errors in sampling the spectrum are introduced [46].

A wavelength error is due to the misassignment of the wavelength of the spectrum of the grating (or filter) in the radiometer and has an error in its wavelength setting. In general, this error is eliminated using one or more atomic emission lines from either a discharge lamp or a hollow cathode lamp. The wavelengths of

most atomic emission lines are known with an accuracy that exceeds the requirements of radiometric calibrations.

The spectral response function of a channel is now used to describe the response of the sensor to monochromatic light being scanned over wavelength. In the ideal case, this response function has a rectangular response. Using a rectangular response function, the FWHM would be the function itself. In most cases, however, the spectral response function can be approximated using a Gaussian model. The spectral resolution of a spectroradiometer with a Gaussian spectral response function corresponds then to the FWHM. It is not advisable to use the measure FWHM for instruments not having a Gaussian spectral response function.

A good measure is the relation between the FWHM and the Gaussian spectral response function [81]:

$$D_{\lambda,eff} = \frac{[\int R(\lambda)d\lambda]^2}{\int R^2(\lambda)d\lambda} = 1.5054 \cdot D_{\lambda,FWHM} \quad (4.5)$$

where

$R(\lambda)$	Spectral response function (must be Gaussian)
$D_{\lambda,eff}$	Effective spectral resolution
$D_{\lambda,FWHM}$	FWHM.

If the FWHM of two neighboring channels do not overlap each other, the spectrum is not contiguously sampled and this gap is referred to as undersampling. In the other case, where the FWHM overlaps more than 50%, the spectrum is oversampled. In spectroradiometric applications it is most desirable that none of the above cases holds true.

There are many other standards available to calibrate the sampling interval, the spectral resolution and the center wavelength [10][12][50][81][100][124]. The focus for this calibration experiment is on the use of a tunable dye laser.

b) Lasers used for Wavelength Calibration

Lasers produce a highly directional and high-intensity beam that has a very narrow wavelength range. The SNR is usually excellent and they expose also a highly collimated beam. Lasers therefore make up one of the best wavelength calibration devices. Unfortunately the wavelength range covered by lasers is limited and their operation is very expensive.

More of a problem is the typical Gaussian beam profile of a laser, which must be taken into account to avoid saturation of single detector elements. In order to use a laser as a radiation source, one must use a beam splitter and a stable detector in the optical system near the radiometer since lasers are not particularly stable sources. The detector serves to monitor the laser beam power and can be used to actively stabilize the system.

c) Tunable Dye Laser

The dye laser used for this calibration is pumped by an argon-ion laser that pro-

vides a single-mode laser beam with a linewidth of about 1 MHz. The pumped argon-ion laser light travels through a reference cavity, where Rhodamine 6G is used as dye. Exiting the cavity, a single-mode laser beam with a linewidth of about 1 MHz is available for the experiment [16]. The tunable wavelength range is between 450–750 nm. The minimum data point increment is 1 MHz. The experimental setup is displayed in Figure 4.10, and pictures of the laboratory given in Figure 4.11. Preliminary analysis showed too much radiant power on the radiometer so that a power reduction method using a polarizer/ $\lambda/2$ /polarizer combination had to be introduced. In a next step the laser beam is split and focused with one beam on a photomultiplier to read out intensity variations over time. The other beam is collimated and focused on the entrance optic of the spectroradiometer.

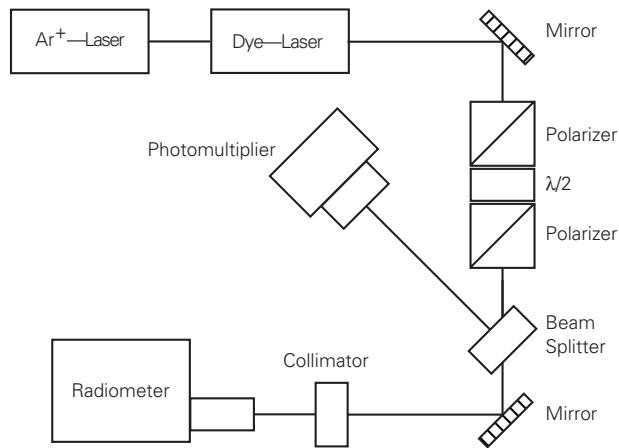


Figure 4.10: Tunable dye laser setup for the wavelength calibration.

The accuracy of the dye laser is around 1 GHz. The refraction index used is in air and the spectral sampling interval of the laser is set to 1 nm. The total wavelength range covered by the laser in this case is 584.1–596.4 nm. The limited range is due to problems with the recalibration and the refreshment process of the dye. Every measurement taken is normalized to the same energy level as recorded by the photomultiplier to level out the intensity variations over time.

d) Center Wavelength

The center wavelength measurement is performed using the laser and scanning the wavelength range covered by the laser in 0.1 nm increments. 124 data points in the spectrum are covered.

Figure 4.12 displays the response of the spectroradiometer to the laser at 593.6 nm. The peak signal is at over 5'000 DN compared to the background signal of about 10 DN (i.e. SNR = 500). There is minor asymmetry in the response of the spectroradiometer to the laser line due to many intermediate optical elements in the optical path of the laser.

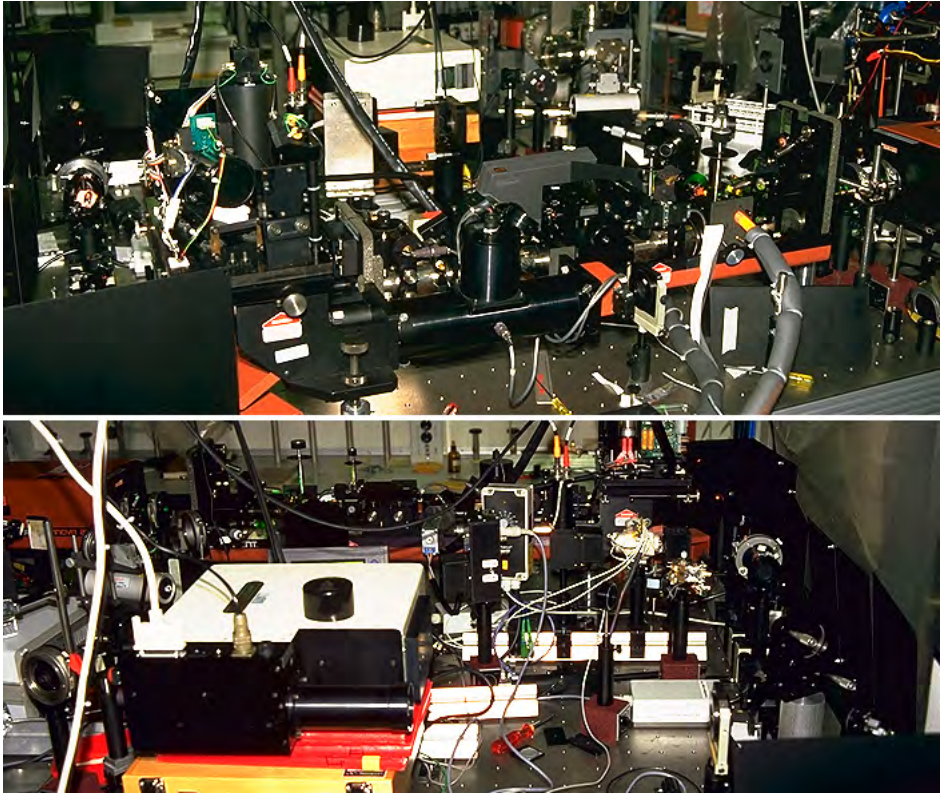


Figure 4.11: Tunable dye laser laboratory setup: cavity (top) and spectrometer (bottom).

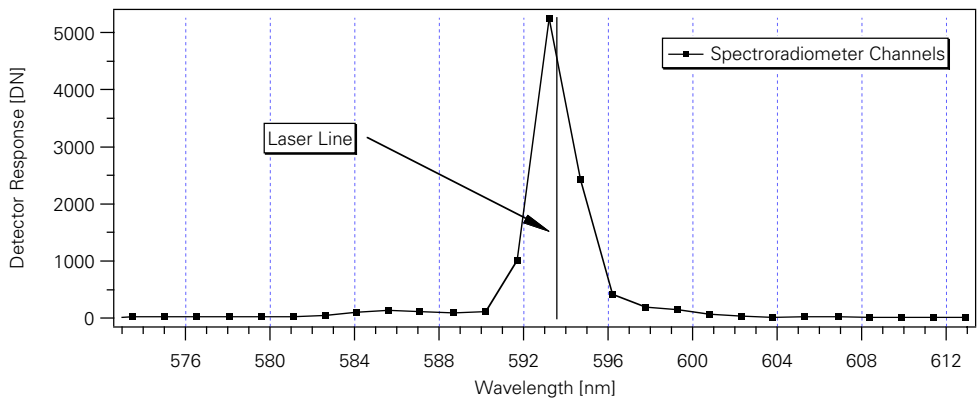


Figure 4.12: Spectroradiometer response to a dye laser line at 593.6 nm.

As the spectroradiometer is operated in a temperature stabilized environment, no significant changes of operating temperature are observed. Errors due to temperature effects are considered to be minor.

The wavelengths determined using the laser are then plotted against the original provided data. The differences measured by the laser are modeled and fitted against the original data as follows:

$$\lambda_{GER} - \lambda_{Laser} = k_0 + k_1 \cdot \lambda_{GER} \quad (4.6)$$

where

- λ_{Laser} Wavelength of the laser
- λ_{GER} Wavelength of the spectroradiometer
- k_n Linear fit parameters.

The updated wavelengths measured with the laser can then be extrapolated using:

$$\lambda_{Laser} = \lambda_{GER} - k_1 \cdot \lambda_{GER} - k_0. \quad (4.7)$$

The first measurement near 584 nm is excluded from the fit (see Figure 4.13).

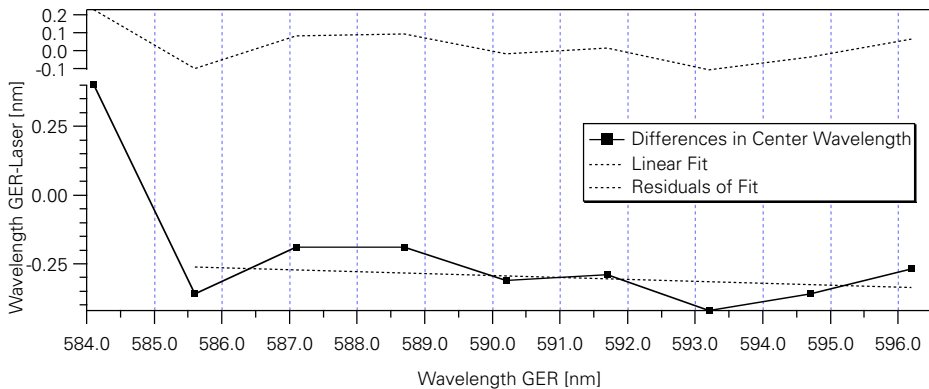


Figure 4.13: Differences between laser and spectroradiometer center wavelength.

The reason for this is because of the measurement of the spectral response function for this channel. The center wavelength is not determined from a single emission line but corresponds to the center position of the Gaussian fit which is discussed in the next chapter. Because the laser measurements started only at 584.1 nm, the left part of the Gaussian function for this channel could not be determined with sufficient accuracy.

The update of the center wavelength is within the range of ± 0.15 nm in the measurement interval. In general, the center wavelengths measured by the laser are higher than the provided values. The extrapolation of the derived fit to all channels is critical and must be interpreted with care. Even though the wavelength range covered by the laser is approximately in the middle of the detector,

a much more robust determination of center wavelengths is the interpolation from the outer wavelengths (e.g. around 400 and 1080 nm). The extrapolation would introduce a very high uncertainty. The following equation is the result of the fit and without introducing any additional uncertainties extrapolated to the whole Si detector:

$$\lambda_{Laser} = \lambda_{GER} - (-0.00697 \pm 0.00854) \cdot \lambda_{GER} - (3.82 \pm 5.05). \quad (4.8)$$

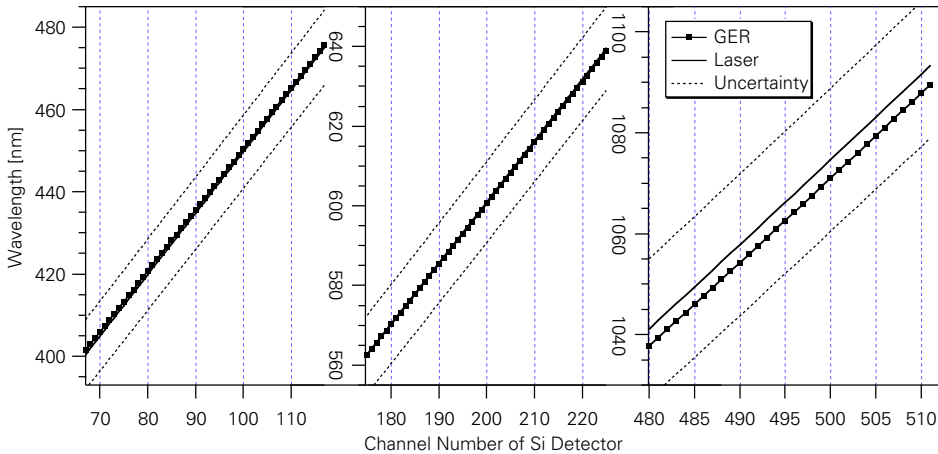


Figure 4.14: Extrapolation of center wavelengths to the Si detector.

Figure 4.14 demonstrates the uncertainty introduced by extrapolating the measured center wavelengths to the full detector. The uncertainty and disagreement in the upper range (channels 480–512) are unacceptably high.

A more powerful method would make use of a discharge lamp having a number of sufficiently strong lines in the 400 and 1100 nm region of the spectrum for proper wavelength characterization. As a consequence of this extrapolation effort, only the determined wavelengths are substituted by the original ones (interval {585...597} nm).

e) Results

The expected uncertainty of the center wavelength is estimated at $< 0.6\%$. The determination of the exact position is better than 0.05% and is used for the final uncertainty calculation. Since these measurements have been performed only twice within a total period of three days, no information on the instability or drift of these wavelengths can be given over time. It must be assumed that the drift could significantly increase this uncertainty.

f) Spectral response function

The spectral response function is measured using the same approach as described above. The only difference is that after normalizing the data the response of adjacent channels of the spectroradiometer is plotted to the laser emission line.

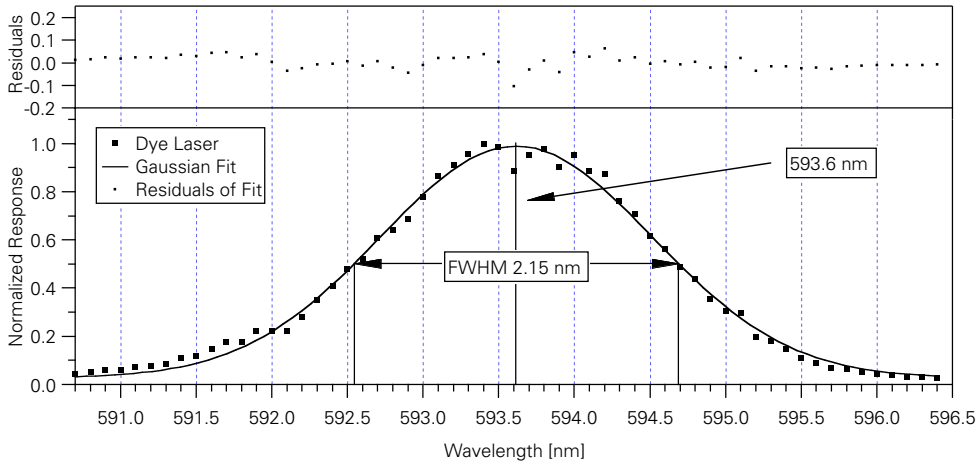


Figure 4.15: Gaussian fit and FWHM determination for 593.6 nm.

Figure 4.15 visualizes this process for one channel of the spectroradiometer (593.6 nm). The model used to derive the response function is a Gaussian fit to the normalized data. The peak of the Gaussian function is determined by the new center wavelength:

$$R_{DN} = k_0 + k_1 \cdot \exp\left(-\left(\frac{\lambda_{GER} - \lambda_{Laser}}{k_3}\right)^2\right) \quad (4.9)$$

where

R_{DN} is the response of the spectroradiometer.

This model is applied to the same wavelength range as in the center wavelength characterization and all the fits properly converged. The coefficients and uncertainties for the fit at 593.62 nm are given with:

$$k_0 = 0.026854 \pm 0.00263$$

$$k_1 = 0.96203 \pm 0.00726$$

$$k_2 = 593.62 \pm 0.00758$$

$$k_3 = 1.2742 \pm 0.0118$$

where

$$k_2 = \lambda_{Laser} \text{ Center wavelength from this fit using 123 measurement points.}$$

The FWHM finally is determined by solving eq. (4.9) for $R_\lambda = 0.5$. The resulting data are plotted by channel number against wavelength (Figure 4.16).

Assuming that the combination of a diffraction grating and a line array have a distinct geometrical alignment, the center wavelength distribution is a function of linear positions on the line array. In this assumption, effects such as the non-uniformities in the detector spacing or irregularities in the grating are neglected.

The grating therefore creates a linear dispersion on the line array and each

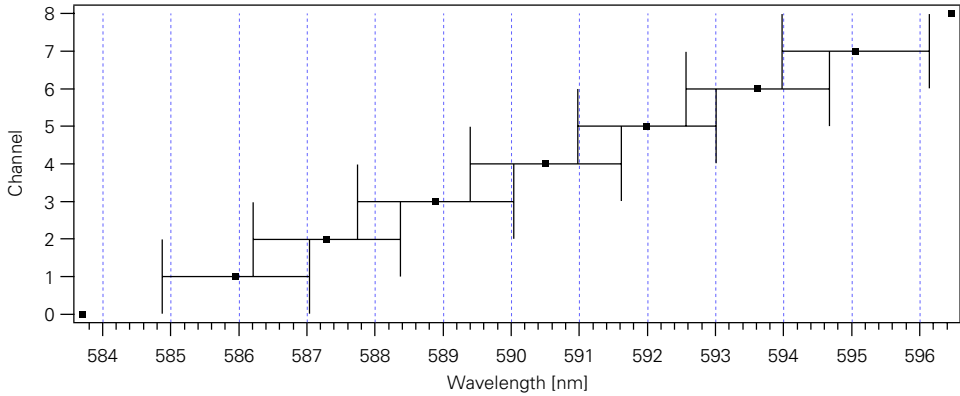


Figure 4.16: Center wavelength and FWHM for selected channels.

detector element is associated with a distinct spectral band based on the spatial extent of each element. Given this relation, and including the effects for spectral scattering, there is a constant relation between the FWHM and the center wavelength of each spectral band:

$$\lambda_{FWHM}(i) \propto \frac{\lambda_{i+1} - \lambda_{i-1}}{2} \quad (4.10)$$

where

$\lambda_{FWHM}(i)$ FWHM of the spectral channel i
 λ_i Center wavelength of channel i .

Following the diffraction grating equation, the angular dispersion of a grating is constant [65], so that the following relation can be used to determine the FWHM for all channels, extrapolated from the above determined channels:

$$const = \frac{(\lambda_{i+1} - \lambda_{i-1}) / 2}{\lambda_{FWHM}(i)}. \quad (4.11)$$

The updated FWHM values will then take into account all the spectral scattering effects together with relation derived from eq. (4.11).

g) Results

The significantly decreasing FWHM in the two PbS detectors is possibly due to a slight tilting of the detectors against the gratings. In many cases this tilting is done intentionally to reduce reflections originating from the detector surfaces, and reflected again from the grating to the detector, thus causing multiple internal scattering effects. Accurate determination of the center wavelength and the spectral resolution is an important task with respect to the total calibration uncertainty expected. Small variations within a few percentages significantly influence the overall calibration uncertainty [38]. This task must therefore be well designed

and planned in the characterization process of the instrument. Figure 4.17 displays the original and calibrated FWHM against (calibrated) wavelengths.

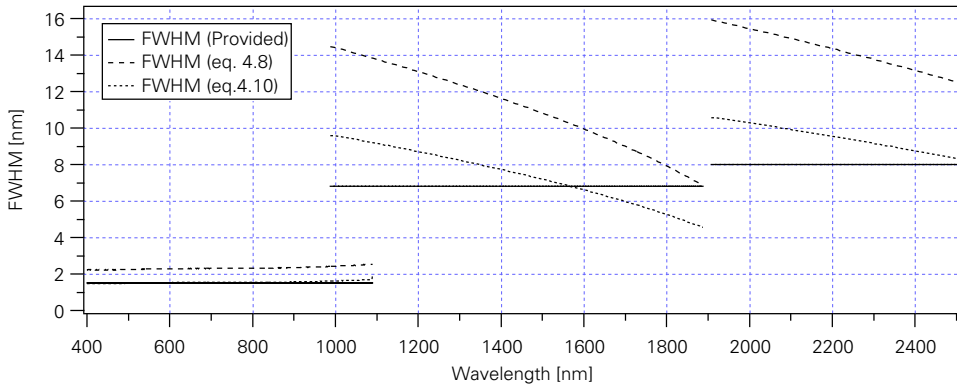


Figure 4.17: Original and calibrated FWHM (y-axis) and center wavelengths (x-axis) for each spectroradiometer channel.

4.6.5 Nonlinearity

a) Introduction

Based on the measurement equation (2.2), the responsivity R can change if the radiant power L_λ changes. If this is the case, S —the output signal of the spectroradiometer—is no longer proportional to L_λ and is therefore nonlinear. In the worst case, it is necessary to deduce a non-linearity function for each channel of a spectroradiometer. Nonlinearities usually arise from detectors and/or signal processing units.

To quantify the nonlinearity of an instrument, it is necessary to verify that the calibration is performed at the same radiant power level. Usually field measurements cover a broad range of power levels, therefore making it necessary to repeat the calibration for each level in order to delineate and verify the nonlinearity function.

The typical form of a nonlinearity appears as a saturation at high irradiance levels (see Figure 4.18). It is desirable that the radiometer saturates only at radiance levels that are not to be expected in reflectance measurements. Caution must be taken not to point instruments that are optimized to measure reflectance directly to the sun. Saturation might be harmful to the performance of the system and could degrade the performance for future measurements. At low radiance levels what often appears to be a nonlinearity may only be the result of failing to apply a dark signal or offset correction. Here it is advantageous to design the instrument in a way so that systematic and random noise remain below the lowest reflectance to be measured. The NER is a good measure for the lower sensitivity of an instrument.

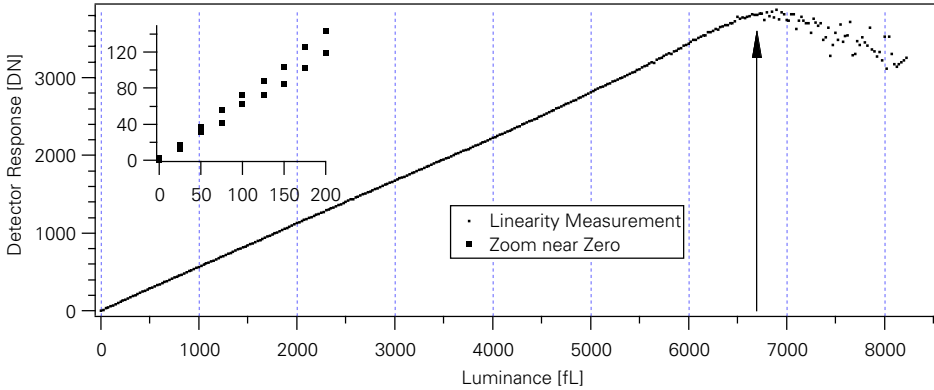


Figure 4.18: Linear (75–6700 fL) and non-linear regions (< 75 and > 6700 fL) for one selected channel (568 nm).

A spectroradiometer having a linear response from the lowest expected radiance (i.e. 1–1.5% reflecting target) up to the highest (100% reflecting target, such as a Spectralon panel) avoids nonlinearity discussions. Since most field instruments make use of a reflectance standard, 100% reflectance must be taken into account even though typical reflectances will rarely exceed 60% reflectance. As a consequence, in the present design of spectroradiometers there is a lot of the dynamic range of the instrument seldom accessed (60–100% reflective targets). Detectors having an exponential response might optimize the use of the dynamic range of these instruments.

b) Theory

There are a number of measurement techniques available to determine the non-linearity of a spectroradiometer. One of the easiest techniques is the use of the inverse square law—because the irradiance of a source varies inversely with the square of the distance from the source to the entrance aperture [50]. This method is primarily suited for irradiance measurements and can not be performed using an integrating sphere. Other methods include the measurement of the transmittance of two polarizers or chopping apertures of determined size on a rotating disk [123].

A very powerful method—if an integrating sphere is available—is a nonlinearity measurement by the superposition of sources method [82]. This method assumes that if the radiometric system is linear, the arithmetic sum of the individual signals measured at different radiance levels is equal to the radiance if all signals irradiate the radiometer at the same time.

A linear system would follow the following equation:

$$K_{ab} = \frac{i_{(a+b)}}{i_a + i_b} \quad (4.12)$$

where

- K_{ab} Nonlinearity correction factor
- i_a, i_b Individual sources
- $i_{(a+b)}$ Combined sources.

Following the measurement equation, the responsivity and the radiant power are given with:

$$i_a = R \cdot L_a. \quad (4.13)$$

And for measurements at different radiances:

$$i_{(a+b)} = K_{ab} \cdot R \cdot L_{(a+b)}. \quad (4.14)$$

This process will be repeated until the full dynamic range of the radiometer is covered.

c) Modelling the Linearity Measurement

Following the superposition of sources method, the expected radiance levels of the field measurements have been estimated and plotted against integrating sphere radiance values. Based on these calculations, the dynamic range of the calibration can be fixed. A major drawback when using an integrating sphere calibration standard is that the spectral radiance has a given spectrum based on the tungsten halogen lamp source (see Figure 4.19). Since the individual detector sensitivity of the Si and PbS detectors does not correlate with the tungsten spectrum, the best trade off between saturation and noise of the detectors is selected.

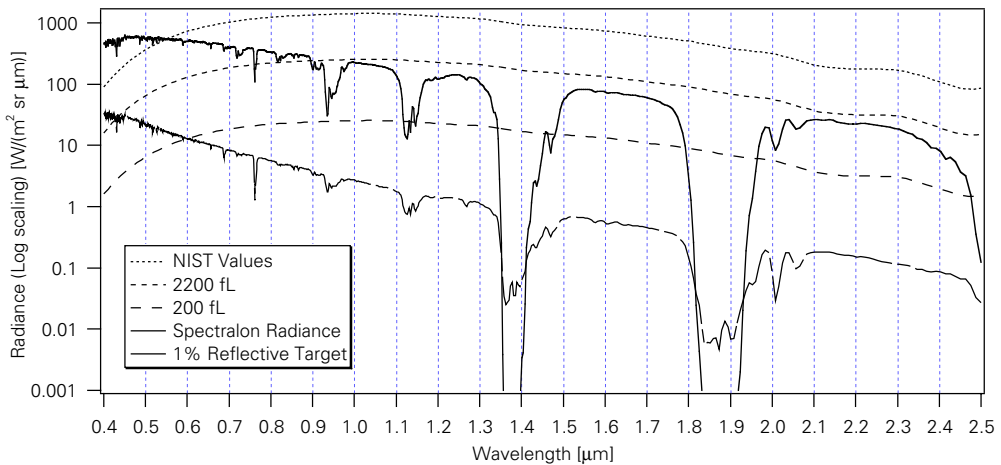


Figure 4.19: Comparison of NIST radiance values [64], calibration radiances and modeled Spectralon [53] radiances .

The Spectralon typical radiance is modeled using MODTRAN [6], with an optimal transmittant atmosphere at 2 m above the ground. The NIST provided original radiance levels (luminance > 12'000 fL) saturate the instrument in all

channels. Therefore the NIST radiance level in the integrating sphere is reduced to 2200 fL (maximum) and 200 fL (minimum) level. This reduction is based on the expected radiance levels measuring under real conditions. The total dynamic range in reflectance values can be visualized by plotting different typical reflectances (see again Figure 4.19).

Since the radiometer has different sensitivity settings for the detectors, three different sensitivity setups have been measured individually. The above-mentioned equations can be adapted for the different sensitivity levels, allowing for a cross check if changing the sensitivity of the instrument does not affect the linearities:

$$k_s \cdot i_{a+b} = K_{k_s ab} \cdot R \cdot L_{k_s(a+b)} \tag{4.15}$$

where

k_s Sensitivity correction.

d) Linearity Measurement

The linearity measurement is performed using the integrating sphere calibration standard. Starting the measurements at input radiances of 0 up to 8300 fL in steps of 25 fL, resulting in 658 measurements for the lowest sensitivity setting. Each sensitivity level is measured starting from 0 in increments up to the saturation level and then back the same way down to zero. In total three different sensitivity levels of the spectroradiometer are measured (e.g. corresponding detector integration times are given as 1, 4, and 8 times), and plotted in Figure 4.20.

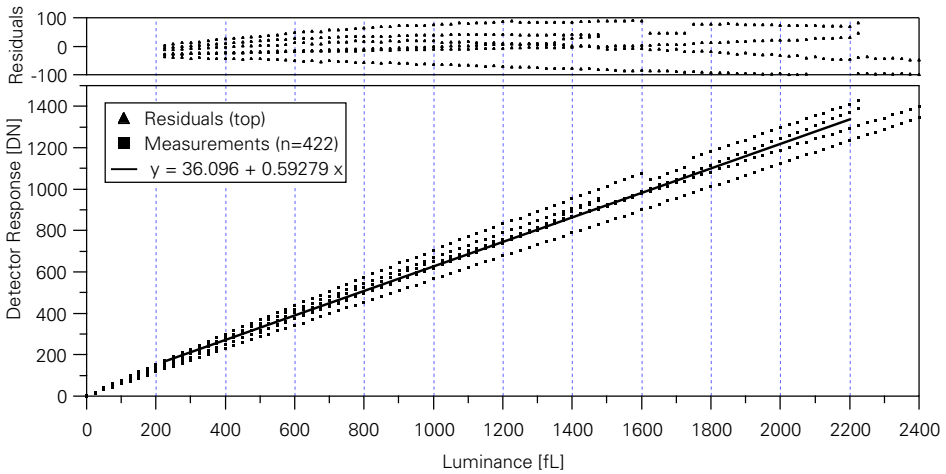


Figure 4.20: Linearity fit and residuals within the predefined calibration range of the spectroradiometer.

The (linear) fit for the 422 linearity measurements (restricted to the calibration interval between 200–2200 fL) at different sensitivity levels results in the following equation:

$$R_{DN} = (36.096 \pm 5.16) + (0.59279 \pm 0.00411) \cdot L_{fL}. \quad (4.16)$$

e) Results

In a next step, the nonlinearity correction factor K_{ab} is calculated including the sensitivity correction. The baseline for calculating K_{ab} is the average of all measurements at a certain luminance and not the fitted linear range.

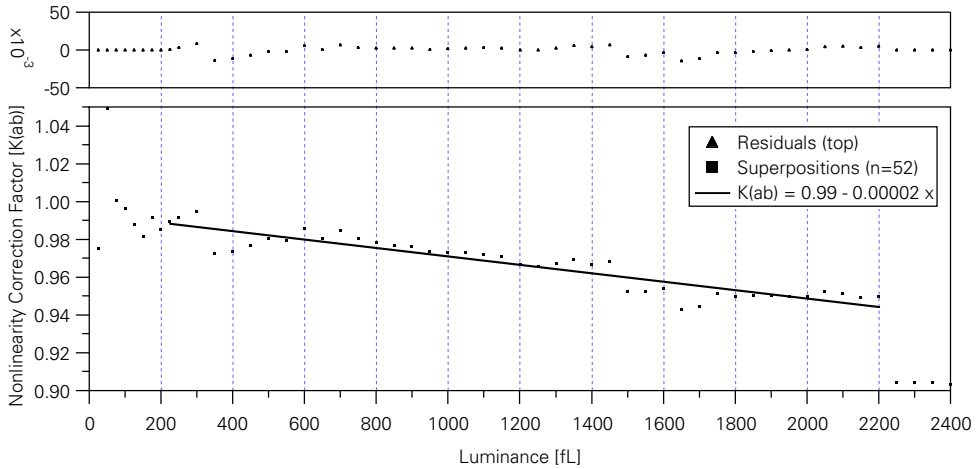


Figure 4.21: Nonlinearity correction factor within the calibration range.

The resulting correction factors for the measured range between 0–2400 fL, again restricted to the calibration interval between 200–2200 fL can be expressed in the following equation using 52 superpositions (see Figure 4.21):

$$K_{ab} = \langle 0.9934 \pm 0.00198 \rangle - (2.2214 \cdot 10^{-5} \pm (1.48 \cdot 10^{-6}))L_{fL} \quad (4.17)$$

The major uncertainty of the superposition of sources method is introduced by the different sensitivity levels of the radiometer. A comparison of isolated sensitivity levels demonstrates a much better linearity within the levels then summing the individual levels up. Nevertheless, the total linearity in the observed interval between 200–2200 fL is excellent, but the extrapolation to lower or higher values is not advisable.

Nonlinearity is measured and modeled for all 704 channels. For convenience and readability, the remaining 703 channels are not presented here.

f) Conclusion

The estimated uncertainty for the nonlinearity is $\leq 0.5\%$, meaning that if the nonlinearity exceeds 0.5%, the measurement equation must be modified for non-linear behavior of the instrument. The modification of eq. (2.2) would incorporate the responsivity as a function of the incident flux. The nonlinearity can be

assessed using a polynomial determined by the nonlinearity coefficients $\{a, b, c, \dots\}$:

$$S = L_\lambda \cdot \Delta\lambda \cdot \Delta A \cdot R(\Phi) \quad (4.18)$$

$$S(1 + aS + bS^2 + cS^3 + \dots) = R_0 \cdot L_\lambda \cdot \Delta\lambda \cdot \Delta A \quad (4.19)$$

where

a, b, c, \dots Nonlinearity coefficients determined by measurements of known radiance standards at different radiance levels.

The calculated nonlinearity for the three detectors of the spectroradiometers is the result of 52 superpositions for each of the 704 channels. The resulting average nonlinearity is 0.20% for the Si detector, 0.39% for the PbS1 detector and 0.44% for the PbS2 detector. Based on these nonlinearity values, the spectroradiometer is considered to be a linear measurement device.

4.6.6 Directional and Positional Effects

a) Introduction

Sometimes the responsivity of the incident radiation on the spectroradiometer is dependent on its position and direction on the fore-optics. In this case a special correction must be evaluated for each positional and directional difference of incoming radiation.

The most popular calibration device to avoid these effects is the integrating sphere calibration standard. Because of its averaging capabilities, the responsivity of the spectroradiometer correctly coupled to the sphere will be invariant with direction and position (see chapt. 4.3.2).

b) Directional and Positional Measurement

The experimental setup measuring the directional invariance of responsivity involves the positioning of a small stable source at different locations over the acceptance angle before the integrating sphere.

The invariance of the position in the fore-optics is measured using a black plate with a hole in it, positioned at different places over the entrance aperture. If the signal remains constant while moving around, the responsivity is invariant with position [50].

c) Conclusion

While using an integrating sphere for the characterization of the spectroradiometer, directional and positional effects may be neglected. The contribution of these effects is estimated to be less than 0.5%.

4.6.7 Spectral Scattering

a) Introduction

Spectral scattering occurs if a measurement is taken at a specific wavelength λ

with a bandpass of λ_{FWHM} . Then some flux from outside of λ_{FWHM} is scattered onto the slit and contributes to the total signal. Spectral scattering effects are only significant if there is a large flux outside of λ_{FWHM} relative to the one within λ_{FWHM} [50].

b) Spectral Scattering Measurement

The experimental determination of scattered flux involves the use of filters. These filters must be designed to have a transmittance close to 0 at the wavelength of the observed center wavelength of the spectroradiometer and a high transmittance at the wavelengths of the scattered flux. Using a spectroradiometer with over 700 channels would therefore require the same amount of specifically designed filters.

An alternative approach is to use a laser as an isolated line source. The tunable dye laser source is a good measurement instrument to determine the responsivity of the spectroradiometer including the spectral scattered light. Assuming that the response of the spectroradiometer is not only a function of one wavelength but of two, the responsivity is updated as follows:

$$R_{(\lambda_0, \lambda)} = \frac{dS(\lambda_0)}{d\Phi(\lambda)} \quad (4.20)$$

where

- $R_{(\lambda_0, \lambda)}$ Responsivity of the spectroradiometer to two wavelengths
- $dS(\lambda_0)$ Output signal for a wavelength λ_0
- $d\Phi(\lambda)$ Incident flux at wavelength λ .

Measuring isolated laser lines corresponds to the simple measurement equation (eqs. (2.1), (2.2)). The flux of the laser line can be determined using a silicon photodiode as described in Figure 4.10:

$$R_{(\lambda_0, \lambda)} = \frac{dS(\lambda_0)}{d\Phi_{Laser}(\lambda)}. \quad (4.21)$$

Measurements at sufficient λ 's makes interpolation possible over all wavelengths to be observed. The best solution would also be to point the laser into an integrating sphere before pointing on the fore-optic of the spectroradiometer to average the speckle distribution on the entrance slit.

c) Conclusion

The spectral scattering sensitivity of the radiometer is not measured separately but included in the determination of the FWHM using the tunable dye laser (see chapt. 4.6.4). The uncertainty introduced by the contribution of spectral scattering is estimated to be less than 0.5%.

In most cases no tunable laser is available to cover the whole wavelength range of the spectroradiometer due to the limited tuning interval of dye lasers. In this case complex double-monochromators and deconvolution techniques must be used to assess spectral scattering.

4.6.8 Field of View (FOV)

a) Introduction

The field-of-view (FOV) is the solid angle through which radiant flux is accepted by the radiometer, and it depends upon the optical configuration of the radiometer. The FOV is determined by the position of the entrance aperture stop relative to the detector area which serves as the field stop [80].

b) Theory

If the detector radius is small with respect to the focal length of the spectroradiometer, then the field of view angle of the radiometer can be given as:

$$\theta_f = 2 \tan \left[\frac{r_d}{f} \right] = 2 \tan \left[\frac{r_t}{h} \right] \quad (4.22)$$

where

θ_f	Field-of-View
f	Focal length
r_d	Detector radius (assuming $r_d \ll f$)
r_t	Spot radius of the target
h	Measurement altitude.

The solid angle defined by the FOV is calculated using:

$$\omega = \frac{\pi}{4} \cdot \tan^2 \left(\frac{\theta_f}{2} \right) \quad (4.23)$$

where

ω	Solid angle.
----------	--------------

The target diameter and the target area covered by the spectroradiometer is a function of the measurement altitude (h) and is expressed as:

$$d_t = 2 \cdot r_t = 2 \cdot h \cdot \tan \left(\frac{\theta_f}{2} \right) \quad (4.24)$$

$$A_t = \pi \cdot h^2 \cdot \tan^2 \left(\frac{\theta_f}{2} \right) \quad (4.25)$$

where

d_t	Target diameter
A_t	Target area.

The flux incident on the detector from a distant isotropic and uniform source is dependent on two radiometric characteristics—the lens area and the FOV plane angle (the geometric relations of the FOV are displayed in Figure 4.22). The flux is independent of the distance from the target [17]:

$$\Phi = \pi \cdot L \cdot A_a \cdot \sin^2 \left[\frac{\theta_f}{2} \right] \tag{4.26}$$

where

- Φ Flux incident on the detector
- L Radiance of source
- A_a Area of the lens.

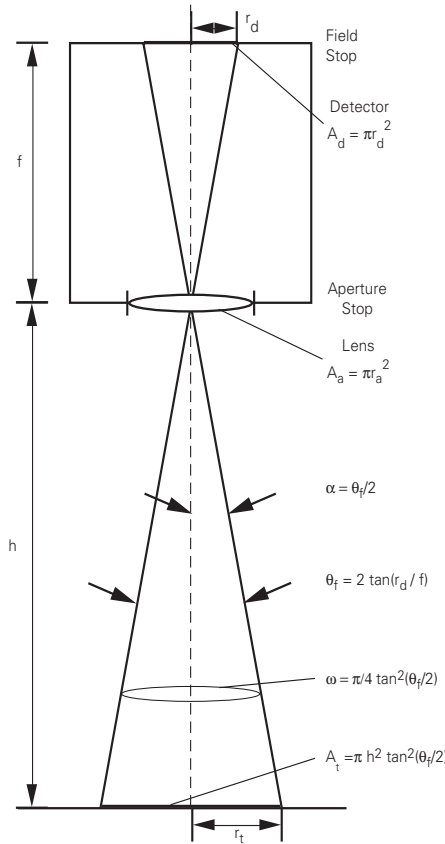


Figure 4.22: Geometric relations of the field-of-view for a fixed-focus spectroradiometer.

c) FOV Measurement

The field-of-view (FOV) experiment is carried out in the laboratory using the GER3700 mounted on a tripod. Two 650 Watt quartz-tungsten halogen lamps are used to illuminate the target. Assuming that the FOV of the instrument is completely round, 8 point-symmetrical positions on the ground using the Spectralon panel on a black background are measured for three different altitudes.

The continuously measuring diagnostics mode of the GER3700 software is

used to determine that line on the ground, where the signal increases and the FOV of the instrument covers partially the Spectralon panel. The restrictions that apply for this experiment include the assumption that no adjacency effects exist and no diffuse radiation (except the one from the panel) reaches the lens of the GER3700. In order to measure different contrast types to grant the reproducibility, the same experiment was carried out using a red and yellow paper instead of the black and white setup.

The following figure plots the measurement altitudes versus the distance from the center of the FOV of the GER3700. The distance is determined using the above-mentioned diagnostics mode by subsequently moving the target closer to the center of the FOV.

d) Results

The half FOV angle is calculated using the following equation:

$$\frac{\theta_f}{2} = \tan \alpha = \frac{r_t}{h} \quad (4.27)$$

where

α Half the FOV angle,

and the relation between these parameters is determined using a linear fit:

$$h = k_0 + k_1 \cdot r_t \quad (4.28)$$

where

k_n fit parameters.

The total field of view can then be determined using:

$$\alpha = \operatorname{atan}\left(\frac{h - k_0}{h \cdot k_1}\right) \quad (4.29)$$

$$FOV = \theta_f = 2\alpha = 2 \operatorname{atan}\left(\frac{h - k_0}{h \cdot k_1}\right). \quad (4.30)$$

The measurements (n=21) result in the following fit:

$$h = (45.757 \pm 18.2) + (31.693 \pm 5.43) \cdot r_t. \quad (4.31)$$

The spectroradiometer's geometrical behavior derived after eqs. (4.30), (4.23), (4.24), and (4.25) is given as (see also Figure 4.23):

$$FOV = 1.96(-0.8 | + 1.2)^\circ \quad (4.32)$$

$$\omega = 22.98 \times 10^{-5}(-14.93 | + 36.78)sr \quad (4.33)$$

$$d_t = 6.84(-2.79 | + 4.19)cm \quad (4.34)$$

$$A_t = 36.77(-23.89 | + 58.84) \text{ cm}^2. \quad (4.35)$$

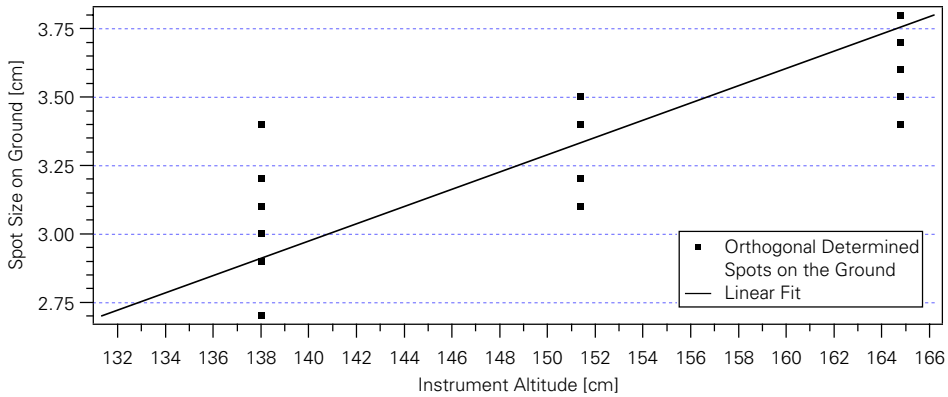


Figure 4.23: Measurement of FOV and the corresponding linear fit.

e) Conclusion

The uncertainty associated with the experimental determination of the total FOV is large, due to the lambertian reflectance properties of the material used and the problematic readout of real time detector data. But since in most experiments the integrating sphere calibration standard is used to perform the measurements, the error associated with the FOV is smaller than 0.1%. The sphere illuminates the FOV homogeneously, and the error associated with the FOV is due to possible drifts and misalignments and not the exact determination of the solid angle covered by the FOV.

Even if using a monochromatic pointable source, such as a generally available pointing laser, the accuracy achieved is not better than in the type of experiment presented here.

4.6.9 Polarization

a) Introduction

There are often significant perturbations of radiant power transfer due to properties of the radiation field other than its geometry. One such possible error is due to the polarization state of the radiation field. The readout signal from a detector that is polarization-sensitive is dependent upon the relative orientation of the polarization state of the radiation with respect to the detector orientation. The emitted radiance from the sun is in most parts of the spectrum unpolarized. The major polarization contribution arises from scattered light resulting mainly in a linear polarization. The total contribution of polarization resulting from scattered light depends on the type of underlying reflectors, the angle of incidence and scatter, the wavelength, and the weather. The degree of polarization can exceed 20%

of the total signal depending on the wavelength and the reflecting objects [21]. In some cases the degree of polarization can be up to 50% or more if directed at water or a light source reflected near the Brewster's angle [5]. The total process of polarization in remote sensing is difficult to quantify since depolarization effects do not allow for a deterministic description of the polarization source. The phenomena of polarization are complex but contains useful information especially in the field of radar polarimetry [42].

b) Theory

The characterization of the spectral radiance relative to their polarization state is done by the Stokes vector S , and the Mueller matrix M to describe the polarization-altering characteristics of the sample.

The Stokes spectral radiance vector is based on flux measurements and is defined for an ideal polarizer as [99]:

$$S = \begin{bmatrix} s_0 \\ s_1 \\ s_2 \\ s_3 \end{bmatrix} = \begin{bmatrix} P_H + P_V \\ P_H - P_V \\ P_{45} - P_{135} \\ P_R - P_L \end{bmatrix} \quad (4.36)$$

where

P_H	Horizontal linear polarizer (0°)
P_V	Vertical linear polarizer (90°)
P_{45}	45° linear polarizer
P_{135}	135° linear polarizer
P_R	Right circular polarizer
P_L	Left circular polarizer.

A Stokes vector measurement is therefore an average over area, solid angle, and wavelength. Based on the Stokes vector, the following polarization parameters have been derived [11]:

Flux

$$P = s_0, \quad (4.37)$$

Degree of polarization

$$DOP = \frac{\sqrt{s_1^2 + s_2^2 + s_3^2}}{s_0}, \quad (4.38)$$

Degree of linear polarization

$$DOLP = \frac{\sqrt{s_1^2 + s_2^2}}{s_0}, \quad (4.39)$$

Degree of circular polarization

$$DOCP = \frac{s_3}{s_0}. \quad (4.40)$$

If now the light, characterized by the Stokes vector, passes through an optical element (i.e. spectroradiometer), it changes its magnitude. The Mueller matrix M transforms the incident Stokes vector S into the exiting Stokes vector S' . The Mueller matrix M characterizes polarization measurements with respect to their polarization properties (i.e. diattenuation, retardance, depolarization) and their form (i.e. eccentricity, etc.)[58]. The Mueller matrix $M_{(k,\lambda)}$ is always a function of the direction of the propagation k and the wavelength λ and is written as [99]:

$$S' = \begin{bmatrix} s'_0 \\ s'_1 \\ s'_2 \\ s'_3 \end{bmatrix} = MS = \begin{bmatrix} m_{00} & m_{01} & m_{02} & m_{03} \\ m_{10} & m_{11} & m_{12} & m_{13} \\ m_{20} & m_{21} & m_{22} & m_{23} \\ m_{30} & m_{31} & m_{32} & m_{33} \end{bmatrix} \cdot \begin{bmatrix} s_0 \\ s_1 \\ s_2 \\ s_3 \end{bmatrix}. \quad (4.41)$$

Solving the transformed Stokes vector for an unpolarized source passing through an ideal polarizer results in:

$$S' = \frac{1}{2} \cdot \begin{bmatrix} s_0 \\ s_0 \cdot \cos 2\phi \\ s_0 \cdot \sin 2\phi \\ 0 \end{bmatrix} = \frac{1}{2} \cdot s_0 \cdot \begin{bmatrix} 1 \\ \cos 2\phi \\ \sin 2\phi \\ 0 \end{bmatrix} \quad (4.42)$$

where

ϕ Angle between the polarization axis of the polarizer and the horizontal direction.

Based on the Mueller matrix M , the polarization sensitivity $D(M)$ can be derived, as well as the polarization dependent loss $PDL(M)$:

$$D(M) = \frac{\sqrt{m_{01}^2 + m_{02}^2}}{m_{00}} \quad (4.43)$$

$$PDL(M) = 10 \log \frac{m_{00} + \sqrt{m_{01}^2 + m_{02}^2 + m_{03}^2}}{m_{00} - \sqrt{m_{01}^2 + m_{02}^2 + m_{03}^2}}. \quad (4.44)$$

An interesting detail is found in the m_{00} element of the Mueller matrix M . This element describes the scattering characteristic of the examined sample. This characteristic contains no polarization information and is generally referred to as the BRDF. A subsequently derived generalized Mueller BRDF can therefore be a helpful descriptor for a combined polarization and BRDF sensitive instrument. This because the amount of scattered light can be a direct indicator of surface conditions [11].

c) Modelling the Polarization Measurement

Since the adequate polarization correction for remote sensing applications in the optical domain remains extremely complex due to the combination of polarization effects, it is useful to experimentally determine the polarization sensitivity of your measurement instrument. The polarized component of the light incident on remote sensing instruments contributes to the total signal. The signal from a spectroradiometer that is polarization-sensitive will be dependent on the relative orientation of the polarization state of the radiation with respect to the spectroradiometer orientation. But in most cases one is not particularly interested in the contribution of the polarized signal to the total signal. The more important question is if the remote sensing instrument is polarization insensitive. This means that the incident polarized radiation is measured from the instrument in the same manner as the unpolarized contribution. There are many remote sensing applications available that make explicit use of the polarization (e.g. radar remote sensing [42]).

The polarization measurement setup includes the assumption of an ideal linear polarizer that is linked between the unpolarized spectral radiance source and the unknown polarization-sensitive spectroradiometer. This source is the integrating sphere that depolarizes completely the incident flux and the sphere's transmittance is independent of the incident radiation (see Figure 4.24).

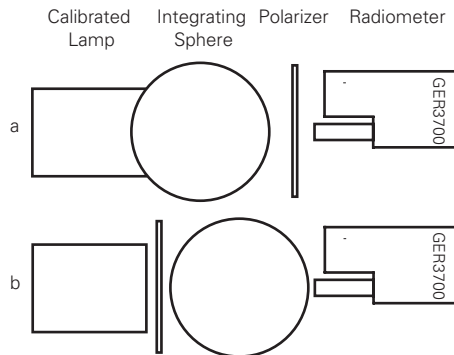


Figure 4.24: Polarization measurement setup.

Assuming an ideal linear polarizer, the transmittance is one for a spectral radiance linearly polarized in the same direction as the polarization axis of the

polarizer. The transmittance is zero for a spectral radiance polarized perpendicular to the polarization axis. Following eq. (4.42) the polarized flux is half the incident flux.

For estimating the polarization effect [50], eq. (4.41) may be solved for the first elements $\{m_{00}, m_{01}, m_{02}, m_{03}\}$ of the Mueller matrix:

$$\begin{aligned} S'_{s_0} &= \frac{1}{2} \cdot \begin{bmatrix} 1 & \cos 2\phi & \sin 2\phi & 0 \end{bmatrix} \cdot L_0 \cdot \begin{bmatrix} 1 \\ s_1 \\ s_2 \\ s_3 \end{bmatrix} \\ &= \frac{1}{2} \cdot L_0 \cdot \left[1 + s_1 \cdot \cos 2\phi + s_2 \cdot \sin 2\phi \right] \end{aligned} \quad (4.45)$$

where

L_0 Spectral radiance of the integrating sphere.

Most often it is sufficient to perform a calibration on three rotational positions of the instrument or its polarization-sensitive components. Since in the experiment the radiant source can be assumed to be of complete uniformity, it is sufficient to measure some rotation states of the polarizer (i.e. 0° , 45° , and 90°) and not to rotate either the source or the detector. Many measurements at rotations intermediate between the two orthogonal measurements have been included to test if the maximum and minimum polarization sensitivities have been sampled.

By measuring the three rotational positions of the polarizer and substituting L_λ from the measurement equation (eq. (2.2)) as well as using eq. (4.45), the following two equations can be derived to determine s_1, s_2 :

$$R = \frac{1}{2} \cdot L_0 \cdot (1 + s_1 \cdot \cos 2\phi + s_2 \cdot \sin 2\phi) \cdot R \cdot \Delta\lambda \cdot \Delta\Theta \quad (4.46)$$

$$\begin{aligned} R_{45} \cdot s_1 - R_0 \cdot s_2 &= R_0 - R_{45} \\ R_{45} \cdot s_1 + R_{90} \cdot s_2 &= R_{45} - R_{90} \end{aligned} \quad (4.47)$$

where

$$\Delta\Theta = \int_{\Delta A} \int_{\Delta\theta_f} \cos\delta \cdot dA d\theta_f \quad (4.48)$$

$\Delta\Theta$ Troughput

R Resulting output signal at rotational positions.

The experimental determination of s_3 relies on the use of a quarter wave plate. Methodically following the presented procedure for s_1, s_2 , eq. (4.45) may be

adapted as follows:

$$S' = \frac{1}{2} \cdot L_0 \cdot \left[1 + s_1 \cdot \cos 2\phi + s_3 \cdot \sin 2\phi \right]. \quad (4.49)$$

The final equation for s_3 can be given as:

$$s_3 = \frac{R_0 - R_{45}}{R_0 + R_{45}}. \quad (4.50)$$

After the successful determination of the Stokes values, the Mueller matrix elements m_i can be defined. Again, the Stokes vector following the polarizer is taken from eq. (4.42). The following Mueller matrix for the spectroradiometer is used:

$$m = \begin{bmatrix} 1 & m_{01} & m_{02} & m_{03} \\ \cdots & \cdots & \cdots & \cdots \\ \cdots & \cdots & \cdots & \cdots \\ \cdots & \cdots & \cdots & \cdots \end{bmatrix}, \quad (4.51)$$

where the output signal is with reference to eq. (4.46):

$$R = \frac{1}{2} \cdot L_0 \cdot (1 + m_{01} \cdot \cos 2\phi + m_{02} \cdot \sin 2\phi) \cdot R \cdot \Delta\lambda \cdot \Delta\Theta, \quad (4.52)$$

and therefore

$$\frac{R_0}{R_{45}} = \frac{1 + m_{01}}{1 + m_{02}} \quad (4.53)$$

$$\frac{R_{45}}{R_{90}} = \frac{1 + m_{02}}{1 - m_{01}}. \quad (4.54)$$

The last element, m_{03} is derived according to eqs. (4.49) and (4.50):

$$m_{03} = \frac{R_{45} - R_0}{R_0 + R_{45}}. \quad (4.55)$$

The final estimation of the polarization effect present in spectral measurements is given in the following formula:

$$P_{Corr} = \frac{1 + s_1^S \cdot m_{01} + s_2^S \cdot m_{02} + s_3^S \cdot m_{03}}{1 + s_1 \cdot m_{01} + s_2 \cdot m_{02} + s_3 \cdot m_{03}} \quad (4.56)$$

where

P_{Corr}	Wavelength dependent polarization correction
s_i^s	Stokes vector of the standard
s_i	Stokes vector of the polarizer
m_{ij}	Mueller matrix of the radiometer.

d) Polarization Measurement

In the optimal case, three different measurement setups are required to fully determine the polarization sensitivity of the radiometer. The instruments needed for the measurements are a stabilized radiance (irradiance) source, an integrating sphere, a polarizer, a quarter wave plate and finally the radiometer.

In general the transmittance of the polarizer is measured using the integrating sphere. The measurements are performed using a rotational interval of 5° and are plotted against its transmittance. Due to the absence of a quarter wave plate, the values for s_3 and m_{03} respectively have been substituted by the values for an ideal polarizer and radiometer.

The experimental measurement setup used (see Figure 4.24) places the polarizer between the light source and the integrating sphere and is used to determine the Stokes vector of the polarizer (s_1, s_2). Using the polarizer after the integrating sphere, the setup is suited to determine the elements (m_{01}, m_{02}) of the Mueller matrix of the radiometer.

In addition, if using a quarter wave plate, the determination of all the elements of the Mueller matrix is possible (m_{ij}).

e) Results

The first measurement of the apparent transmittance of the polarizer is to verify the proper behavior of the measurement setup. The plotted wavelength in Figure 4.25 is at 649.4 nm and demonstrates the expected orthogonal symmetry of the polarization effect. The fitted function $f(x) = k_0 + k_1 \cdot \sin(xk_2 + k_3)$ underlines the orthogonal symmetry of the polarizer—except for the 5° measurement, the residuals are well below 0.5%. These measurements are performed using measurement setup a, where the uniform light source is placed before the polarizer.

Using these measurements the two important parameters $D(M)$ (polarization sensitivity, eq. (4.43)) and $PDL(M)$ (polarization dependent loss, eq. (4.44)) are plotted in the wavelength range between 400 and 900 nm. The transmittance of the polarizer is nearly 100% above 900nm. For this reason these measurements above this wavelength are not included here.

Figure 4.26 plots the polarization sensitivity $D(M)$, scaled on the left axis between 1.5 and 6.5% in the observed region. The polarization dependent loss (scaled on the right axis) does not exceed 0.5% for this measurement setup. $D(M)$ shows that *the radiometer is polarization sensitive* and that under ‘optimal’ circumstances the polarization dependent loss is less than 0.4%. In real world remote sensing applications, $PDL(M)$ can not be quantified, since the atmospheric effects produce randomly distributed polarization effects. The correction

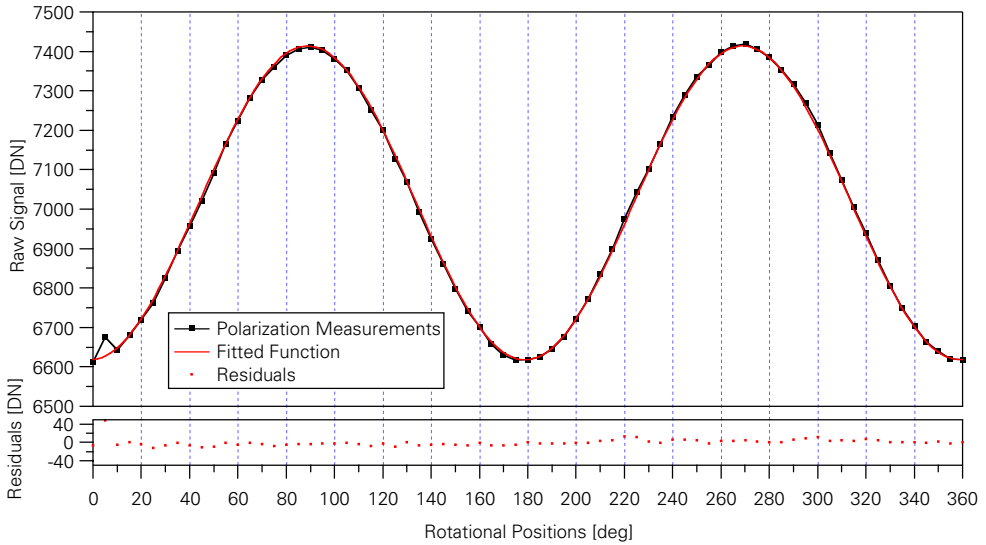


Figure 4.25: Apparent transmittance of a polarizer at 649.4 nm.

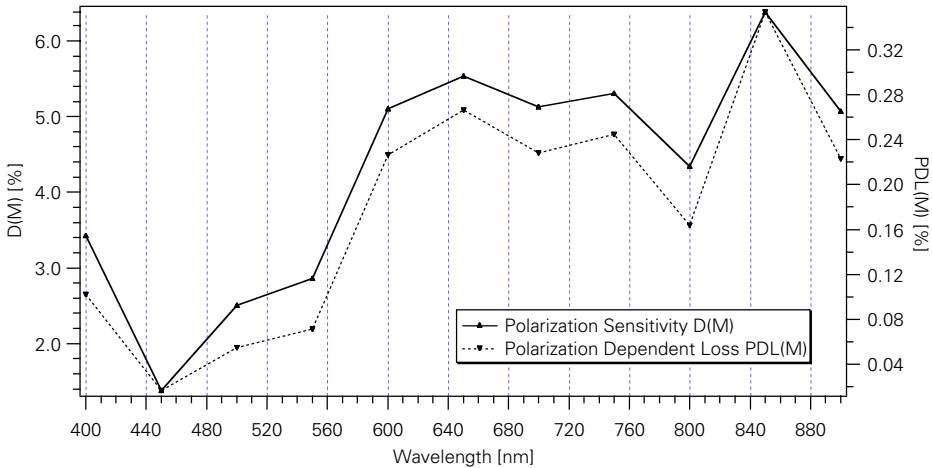


Figure 4.26: Polarization sensitivity and polarization dependent loss.

factor ($PDL(M)$) is therefore not applied to every measurement, but included as a systematic error.

The estimated polarization sensitivity is $\leq 2\%$. The resulting polarization dependent loss of the spectroradiometric signal is $< 0.4\%$. This difference results from the difficult measurement setup, and the problems associated with the proper estimation of polarization effects present at a remote sensing instrument.

4.6.10 Size-of-Source Effect

a) Introduction

The size-of-source effect is caused by optical aberrations, diffractions, and scattering in the fore-optics of the spectroradiometer if the measured source is much smaller in size as the imaged area by the spectroradiometer. The effect does not occur in spectral irradiance measurements where it is limited to an error $\ll 0.5\%$ [50].

The sources used for this characterization are all completely filling the total FOV of the spectroradiometer. The integrating sphere calibration standard is directly coupled to the fore-optics of the radiometer. The polarizer is larger than the FOV and the Spectralon diffuse reflectance standard in a distance up to a few meters is filling the aperture of the spectroradiometer. Using the laser as a source, the beam diameter is adjusted to the diameter of the spectroradiometer. This involves a number of collimating lenses aligned to match the beam to the optics.

b) Conclusion

The size-of-source effect is not measured here. The errors from this effect are normally in the interval $(0.005-0.5)\%$ and this error is mostly added in field measurements. In those situations where the source imaged is much smaller than the FOV of the spectroradiometer or adjacent objects significantly contribute to the at-sensor-radiance through multiple scattering effects.

4.6.11 Temperature

a) Introduction

The influence of temperature effects on the different parts of a spectroradiometric measurement system must not be overlooked. Although a detector is said to be inherently linear, the loaded detector circuit is not. In addition some elements of the radiometer can be temperature dependent such as uncooled PbS detectors operated in a hot summer environment. It might not be an extreme challenge to calibrate the instrument in the laboratory under stable environmental conditions. But the traceability must be questioned if these data are compared to field measurements. The best solution to this problem would be to operate the instrument always in a controlled environment and trace back the temperature changes to the laboratory values using an appropriate model.

The special requirements for a field portable spectroradiometer often do not allow the integration of a cooling system because of space and power consumption constraints. Another approach would be to measure the relative change in calibration factors as a function of temperature and compensate for these changes in postprocessing steps.

b) Theory

The discussion of linearity associated with spectroradiometric measurements can be found in Chapt. 4.6.5. The linearity of Si detectors is usually excellent in the 10^{-8} to 10^{-3} W range. The temperature discussion in this chapter therefore

focuses on the lead sulfide detectors only. PbS detectors can be found in many spectroradiometric applications operating in the wavelength region between 850 and 3800 nm. It is one of the most sensitive uncooled detector types being used in the region between 1300 and 3000 nm. PbS detectors are available optimized to operate in three different temperature ranges. The one of interest in this case is the ATO (ambient temperature operation) type [45]. Most detectors undergo a change of the detectivity D^* with a change of temperature. D^* is a relative sensitivity parameter which is used to compare different detector types. D^* is the SNR at a particular frequency and in a 1 Hz bandwidth when 1 Watt of radiant power is incident on a 1 cm^2 active detector area. The higher D^* values, the better the detector is.

Virtually no literature is available on the quantitative thermal stability of these detectors.

c) Modeling the Temperature Dependency

Due to lack of information on athermalization efforts inside the spectroradiometer, it is assumed that the thermal effects within the housing of the radiometer are homogenous. Additionally, it is assumed that the changes of defocusing are negligible compared to the effects on changing D^* .

The established temperature model assumes an exponential change of the input signal with any change of environment temperature:

$$R_{DN, T_{PbS}} = k_0 + k_1 \cdot \exp(-k_2 \cdot k_3) \quad (4.57)$$

where

$R_{DN, T_{PbS}}$ Temperature dependent detector signal
 k_n Fit parameters, where $k_3 = T_{PbS}$, the corresponding detector (PbS1) temperature reading.

d) Temperature Dependency Measurement

In this specific experiment it is the goal to delineate the response of the spectrometer to the most usual field operating temperatures. The expected interval in this experiment ranges from approximately 22° to 55° Celsius. The starting temperature might be high for winter environments, but the instrument heats itself up rapidly after a short time of operation, even if it is not exposed to the sun or any other thermal radiation.

In this experiment we have been using an integrating sphere calibration source. The assumption is that the source has a verified linear performance over all decades of radiant power. The second assumption is that the spectral linearity is constant over the measurement range. Both assumptions are likely to be true since the integrating sphere is controlled by a photopic detector, and the lamp current is highly constant over time. The next assumption is that the heat dissipation from the sphere to the radiometer is considerably low. The temperature stabilized environment of the calibration chamber is used as a reference (22° C). The measurement equipment is stored 24 h prior to the measurements in the

chamber so that all instruments start at the same temperature.

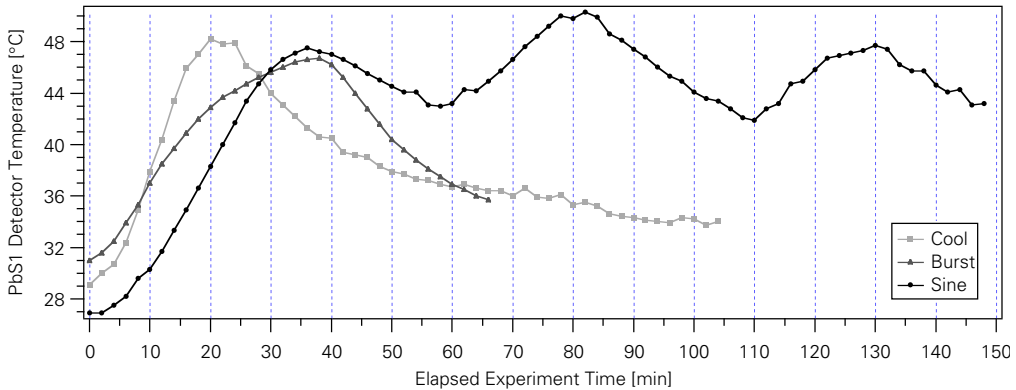


Figure 4.27: Radiometer temperature readings for three experiments: heat once, cool down passive (cool); heat once, cool down active (burst); and heat and cool three times (sine).

The relatively high starting temperature for all three experiments is a result of the warm-up phase of the spectroradiometer. Prior to any measurement, the instrument is switched on at least 15 min. before the first measurement. The three experiments carried out resulted in a total of 162 measurements (see Figure 4.27).

The measurements have been performed for all channels of the spectroradiometer, but only the PbS1 and PbS2 detectors are of real interest. The temperature fit for the PbS1 detector is plotted against the signal change for three channels. Near channel 1 of the PbS1 detector (instrument channel 513, at 987.79 nm) the temperature measurement is performed using a PT detector. The total signal change detected here ranges from 1'500 DN at 27° C to 650 DN at 50° C. Equivalent temperature sensitivities are detected for the channel 64 (1515.56 nm) and channel 128 (1888.32 nm) of the PbS1 detector (see Figure 4.28).

The measurement results correspond with the substantial decrease of D^* after the maximum around 200° K and reach the same low D^* values for 75° K and 300° K (i.e. 27° C). No values could be found for temperatures exceeding 300° K. The plot of all model parameters (in Figure 4.29) displays again the amplified upper part of the PbS1 detector. The amplification of the signal is apparent between detector element 63 and 64.

e) Conclusion

Absolute radiance measurements in the PbS1 and PbS2 detector range must be calibrated for temperature drifts. The temperature related effect affects all wavelengths between 987 and 2500 nm. As a consequence, for reflectance measurements it is important to minimize the time between reference and target measurement. Otherwise the temperature induced effects will dominate possible changes, rather than atmospheric influences.

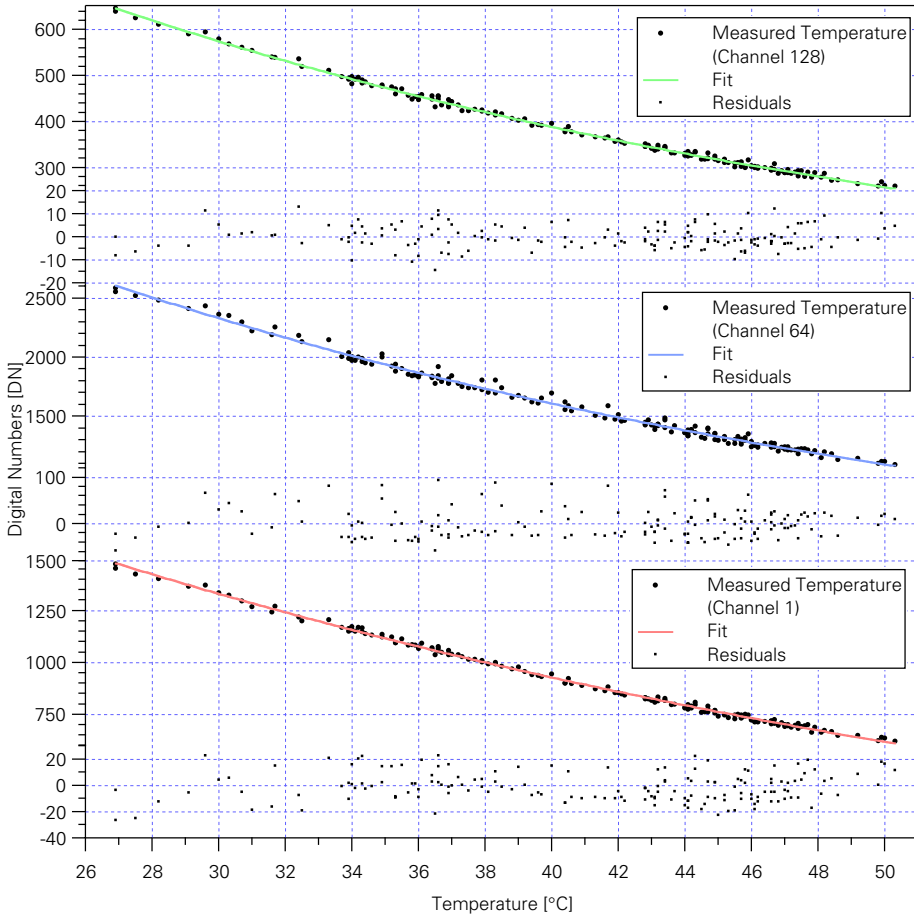


Figure 4.28: Temperature fit for three selected PbS1 detector channels.

The temperature uncertainty introduced by the different detectors is calculated using the temperature fit models for each spectroradiometer channel. Since the Si detector is not temperature sensitive to the same extent as the PbS detectors, the resulting Si temperature sensitivity is $< 0.1\%$. The PbS detectors in the temperature interval of laboratory measurements expose an uncertainty of $< 1\%$.

A major upgrade of the system might include the temperature readouts for at least the two border elements of each PbS detector. An appropriate model could, within certain limits, compensate for the temperature drift. The temperature stabilized housing, or even a cooling of the detectors would significantly improve the absolute radiance measurement capabilities of the spectroradiometer.

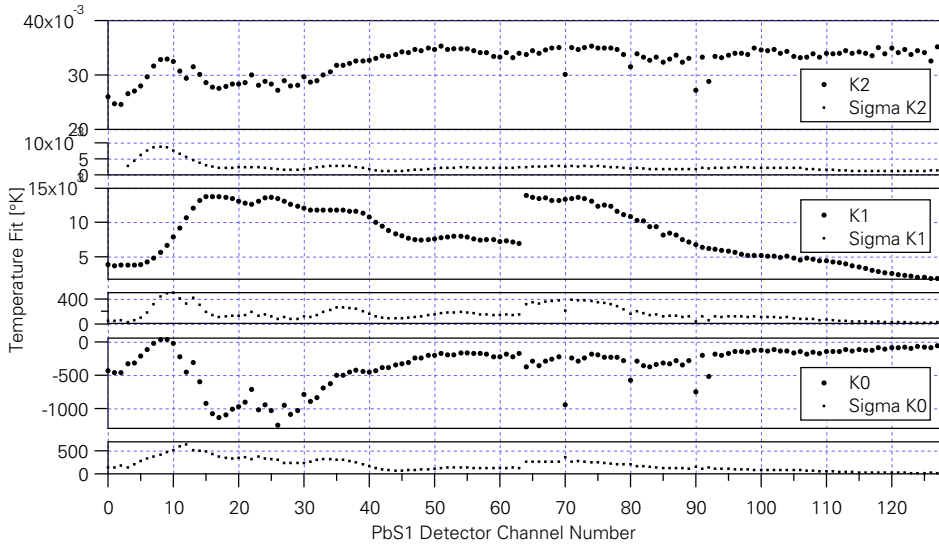


Figure 4.29: Offset values for temperature model in the PbS1 detector.

Chapter 5:

Field Reflectance Spectroradiometry

5.1 Introduction

Two types of reflectances are most commonly referred to: Radiation that is reflected specularly or radiation uniformly reflected in all directions of the hemisphere. The first case represents an ideal reflecting surface, and the second an ideal Lambertian surface. Both cases are ideal and are never found in practice, so any reflectance measurement is a combination of both types [106].

Reflectance spectroradiometry is the quantitative measurement of reflectance. In most cases the ambient solar illumination is used for comparison measurements between the remote sensing instrument and the ground spectroradiometer. In some situations it is nevertheless more desirable to have a fixed illumination and viewing geometry. In such cases an artificial illumination in a laboratory is used. This technique is most often used to compile spectral libraries of special materials of interest [15][39].

Reflectance spectra measured under solar illumination are strongly modified by the absorbing molecules in the atmosphere [36]. By using division of the target signal by the reference, all multiplicative parameters are ratioed out. Nevertheless, diffuse illumination, scattered light of the instrument, the measurement equipment and the persons measuring may significantly influence the total measured signal [22].

Reflectance measurements of homogenous ground targets, at the scale of imaging sensors, can be used to model at-sensor-radiances for vicarious calibration experiments. In addition they can be used to compile spectral libraries of known endmembers for spectral unmixing applications, and reference objects for further comparison.

5.2 Measurement of Reflectance

The measurement of reflectance is based on the process where a fraction of the radiant flux incident on a surface is returned into the same hemisphere whose

base is the surface and which contains the incident radiation [66]. The spectral reflectance can subsequently be defined as:

$$\rho(\lambda) = \frac{\Phi_{\lambda r}}{\Phi_{\lambda i}} \quad (5.1)$$

where

- $\rho(\lambda)$ Spectral reflectance factor
- $\Phi_{\lambda r}$ Reflected spectral radiant flux
- $\Phi_{\lambda i}$ Incident spectral radiant flux.

This spectral reflectance factor is only valid if the surface corresponds to a perfect diffuse (or Lambertian) reflector. But since the Lambertian assumption is only an approximation used in reflectance measurements, another factor must be introduced to account for the possible geometries if the reflector is not perfectly lambertian. The fundamental *geometric* descriptor of reflectance is the bidirectional reflectance distribution function (BRDF). The associated nomenclature for reflectance and reflectance factors is discussed in detail in Nicodemus et al. [59]. The reflectance factor is therefore a simplification of the expression for the hemispherical–directional reflectance factor [29].

Field measurements of reflectance are mostly relative measurements and require an artifact standard. This standard must be as compliant as possible to the lambertian assumption, i.e. the BRDF component must be close to 1. Additionally the standard must be insensitive to contamination, aging, weather and other physical influences from the environment.

The most critical parameter in field reflectance measurements are the—for the human observer mostly invisible, irradiance changes due to atmospheric effects. Most of these changes affect the major water vapor absorption bands but other bands might be also affected. Since most reflectance measurements continue to be single FOV measurements [56], the time between the reference and the target measurement must be minimized in order to minimize possible atmospherically induced changes. This optimization is also required because the illumination characteristics must be the same for the reference and target measurements. Any change in position of the observer or illumination geometry between a reference and a target scan introduces a BRDF related change in the signal. In addition, when using any field reflectance standard, the correction for the non–lambertian behavior of the standard must be taken into account.

By incorporating any field standard $\rho_{\lambda s}$, the reference measurement can be modified based on eq. (5.1) as follows:

$$\rho(\lambda)_{corr} = \Phi_{\lambda r, t_1} \cdot \frac{\rho_{\lambda s}}{\Phi_{\lambda i, t_0}} \quad (5.2)$$

where

- $\rho(\lambda)_{corr}$ Spectral reflectance corrected for non–lambertian field reference
- $\rho_{\lambda s}$ Spectral reflectance factor of the field standard.

Since in most cases $t_0 - t_1 \neq 0$ with $\Delta t < 15 \text{ min}$, ρ_{λ_s} must be applied to Φ_{λ_i} before multiplying it with the reflected radiance. The uncertainty associated with $t_0 - t_1 \rightarrow \infty$ is discussed in chapter 6.4.1.

A quantification of the atmospheric stability in selected wavelengths can be given using sunphotometer measurements. The irradiance changes associated with varying optical transmittance is plotted against measurement time in Figure 5.1. Any vertical dashed line corresponds to a 6 min. interval. Obviously, an uncertainty of 2% is very likely and is therefore included in the final uncertainty budget.

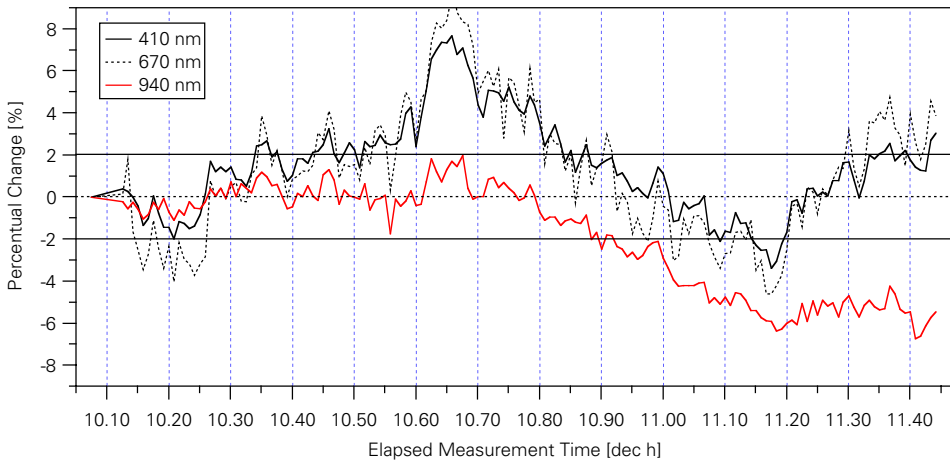


Figure 5.1: Percentual change of atmospheric transmittance over time in three selected wavelengths (410 nm, 670 nm, and 940 nm).

The overall uncertainty arising from the general assumption using a perfect lambertian reflector can be quantified with a RTC. Assuming $t_0 - t_1 = 0$ (e.g. reference and target measurements performed at the same time), the RTC helps to model both a constant surface albedo of 1 over the whole spectral range covered, and the Spectralon reflectance standard as ground albedo using the NIST calibrated reflectance values.

The additional uncertainty introduced by the lambertian assumption is between 1–2% in the VIS/NIR range of the electromagnetic spectrum, whereas it increases around 2000 nm due to an absorption band present in the PTFE material up to 6%. Figure 5.2 shows the uncertainty difference between eqs. (5.1) and (5.2).

5.3 Field Standards

Field standards are reference materials that should exhibit a highly lambertian reflectance over the whole spectral range of interest. In addition, the reflectance

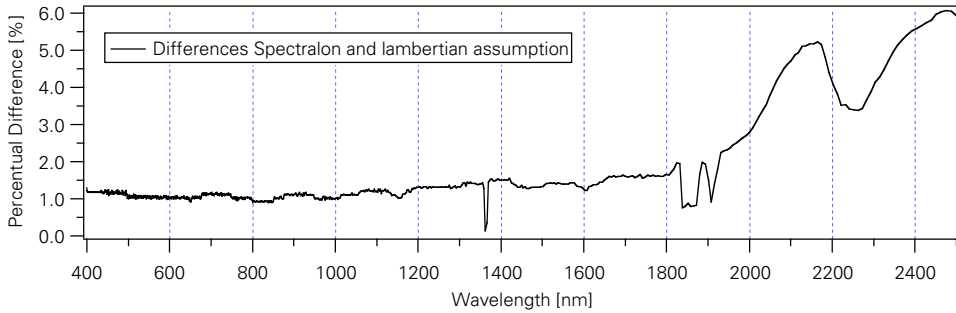


Figure 5.2: Differences of a perfect lambertian assumption (100% reflector) and the Spectralon reference standard.

of the material should be insensitive to BRDF effects and should reflect at least more than 80% of the incoming radiation. Since contamination of the standards material is often a problem, the spectral and spatial characteristics should not degrade over time and—if used frequently in the field—should be able to be washed or rinsed to remove contamination or particles such as mud, sand or others.

5.3.1 Spectralon Reflectance Standard

The reflectance calibration of spectroradiometric measurements in the field requires a Spectralon panel as a reference standard. Spectralon® is a registered trademark of Labsphere, Inc. and a patented reflectance material (US Patent No. 4'912'720). Spectralon is made from PTFE (polytetrafluoroethylene) powder and is sintered without the use of binders. This makes the material thermally stable up to 350° C and it is chemically inert to most bases. The surface and the immediate subsurface structure of Spectralon exhibits highly lambertian behavior apparently arising from the porous structure of the thermoplastics resin [107]. This structure causes both reflectance and transmittance, but not absorbance, of light. For applications requiring a totally opaque reflectance, $BaSO_4$ (barium sulfate) can be added to Spectralon. But the spectral properties of Spectralon exceed those of most paints which show strong absorbances in the UV due to absorbances by TiO_2 or similar pigments. Such black pigments added to the resin—even at very low concentrations—change the porous structure of Spectralon and lead to a reduction of multiple scattered reflections. These optical properties result in a less than lambertian reflectance behavior [108].

The spectral signature of Spectralon is relatively flat in the region of 0.25 to 2.5 μm . The reflectance variance there is < 5%; between 0.36 and 0.74 μm even < 0.05%. The hydrophobic nature of Spectralon also leads to the non-existence of water overtone bands in the NIR, which are present in $BaSO_4$ based materials [40].

Spectralon is a tradename and must be considered as a descriptor for con-

trolled processes using PTFE to construct a reflectance standard. The generalized fabrication process for the PTFE powder was first published by Weidner et al. [119] of NIST. The terms ‘Halon’, ‘Sintered Halon’, ‘PTFE’, and ‘Spectralon’ are often used interchangeably to describe a reflectance standard. PTFE standards are widely accepted and are used as standards for inter-laboratory calibration for diffuse reflectance measurements [120].

Two different measures of a material’s ability to scatter light are identified here. On the one hand, the BRDF gives a good estimate of the lambertian behavior of Spectralon reflectance material [32]. Field reference-reflectance panels can be calibrated using a goniometer and a standard that is traceable to NIST [118]. For the MISR (Multi-Angle Imaging SpectroRadiometer) calibration, BRDF experiments have been carried out using degraded and non-degraded Spectralon. The deviation from the mean of the measurements was typically in the order of 0.5%; the Spectralon samples were considered the same [7]. On the other hand, the total hemispherical reflectance as a factor of the angle of the incident radiation can be measured.

In general polarization effects decrease with increasing illumination angle. With Spectralon usually the degree of depolarization does not differ to much except for the 500 nm wavelength region [40].

The field calibration reported here is performed using a Spectralon SRT-99-100 diffuse reflectance target. The target ships in an anodized black aluminium frame and has a reflective area of 25.4 by 25.4 cm.

Description	Value
Spectral Range	0.2–2.5 μm
Reflectance	98 – 99%
Thermal Stability	up to 350° C (decomposes at > 400° C)
Vacuum Stability	Minimal outgassing of entrained air
Laser Damage Threshold	> 8.0 J/m ²
General Use	UV – VIS – NIR
Density	1.25–1.5 g/cm ³
Water Permeability	< 0.001% (Hydrophobic)
Hardness	20–30 Shore D
Coefficient of Linear Expansion	5.5–6.5x10 ⁻⁴ in/°C
Flammability	Non-flammable, incompatible with non-polar solvents

Table 5.1: Properties of Spectralon reflectance material [54].

Figure 5.3 lists the 8° hemispherical spectral reflectance factor for the Spectralon SRT-99-100 reflectance panel. The data have been calibrated by the NIST using

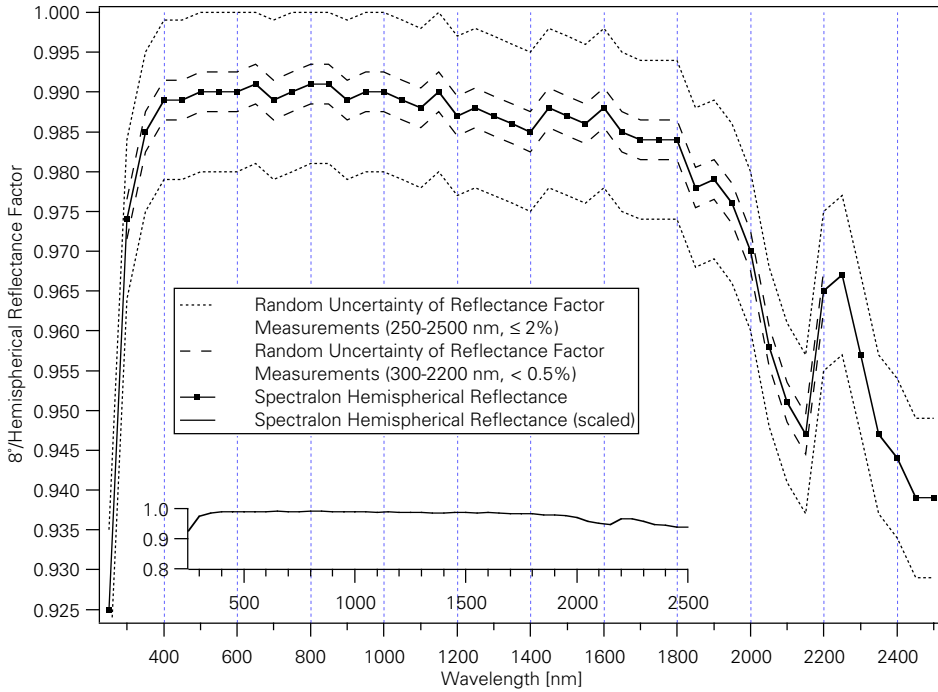


Figure 5.3: NIST calibrated Spectralon 8° hemispherical reflectance factor [53].

a NIST reference reflectometer. The random uncertainty of reflectance factor measurements is estimated to be less than 0.005 over the spectral range from 300–2200 nm, and less than or equal to 0.02 over the spectral range from 250–2500 nm [53].

5.3.2 Other Field Standards

A huge selection of materials exist that are being used as a reflectance standard in the field. Amongst them, Spectralon, sintered Halon, fused silica (SiO_3), alumina (Al_2O_3), and sintered silicon nitride (Si_3N_4) are the most popular [40].

Since the discontinuation of the production of Halon, type G–80, one of the most widely used material, the search for an equivalent alternative standard material has started. A possible successor has been identified and tested under the name, pressed Aglofon F6. The physical properties of this material are quite similar, so that most likely Aglofon will replace Halon [109].

There are also individual diffuse reflectance standards available that have reflectance factors between 2% and 99%. But with decreasing reflectivity (or increasing amounts of black or other dark pigments) the diffuse component of the panel is reduced and exhibits a stronger BRDF component. It is therefore not

advisable to use grey reflectance standards as field calibration standards because of the associated BRDF component. But to better represent the quantity to be measured in the field, a 50% reflecting target would be closer to the mean reflectance to be expected in a field experiment.

The measured field reflectances during an average summer day in Switzerland display this headroom between the maximum reflectance of typical objects and the Spectralon panel (see Figure 5.4). The calibration procedure, when using an integrating sphere calibration standard, must therefore take into account the

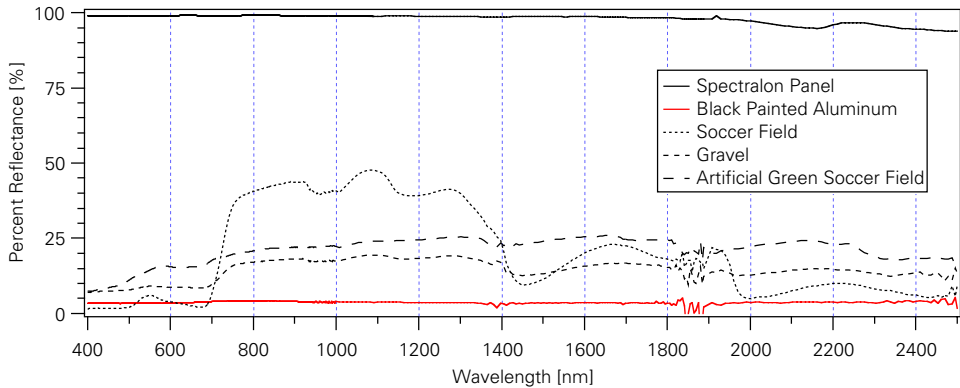


Figure 5.4: Field reflectances of different objects under solar illumination in comparison with Spectralon reflectance.

total dynamic range of reflectivity present in field measurements (see also the discussion associated with Figure 4.19).

5.4 Measurement Plan

An updated measurement plan, focusing on field reflectance measurements, is presented in Table 5.2. The assumptions made are that the characterization process of the spectroradiometer is successfully carried out, and a well characterized instrument is available.

One of the most critical points in the plan for field reflectance measurements is the selection of the measurement design. This simply refers to means how they are carried out, and how often they are repeated to achieve the best representation of the quantity measured.

5.5 Reflectance Measurement

Field reflectance measurements are performed with the spectroradiometer looking from a distance of 2 m in nadir direction on the ground. Since in most cases

Major Plan	Detailed Plan	Action
Detailed description of the quantity to be measured including the accuracy desired	Quantity to be measured Wavelengths to be measured Measurement accuracy desired Geometry of quantity Relative spectral distribution Approximate magnitude Stability Polarization	Spectral Reflectance 400–2500 nm ≤ 10% Nadir looking measurements of reflectance 400–2500 nm 0 – 100% ≤ 5% ≤ 2%
Identification of potential error sources and their magnitude		see chapt. 4.6
Selection of the radiance standard	Source standard	Sun, solar reflected radiance
Selection of the spectroradiometer	Selecting the fore-optics Selecting the system setup	2° FOV chapt. 3.3
Characterize the spectroradiometer for all potential errors		see chapt. 4.6
Select and characterize the measurement setup	Selection Characterization	Type 3 (see Figure 4.4) Type 3 (see Figure 4.4)
Select the measurement design	Define sampling strategy Sampling scheme Sampling size	see chapt. 5.4 Stratified random sampling 30–40
Acquire the data and calculate the quantity desired	Carrying out the measurements	see chapt. 5.6
Prepare the uncertainty report	All sources of uncertainty Error Type A or Type B Degrees of freedom Combined uncertainty Expanded uncertainty	chapt. 6.4.1.a chapt. 6.4.1.b chapt. 6.4.1.c chapt. 6.4.1.d chapt. 6.4.1.e

Table 5.2: Measurement Plan for the GER3700 in Field Measurements

single FOV instruments will be used, two subsequent measurements must be taken. The first is the reference measurement of the field standard and subsequently the target is measured. The time between the reference and target mea-

measurements is critical in terms of the short-term changes of the solar irradiation and the change of the illumination and observer geometry.

5.5.1 Sampling Strategy

Assessing the homogeneity of any object in the field requires many spectroradiometric measurements. In most cases when measuring in the field it is useful to have a measurement plan at hand that defines the sampling strategy according to the measurement type selected. In addition, it is useful to compile a field report sheet for any spectroradiometric measurement and to note as much as possible additional attributes available for each individual data take (e.g. cloud coverage, wind, temperature, (soil) moisture, (GPS) coordinates, adjacent objects, surface roughness, etc.).

The major goal of the implementation is to minimize measurement errors and the measurement uncertainty of the objects to be assessed. The sampling strategy is composed of two major factors defining the representativeness of the samples: the sampling scheme and the sample size.

a) Sampling Scheme

Sampling schemes can be subdivided into a number of categories [2]:

- simple random sampling
- systematic sampling
- stratified random sampling
- hierarchical sampling
- cluster sampling, and
- stratified systematic unaligned sampling

A good discussion on the appropriate selection of sampling schemes is found for general applications in Haggett et al. [41] and for remote sensing applications in Congalton [18]. For this calibration, the field measurements are performed using stratified random sampling.

b) Sample Size

Using the standard field setup of the spectroradiometer, the area covered by one measurement is according to eq. (4.35) (chapter 4.6.8):

$$A_t \cong 36.7 \text{ cm}^2 \quad (5.3)$$

where

$$\begin{aligned} h &= 2 \text{ m} \\ \theta_f &= 1.96^\circ. \end{aligned}$$

This small area covered can be disadvantageous if assessing very rough surfaces such as meadows and grass. But the absolute size of the sample size is more important than the relative proportion of the individual measurements on the total field size. In any case, statistical representative numbers of sample sizes are between 30–40 measurements [2][41]; this size is far too large for field measurements related to vicarious calibration, where measurements can only be taken during the

actual overflight. But assessing in-field variations of crops or other vegetation stands, this sample size is adequate. The spectrum plotted in Figure 5.5 has a sample size of $n = 43$ covering 'only' 0.11% of the total $A = 144m^2$ area. Every second measurement was a reference measurement to minimize the uncertainty of atmospheric changes (see eq. (5.2)).

5.6 Performing the Measurement

Whilst performing a vicarious calibration during an overflight of a remote sensing sensor, the time between reference and target measurement must be kept as short as possible. The time interval between the actual overflight and the field measurements must also be minimized. But when assessing the homogeneity of a crop, the in-field variation can only be assessed by averaging many individual sampling points. In any case, the maximum time between any new reference measurement should not exceed 15 min. A critical number of degrees of freedom is added to spectroscopic measurements when measuring with the sun as illumination source. Not only the geometrical position of the sun is dependent on time but also the atmospheric transmission. Additionally, natural surfaces are also subject to changes with the time of day. The final corrected reflectance measurement is usually scaled between 0 and 100%. In many cases where the specific application of measuring the signal in the deep atmospheric absorption bands is not of special interest, these values are usually removed. The reflectance spectrum plotted in Figure 5.5 shows the spectrum of an constructed blue place on the campus of the University of Zürich, made of the same material as the short distance training areas of an athletic stadium. The solid line plots the averaged signal, whereas the dots indicate individual measurement points. Each measurement is corrected for the near-perfect lambertian assumption of the Spectralon reference panel.

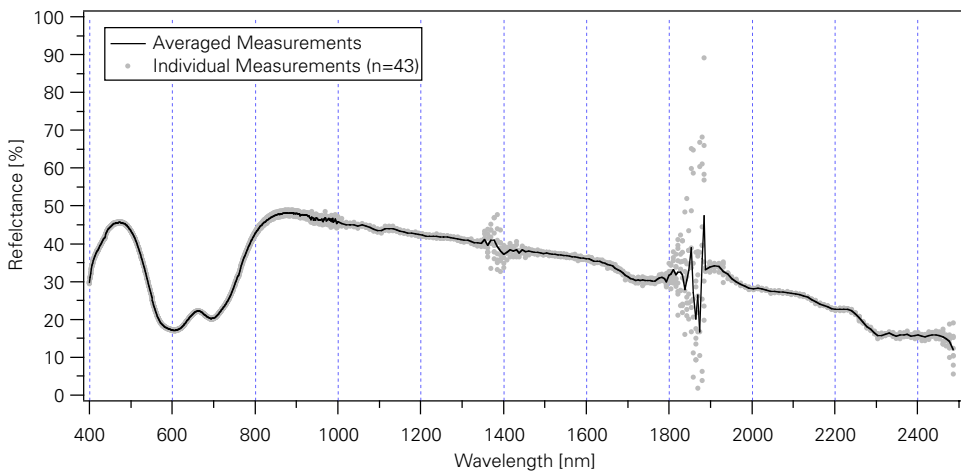


Figure 5.5: Calibrated absolute reflectance spectrum of an artificial blue coating.

Chapter 6:

Calibration Uncertainty Estimation

6.1 Uncertainty in Spectroradiometric Measurements

It has been widely accepted that spectroradiometric measurements must be accompanied by a high quality statement of uncertainty to improve their usefulness and reusability for further analysis. The major standardization effort is undertaken by CIPM (Comité International des Poids et Mesures), the authority in metrology to establish a standard in the expression of uncertainty in measurements. The recommendation was approved in 1986 [14].

The goal of this chapter is to promote full information on how uncertainty statements are arrived at, and to provide a basis for the international comparison of measurement results.

6.1.1 Introduction

Similar to the introduction of the International System of Units (SI), it is helpful to have a measure for uncertainty that also expresses the significance of a measurement. An ideal method for this expression would be one that is applicable to all kinds of measurements (i.e. that is *universal*), and that is directly derivable from contributing components (i.e. *internally consistent*). The method must also enable the direct use of the uncertainty expression to evaluate another measurement (i.e. it should be *transferable*) [43].

There exist two major estimation categories for the numerical values of a measurement result:

- **Type A Evaluation of standard uncertainty**

This method of uncertainty evaluation utilizes statistical analysis of a series of observations. Variations are due to the effects of uncontrolled variables. The magnitude of these effects is usually small and successive measurements form a random sequence. Type A errors are estimated using standard statistical methods. If the distribution of the measurements is known (e.g. Gaussian or Poisson), then one uses the formalism appropriate to the distribution. It is usual to assume Gaussian distribution and then to apply Gaussian statis-

tical concepts and terminology to express the uncertainty of radiometric measurements.

- **Type B Evaluation of standard uncertainty**

This method of uncertainty evaluation uses means other than the statistical analysis of a series of observations. Type B uncertainty is not detectable as variation since it does not change for successive measurements with a given measurement method. It arises because of differences between the ideal behavior embodied in the fundamental laws of physics and real behavior detected in an experimental simulation of the ideal. Type B uncertainties are either scientific judgements of the magnitude of the difference between the real and the ideal, or they are the result of auxiliary measurements. If an auxiliary measurement can be devised to measure a systematic error (or Type B error), then it need no longer be considered an error—it can be used as a correction factor. If such a correction is applied then the uncertainty is reduced to the uncertainty associated with the auxiliary experiment. Unfortunately the scientific judgement for a type B error is often subjective. For Type B errors, therefore neither a confidence interval nor a standard deviation level is objectively quantifiable.

The sum of all type A and B uncertainties contribute to the final signal. Because type A errors are truly random, they are uncorrelated. Type B uncertainties may either be uncorrelated or correlated. The correlated type B uncertainties must be arithmetically summed in a way that accounts for their correlation. Therefore it is usually desirable to partition type B uncertainties so that they are uncorrelated [123].

Type A evaluation is based on any valid statistical method for treating data, while Type B evaluation is based on scientific judgement using all relevant data available, including previous measurement data, experience, general knowledge, specifications, data provided in calibration reports, and uncertainties assigned to reference data taken from handbooks or literature [113].

The combined standard uncertainty of a measurement result (u_c) represents the standard deviation of the result. The combination of all individual standard uncertainties (Type A and B) is called the law of propagation of uncertainty (also known as ‘root–sum–squares’, or ‘RSS’). u_c can be expressed as the standard uncertainty of the measurement result y :

$$u_c^2(y) = \sum_{i=1}^N \left(\frac{\partial f}{\partial x_i} \right)^2 \cdot u^2(x_i) + 2 \sum_{i=1}^{N-1} \sum_{j=i+1}^N \frac{\partial f}{\partial x_i} \frac{\partial f}{\partial x_j} \cdot u(x_i, x_j) \quad (6.1)$$

where

$u_c^2(y)$ Estimated variance

$\partial f / \partial x_i$ Partial derivatives (‘sensitivity coefficients’).

An additional expression to the standard uncertainty u_c is the expanded uncertainty U , and is defined as:

$$U = k \cdot u_c(y) \quad (6.2)$$

with

$$y - U \leq Y \leq y + U \quad (6.3)$$

so that

$$Y = y \pm U \quad (6.4)$$

where

k	Coverage factor
y	Measurement result
Y	Measurand.

U therefore defines an interval about the measurement result within which the value of Y is confidently believed to lie. The coverage factor is in general chosen on the basis of the desired level of confidence. Typically it is in the range of 2 (normal distribution, level of confidence approx. 95%) to 3 (level of confidence greater than 99%) [113]. In spectroradiometry it is most usual to have a coverage factor of 2 (Exceptions are the measurements of physical constants and international comparisons of SI units, which do not apply for this calibration).

6.1.2 Determination of Uncertainty in Spectroradiometry

Many of the standard uncertainties can not be measured using statistical approaches. This is because of the non–statistical behavior of some of the quantities measured, such as the wavelength instability or instabilities associated with a standard. For these non–statistical behaviors, a rectangular probability distribution is assumed. Finally, upper and lower limits for the measurements falling into the category of nonstatistical instabilities must be established, making the resulting uncertainty [43]:

$$u_c(y) = (y_{max} - y_{min}) / (2\sqrt{3}) \quad (6.5)$$

where

$y_{max}; y_{min}$ Upper and lower limits of measurement.

If all standard uncertainties are obtained through performing measurements, and these all have a normal distribution, the coverage probability for the reported uncertainty can be provided. The estimate of the effective degrees of freedom is derived using the Welch–Satterthwaite formula [113]:

$$v_{eff} = \frac{u_c^4(y)}{\frac{1}{v_i} \cdot \left(\sum_{i=1}^n u_i^4(y) \right)} \quad (6.6)$$

where

$u_i(y)$ i 'th standard uncertainty where all u_i are mutually statistically independent and determined from normally distributed quantities

ν_i the degree of freedom of $u_i(y)$.

The degrees of freedom from Type A evaluation is in this spectroradiometric calibration:

$$\nu_i = n - m \quad (6.7)$$

where

ν_i Degrees of freedom from $u_i(y)$

n Data points measured

m Parameters estimated by fitting a curve to n points.

The evaluation for Type B is much more complicated. The common practice is carried out in such a manner, that underestimation is avoided. Under this assumption the degrees of freedom are:

$$\nu_i \rightarrow \infty. \quad (6.8)$$

After obtaining the t -factor $t_p(\nu_{eff})$ for the required level of confidence p from a t -distribution table (see [43], p. 66), U_p is calculated as follows ($k_p = t_p(\nu_{eff})$):

$$U_p = k_p \cdot u_c(y). \quad (6.9)$$

The difference between U and U_p is that both report the expanded uncertainty of an output estimate, with U having a *high* level of confidence and U_p having a high, *specified* level of confidence, equal to the corresponding coverage factor times the combined standard uncertainty.

6.2 Laboratory Calibration Uncertainty

6.2.1 Uncertainty Report

a) Identified Sources of Uncertainty

The sources of uncertainty included in the final report include all the measurements performed during the characterization process. Additional sources are the scattering of light due to the coupling of the spectroradiometer to the integrating sphere. This uncertainty is estimated to be less than 0.1%. If measured, results are listed for each detector individually (i.e. Si, PbS1, and PbS2 detector).

b) Identification of Errors (Type A or Type B)

The identification of errors and their classification in Type A and B is listed in Table 6.1 in the second column.

Source	Type	ν_i	$u_c(y)$	$t_p(\nu_{eff})$ (95%)	U_p	Ref. chapter
Measurement Noise (N/S)	A	63	0.46%	2.01	0.92	4.6.1
			1.08%		2.17	
			1.69%		3.40	
Responsivity (Temp.)	B	$\nu_i \rightarrow \infty$	< 0.1%	1.960	0.2	4.6.11
			< 1%		1.96	
			< 1%		1.96	
Wavelength	B	$\nu_i \rightarrow \infty$	0.05%	1.960	0.10	4.6.4
Nonlinearity	A	51	0.20%	2.01	0.40	4.6.5
			0.39%		0.78	
			0.44%		0.88	
Directional and Positional	B	$\nu_i \rightarrow \infty$	< 0.5%	1.960	1.96	4.6.6
Spectral Scattering	B	$\nu_i \rightarrow \infty$	< 0.5%	1.960	1.96	4.6.7
FOV	B	$\nu_i \rightarrow \infty$	< 0.1%	1.960	1.96	4.6.8
Polarization	B	$\nu_i \rightarrow \infty$	< 0.34%	1.960	0.67	4.6.9
Size-of-Source	B	$\nu_i \rightarrow \infty$	$\ll 0.5\%$	1.960	0.98	4.6.10
Integrating Sphere	B	$\nu_i \rightarrow \infty$	2%	1.960	3.92	4.3.2
Drift of Sphere	B	$\nu_i \rightarrow \infty$	2%	1.960	3.92	4.3.2
Scattering by Placeholder	B	$\nu_i \rightarrow \infty$	0.1%	1.960	0.20	n.a.

Table 6.1: Uncertainties for a $\leq 10\%$ laboratory calibration of the GER3700 spectroradiometer at 200 fL.

c) Degrees of Freedom

The degrees of freedom ν_i are based on either the number of measurements performed to determine the necessary parameters, or they are set to infinity. The degrees of freedom are listed in the third column of Table 6.1.

d) Combined Uncertainty u_c

The combined uncertainties $u_c(y)$ are also given in table Table 6.1. The uncertainties for the integrating sphere are listed as 2% for the NIST traceable luminance uncertainty, and 2% is assigned to the drift of the sphere over less than a 100 h operating time (or 1 year). The final combined uncertainties for the instrument are listed in Table 6.2 for each detector type.

Detector	Combined Uncertainty u_c
Si	3.02%
PbS1	3.35%
PbS2	3.60%

Table 6.2: Combined uncertainty for the GER3700 spectroradiometer.

e) Expanded Uncertainty

The expanded uncertainty is calculated using a coverage factor of 2. The final results are listed in Table 6.3 for each detector type separately.

Detector	Expanded Uncertainty U
Si	6.04%
PbS1	6.70%
PbS2	7.20%

Table 6.3: Expanded uncertainty for the GER3700 spectroradiometer ($k=2$).

By introducing a level of confidence of 95% and following eq. (6.9), the expanded uncertainty is given as (Table 6.4):

Detector	Expanded Uncertainty U_p
Si	5.93%
PbS1	6.58%
PbS2	7.09%

Table 6.4: Expanded uncertainty for the GER3700 spectroradiometer using a 95% confidence interval.

f) Conclusions

The NIST traceable calibration of the detectors of the spectroradiometer is listed as follows (Table 6.5):

Detector	Uncertainty
Si	$Y = y \pm 5.93 \%$

Table 6.5: GER3700 spectroradiometer laboratory calibration uncertainty.

Detector	Uncertainty
PbS1	$Y = y \pm 6.58 \%$
PbS2	$Y = y \pm 7.09 \%$

Table 6.5: GER3700 spectroradiometer laboratory calibration uncertainty.

Compared with the initial estimation of all error sources ($Y = y \pm 7.63 \%$, see Table 4.1 on page 25), the expanded uncertainty is better than the first assumptions.

Major factors contributing to the uncertainty are the responsivity mainly influenced by thermal effects in the PbS detectors.

6.3 Absolute Radiance Calibration

6.3.1 Linear Calibration Model

The absolute radiance calibration is performed assuming in a first step a linear relation between the spectroradiometer reading R_{DN} and the at-sensor-radiance L_λ . Since the final goal is to achieve radiance calibrated data and not digital numbers, the inverse model is used to express the calibration coefficients:

$$L_\lambda = C_{gain,\lambda} \cdot R_{DN} + C_{offset,\lambda} \quad (6.10)$$

where

- L_λ Calibrated at-sensor-radiance
- C_{gain} Calibration gain
- R_{DN} Measured value
- C_{offset} Calibration offset ($C_{offset} = R_{dark} \cdot C_{gain}$).

Since the calibration coefficients are wavelength dependent, for each of the spectroradiometer channels both values are plotted (see Figure 6.1).

6.3.2 Temperature Dependent Calibration Model

Because the PbS detectors show a temperature sensitivity that causes significant changes in the resulting spectroradiometer reading, the calibration must also include the temperature sensitivity before stating values for absolute calibrated radiance (see Figure 6.2). The extended calibration formula, based on eq. (6.10) is given below:

$$L_{\lambda,T} = C_{gain,\lambda} \cdot (R_{DN} + k_1 \cdot \exp(-k_2 \cdot T_{PbS})) + C_{offset,\lambda} \quad (6.11)$$

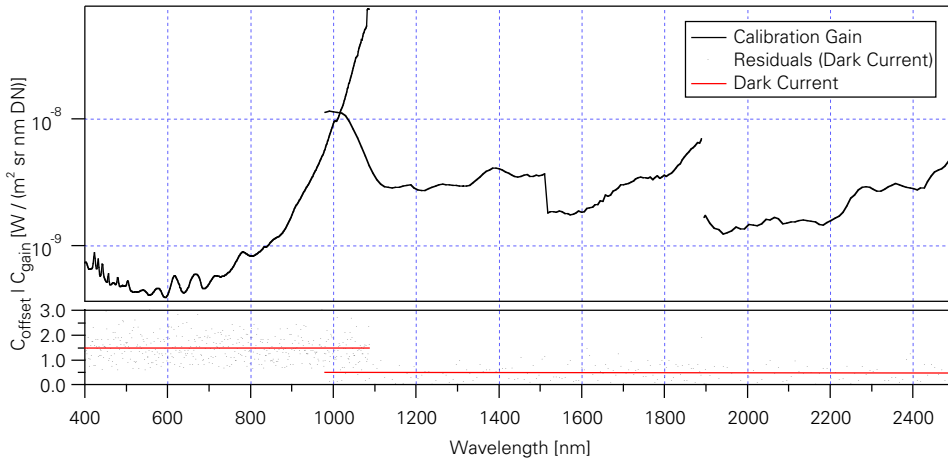


Figure 6.1: Calibration gain and calibration offset for all 704 GER3700 spectroradiometer channels.

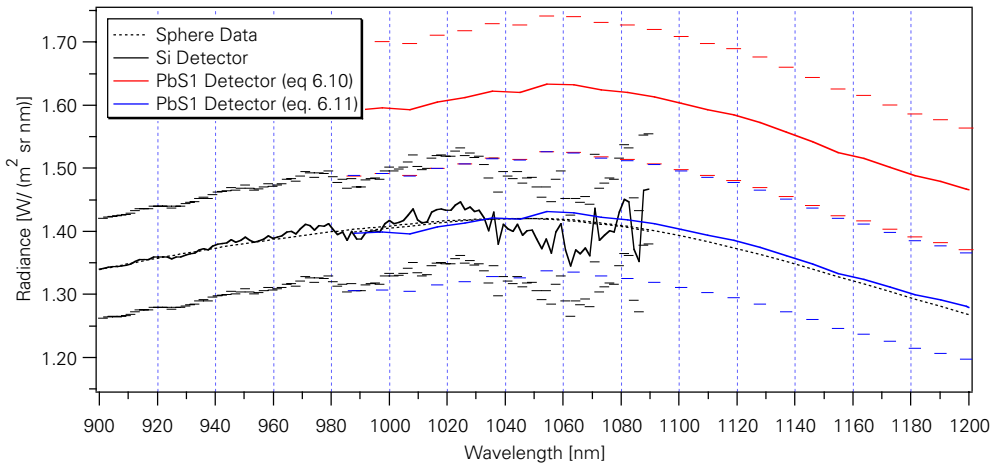


Figure 6.2: Comparison of temperature calibrated (according to eq. (6.11)) and uncalibrated radiance calibration (according to eq. (6.10)) at the detector transition zone.

where

- $L_{\lambda, T}$ Temperature calibrated radiance
- k_n Temperature model fit parameters
- T_{PbS} Temperature reading of the PbS1 detector.

By correcting the temperature sensitivity for the PbS detectors, a better agreement between the predicted and measured values is achieved. Using the 200 fL SNR experiment as reference for the temperature drift, the uncorrected and temperature corrected data are plotted against the integrating sphere reference standard.

A significant difference between the corrected and uncorrected data in this transition area of the two detector elements is visible. The bars around the curves indicate the uncertainty for each spectroradiometer channel. The result presented here is limited to a comparison of the calibration coefficients derived from the same calibration standard used for the verification. Therefore it is more accurate to use the term reproducibility instead of absolute radiometric accuracy. Nevertheless, the uncertainties calculated include the uncertainties of the standard, and the absolute temperature calibrated measurements can be used for comparison with any other instrument.

6.4 Absolute Reflectance Calibration

6.4.1 Uncertainty Report

a) Identified Sources of Uncertainty

The sources of uncertainty include all the measurements performed during the laboratory characterization process. Additional sources include the contribution of uncertainty of adjacency effects (< 1%), the NIST calibrated uncertainty of the Spectralon panel, uncertainty of the solar constant and associated drifts (< 0.1%), and three drift scenarios of absolute changes of the atmospheric properties between the reference and the target measurements (the 2% change is used as reference size for the final uncertainty calculation).

Source	Type	v_i	$u_c(y)$	$t_p(v_{eff})$ (95%)	U_p	Ref. chapter
Measurement Noise (N/S)	A	63	0.46%	2.01	0.92	4.6.1
			1.08%		2.17	
			1.69%		3.40	
Responsivity (Temp.)	B	$v_i \rightarrow \infty$	< 0.1%	1.960	0.2	4.6.11
			< 1%		1.96	
			< 1%		1.96	
Wavelength	B	$v_i \rightarrow \infty$	0.05%	1.960	0.10	4.6.4
Nonlinearity	A	51	0.20%	2.01	0.40	4.6.5
			0.39%		0.78	
			0.44%		0.88	
Directional and Positional	B	$v_i \rightarrow \infty$	< 0.5%	1.960	0.98	4.6.6
Spectral Scattering	B	$v_i \rightarrow \infty$	< 0.5%	1.960	0.98	4.6.7
FOV	B	$v_i \rightarrow \infty$	< 0.1%	1.960	0.20	4.6.8

Table 6.6: Uncertainties for a field reflectance calibration of the GER3700 spectroradiometer.

Source	Type	ν_i	$u_c(y)$	$t_p(\nu_{eff})$ (95%)	U_p	Ref. chapter
Polarization	B	$\nu_i \rightarrow \infty$	< 0.34%	1.960	0.67	4.6.9
Adjacency Effects	B	$\nu_i \rightarrow \infty$	< 1%	1.960	1.96	[8]
Spectralon Panel	B	$\nu_i \rightarrow \infty$	$\leq 2\%$	1.960	3.92	5.3.1
			< 0.5%	1.960	0.98	
Sun	B	$\nu_i \rightarrow \infty$	$\ll 0.1\%$	1.960	0.20	n.a.
Drift of the Sun	B	$\nu_i \rightarrow \infty$	0.1%	1.960	0.20	n.a.
Atmospheric Changes	B	$\nu_i \rightarrow \infty$	0.1%	1.960	0.20	n.a.
			2%		3.92	
			10%		19.60	

Table 6.6: Uncertainties for a field reflectance calibration of the GER3700 spectroradiometer.

b) Identification of Errors (Type A or Type B)

The identification of errors and their classification in Type A and B is listed in Table 6.6 in the second column.

c) Degrees of Freedom

The degrees of freedom ν_i are either based on the number of measurements performed to determine the necessary parameters or they are set to infinity. The degrees of freedom are listed in the third column of Table 6.6.

d) Combined Uncertainty u_c

The combined uncertainties $u_c(y)$ are listed in Table 6.6. The uncertainties for the Spectralon panel are split according to the NIST calibration in < 0.5% for 400–2200 nm and $\leq 2\%$ for 2200–2500 nm. The final combined uncertainties for the instrument are listed in Table 6.7 for each detector type.

Detector	Combined Uncertainty u_c
Si	2.48%
PbS1	2.87%
PbS2	3.15%

Table 6.7: Combined uncertainty for the GER3700 spectroradiometer.

e) Expanded Uncertainty

The expanded uncertainty is calculated using a coverage factor of 2. The final results are listed in Table 6.8 for each detector type separately.

Detector	Expanded Uncertainty U
Si	4.96%
PbS1	5.73%
PbS2	6.31%

Table 6.8: Expanded uncertainty for the GER3700 spectroradiometer ($k=2$).

By introducing a level of confidence of 95% and following eq. (6.9), the expanded uncertainty is given as (Table 6.9):

Detector	Expanded Uncertainty U_p
Si	4.87%
PbS1	5.64%
PbS2	6.23%

Table 6.9: Expanded uncertainty for the GER3700 spectroradiometer using a 95% confidence interval.

f) Conclusions

The magnitude of the uncertainty for reflectance measurements is strongly dependent upon the stability of the atmosphere in the observed wavelength range. Assuming a variability between 0.1 and 10% of the atmosphere, which is most likely in some water vapor absorption bands and in some highly transmittant bands, the magnitude of the uncertainty varies significantly. The NIST traceable field calibration of the spectroradiometer for reflectance values assuming a 0.1%, 2% and 10% uncertain atmosphere for all spectral bands is given as follows (Table 6.10):

Detector	$U_p(u_c(y) = 0.1)$	$U_p(u_c(y) = 2)$	$U_p(u_c(y) = 10)$
Si	$\pm 2.90\%$	$\pm 4.87\%$	$\pm 19.81\%$
PbS1	$\pm 4.06\%$	$\pm 5.64\%$	$\pm 20.02\%$
PbS2 (< 2200 nm)	$\pm 4.85\%$	$\pm 6.23\%$	$\pm 20.19\%$
PbS2 (≥ 2200 nm)	$\pm 6.16\%$	$\pm 7.30\%$	$\pm 20.54\%$

Table 6.10: Field calibration uncertainties of the GER3700 spectroradiometer for three different atmospheric conditions including the Spectralon uncertainty for higher wavelengths.

According to Figure 5.5, the spectrum can be redrawn using the 0.1% assumption for atmospheric changes and the water absorption bands are omitted because of this restriction (see Figure 6.3).

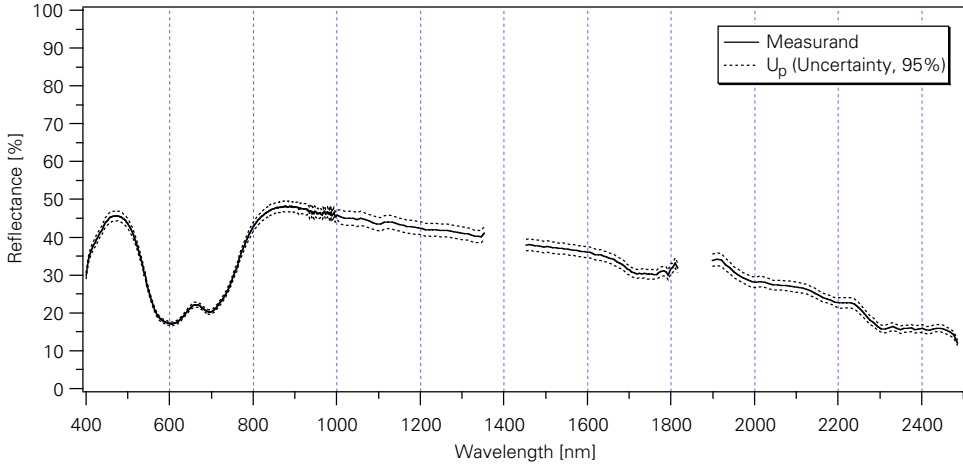


Figure 6.3: NIST calibrated field reflectance spectrum using a 95% confidence interval.

A closer look at a detail between 2100 and 2300 nm demonstrates the change of the calibration uncertainty because of the change in the NIST certified uncertainty for wavelengths exceeding 2200 nm (see Figure 6.4).

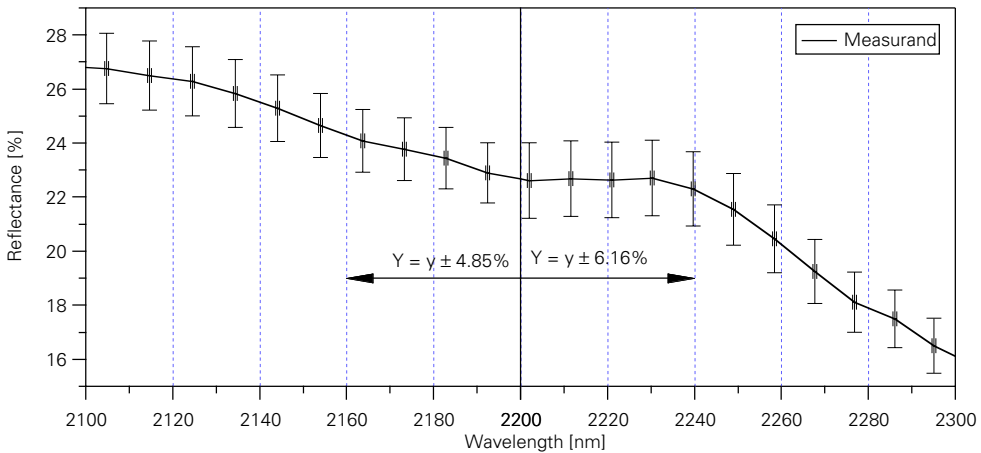


Figure 6.4: Uncertainty change at 2200 nm of the NIST calibrated reflectance spectrum.

6.5 Conclusions

Two fundamental methods for calibration of a spectroradiometer have been presented: The radiance based calibration with the final goal to measure absolute radiance values with an associated uncertainty; and the reflectance based calibration for the measurement of field reflectances also associated with an uncertainty. Performed to this extent, both methods are expensive in terms of time consumption and instrumentation needed. But the accuracy achieved with this calibration is important for applications where the measurement within the absorption bands of the atmosphere is performed; such as in the water vapor band around 940 nm and others.

It is inappropriate to define a set of calibration parameters once in the lifetime of a spectroradiometric measurement instrument. Also there is no calibration strategy available that automatically generates calibration coefficients as a function of time. As a consequence, the interference of scientists will always be required to calibrate this kind of instrument. Discussion over calibration effort versus calibration accuracy can only be resolved satisfactorily if the figures of merit for a calibration are normalized so that they allow a transparent comparison with other instruments. In addition, predictable accuracies, or at least modelable ones, are required to determine the extent of the calibration effort.

The required calibration accuracy helps to estimate the calibration effort needed and can also be a helpful measure to define the required recalibration frequency. Any spectroradiometric measurement device tends to drift over time. These drifts generally introduce a higher uncertainty over time and therefore the overall calibration accuracy might suffer from inappropriate recalibration intervals.

Certainly there are limitations to the calibration effort. Laboratory calibration reduces the operational time of the instrument and binds many resources to the calibration process. After the laboratory calibration the instruments needed for the laboratory calibration are—in the worst case—not accessed until the next recalibration task. Inefficient resource allocation and ageing of the calibration instrumentation introduces even higher costs to the calibration effort.

When it comes to the comparison of calibrated instruments, or even when trying to evaluate and acquire instruments, the figures of merit must be clearly defined to allow for a proper estimation of an instrument's capability.

Table 6.11 lists the figures of merit suggested for the evaluation, and compares the performance of different field spectroradiometer systems. For most of the parameters listed there exist a wavelength dependency that should be declared by the manufacturer. In addition, it would be most beneficial if the uncertainty is stated for each independent source, and the quality of the standards used for absolute radiometric calibration declared.

Figure of Merit	Sign	Units
Focal length	f	[mm]
f -number	$f\#$	[-]
Field of view (FOV)	θ_f	[rad], or [°]
Number of channels		[-]
Diffraction elements		[-]
Detector types		[-]
Detectivity	D^*	[-]
Quantization rate		[bit]
Signal to noise ratio	SNR	[-]
Noise to signal ratio	NSR	[-]
Noise equivalent signal	NES	[DN]
Noise equivalent radiance	NER	$[W/(m^2 \cdot sr \cdot nm)]$
Dark current	R_{dark}	[DN]
Wavelength range	$\hat{\lambda}$	[nm]
Center wavelength	$\hat{\lambda}_{CW}$	[nm]
Spectral sampling interval	$\hat{\lambda}_{i+1} - \hat{\lambda}_i$	[nm]
Spectral resolution	$\hat{\lambda}_{FWHM}$	[nm]
Nonlinearity factor	K_{ab}	[-]
Polarization sensitivity	$D(M)$	[%]
Polarization dependent loss	$PDL(M)$	[%]
Temperature sensitivity	R_T	[K]
Combined uncertainty	u_c	[%]
Expanded uncertainty (coverage factor 2, or calculated)	$U, (U_p)$	[%]
Calibration gain	C_{gain}	$[W/(m^2 \cdot sr \cdot nm \cdot DN)]$
Calibration offset	C_{offset}	$[W/(m^2 \cdot sr \cdot nm)]$

Table 6.11: Suggested figures for the comparison of field spectroradiometers.

Chapter 7:

Vicarious Calibration

7.1 Introduction

After having discussed the laboratory calibration of a non-imaging spectroradiometer, the focus in this chapter is on the performance validation of an imaging spectrometer in a field experiment. Imaging spectrometers acquire the spatial extent of the image using across-track scanning techniques (e.g. pushbroom, whiskbroom, etc.) and their inherent velocity along track. The spectral domain of any imaging spectrometer is recorded in the same manner as with non-imaging instruments.

Assuming an imaging spectrometer having 200 spectral channels and 512 spatial pixels in a row, a full data take composed of 512 scan lines will have more than 52 mio. pixels that must be individually calibrated. Again assuming that for each pixel a characterization matrix must be applied in a way like that presented in Table 6.11, the calibration data set might easily exceed the size (and complexity) of the actual data take. Without the existence of predefined inter-relationships between all these pixels, the calibration effort cannot be managed and predicted in a satisfactory manner. The amount of inter- or extrapolation needed to derive the relevant calibration information is closely related to the data quality and applicability of subsequent methods, such as the delineation of geophysical parameters from absolute radiance or reflectance data.

None of the today's existing hyperspectral imagers provide calibration information for each pixel acquired during the data acquisition. Technically it is not feasible to point at the same time to a calibration standard and recording image data. Nevertheless, the two predominant acquisition types (e.g. pushbroom and whiskbroom) used in hyperspectral imaging so far have their individual advantages of in-flight calibration possibilities. Whiskbroom instruments can scan a reference at the end of each scanline (e.g. AVIRIS [13][68], DAIS [33][61][62], etc.) and the calibration information must then be extrapolated to each pixel within one scanline. Pushbroom instruments (e.g. APEX [28], HSI [105], HYDICE [3], etc.) can point permanently with parts of the detector onto a calibration reference, or they may scan a reference using a tilting mirror before and after the data take.

The major problem of imaging spectrometers calibrated in the laboratory is

that their operating environment, when acquiring data under ‘real’ conditions, differs significantly from the laboratory environment (e.g. temperature, pressure, humidity, vibrations, etc.). This again introduces uncertainties to the calibration process that must be well quantified. Independent means of system calibration are required to confirm that the airborne operated instruments are performing as predicted and expected, and that the calibration does not drift in an unpredictable manner. Technical means such as optimizing the operating environment to laboratory conditions (or vice versa) include athermalization efforts, temperature stabilization and pressurizing the instrument to significantly decrease the calibration uncertainty. In-flight calibration and validation experiments are therefore always important to verify the performance under natural illumination conditions.

7.2 Vicarious Calibration

The term ‘vicarious calibration’ was used first in the early 1980s. According to Slater [103], Koepke [49] is the first one to use this term to describe the calibration of a satellite by reference to a typical, but *not simultaneously* measured, ground scene and atmospheric condition. In a more restricted way, access to the selected ground site *at the time* of image acquisition is preferred in more restrictive experiments (e.g. AVIRIS [37], general high spatial resolution space sensors [77], SPOT [88], DAIS 7915 [91], and HYDICE [114]).

All the necessary quantities to determine the atmosphere and the observed objects are measured during the overflight of the remote sensing instrument to predict the amount of radiation present at the sensor using a forward RTC approach. Two major methods of vicarious calibration approaches [101] are discussed here, and one is applied to a sensor.

a) Reflectance Based Approach

The reflectance based approach relies on characterizing the surface reflectance of a selected target at the time the sensor acquires an image of the target in the solar reflective range of the electromagnetic spectrum. Usually this is done by using a ground based spectroradiometer, together with a white reference such as a Spectralon panel described in chapter 5. The method relies also on characterizing the atmosphere between the reference target and the sensor at the time of the overflight. The characterization of the atmosphere is performed using radiosonde data to describe the vertical composition of the atmosphere and a sunphotometer to estimate the visibility from optical thickness measurements. All these data are used together with a radiative transfer code to convert the measured ground reflectance to the at-sensor-radiance, correcting for scattering and absorption induced by the atmosphere for the specific target.

b) Radiance Based Approach

This method is somewhat similar to the reflectance based approach. In this case,

a well calibrated radiometer is used instead of reflectance based measurements. Preferably the radiometer is flown in a small aircraft or helicopter at an altitude of at least 3 km above the selected calibration site. Since then most of the atmospheric aerosols and water vapor are concentrated below the aircraft flying altitude, the radiances measured are comparable to the at-sensor radiances of the imaging spectrometer in space. A minimal atmospheric correction is required to compensate for the path differences between the spaceborne sensor and airborne imaging spectrometer.

Special disadvantages of this method include the more complex instrumentation setup (e.g. additional aircraft / helicopter required) and the coordination effort. Temporal variations of the atmosphere can be measured using a sunphotometer, but since these effects are spatio-temporal effects, the definition of atmospheric properties at the location of the spectroradiometer built in the helicopter or aircraft remains difficult [90].

7.3 Vicarious Calibration Experiment (Reflectance Based Approach)

7.3.1 Experiment Description

a) Instrumentation Setup

The airborne instrumentation used for this vicarious calibration experiment is the hyperspectral imager DAIS 7915 [9] flown aboard a Dornier DO-228 aircraft. The DAIS 7915 is operated by DLR in Oberpfaffenhofen near Munich / Germany. The instrument is extensively calibrated in the laboratory [33] and a complete processing and archiving chain is operated at the DLR for fast data evaluation and processing. The DAIS 7915 has 72 channels in the reflective part of the electromagnetic spectrum and 7 channels in the mid-infrared and thermal infrared regions of the spectrum. The characteristics of the DAIS 7915 are listed in the Appendix (Table 1 on page 133, and Table 2 on page 133).

Also in the same aircraft, the Wide Angle Airborne Camera (WAAC) is flown at the same time over the calibration test site. The calibration experiment focuses only on the hyperspectral in-flight validation, so the data analysis of this camera is not discussed in detail here (but is found in [71] and [72]).

The ground equipment used for the validation experiments are listed as follows (Table 7.1):

Instrument / Equipment	Reference	7/23/96	9/8/97
GER3700 spectroradiometer	chapt. 3.3	X	X
ASD fieldSpec spectroradiometer	[22]	X	X

Table 7.1: Ground equipment for two validation experiments in Central Switzerland.

Instrument / Equipment	Reference	7/23/96	9/8/97
Sunphotometer	chapt. 3.4, [95]	X	X
Radiosonde	[91]	X	–
Blank Aluminium Targets	[93]	–	X
Black Aluminium Targets	[93]	–	X
Heated Aluminium Targets	[93]	–	X
Differential GPS (ground station)	[93]	–	X
GCP towels	[93]	–	X

Table 7.1: Ground equipment for two validation experiments in Central Switzerland.

Simultaneously to the overflight, field reflectance measurements are performed before and after the validation experiment at similar sun–zenith angles (see [47][112]).

b) Test Site Selection

The test site selected is the standard test site of RSL located in Central Switzerland about 20 km south of Zürich near the village ‘Küssnacht am Rigi’. The calibration site consists of natural (e.g. soccer field (grass), and meadow) and artificial (e.g. gravel, green soccer field, red coating) targets. Figure 7.1 is a zoom

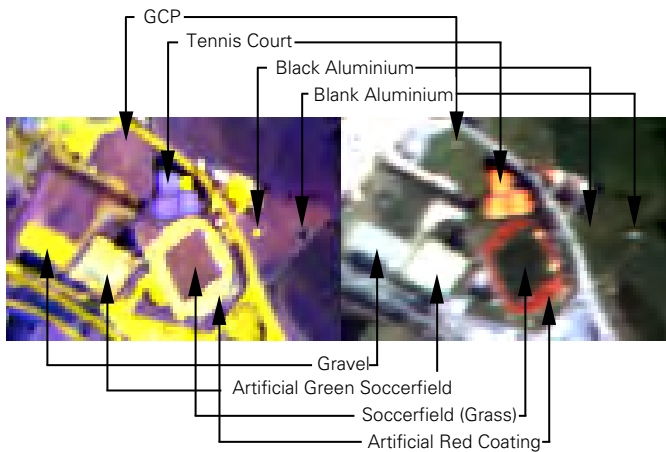


Figure 7.1: DAIS 7915 vicarious calibration site in Central Switzerland (Thermal IR left image, VIS right image).

into this area, where the left image is a thermal image and the right image a visible image from the data take on August 9, 1997. Bright objects in the left image have a high emissivity and bright objects on the right image have a high reflectivity.

The thermal calibration targets (aluminum) are clearly identified on the thermal

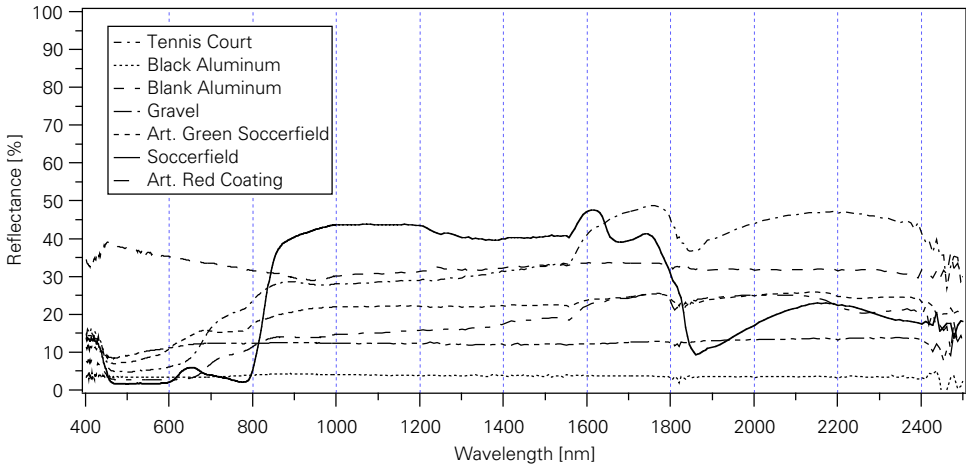


Figure 7.2: Corresponding spectral signatures to the objects listed in Figure 7.1.

image, where on the visible image the black aluminum target has only a 5% reflectance and cannot be identified (see also Figure 7.2).

Major factors driving the proper selection of reference targets are dependent on the kind of instrument to be calibrated. Spatial uniformity, temporal stability, the magnitude of directional effects (e.g. BRDF), and radiometric homogeneity are selection criteria that must be included in any evaluation. Since airborne instruments are much more flexible, cloud cover of the calibration site is only a factor to be considered using satellite based instruments where the repeated coverage of the calibration site might interfere with the cloud coverage [20]. The major drawback of airborne instruments with respect to in-flight calibration experiments is their limited operating range and the availability of adequate calibration sites within this operating range.

In a Mid-European environment it is nearly impossible to identify calibration sites having a predictable stability of all the abovementioned factors, and whose uncertainty does not exceed the expected calibration uncertainty. As a consequence, in-flight validation experiments, or radiance and reflectance based vicarious calibration experiments, must be carried out at the same time of the overpass of the instrument. The amount of vegetation present in frequently used test sites (e.g. La Crau [87]) increases the natural temporal variability, and therefore increases the overall uncertainty.

The proposed calibration site for in-flight validation and calibration in Central Switzerland must be accessed every time a calibration overflight is planned, and the measured data might not be extrapolated between individual measurement campaigns. The expected variability of the selected artificial and natural surfaces will in any case exceed the overall calibration uncertainty.

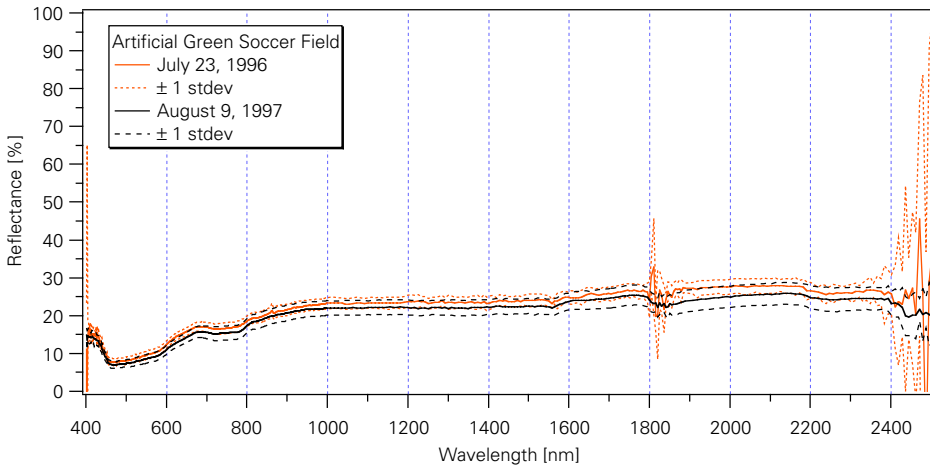


Figure 7.3: Artificial green soccer field covered with quartz sand measured in the two calibration campaigns.

In Figure 7.3 the same artificial green soccer field is measured in the two calibration campaigns carried out with the DAIS 7915. The standard deviation plotted for both measurements results from averaging 9 different spots on the field averaging 7 (1996) and 15 (1997) measurements respectively. The difference of these spectra also results from uncalibrated (1996) and fully calibrated (1997) instruments and the difference in illumination geometry.

The largest more or less homogenous area in the selected calibration site is a

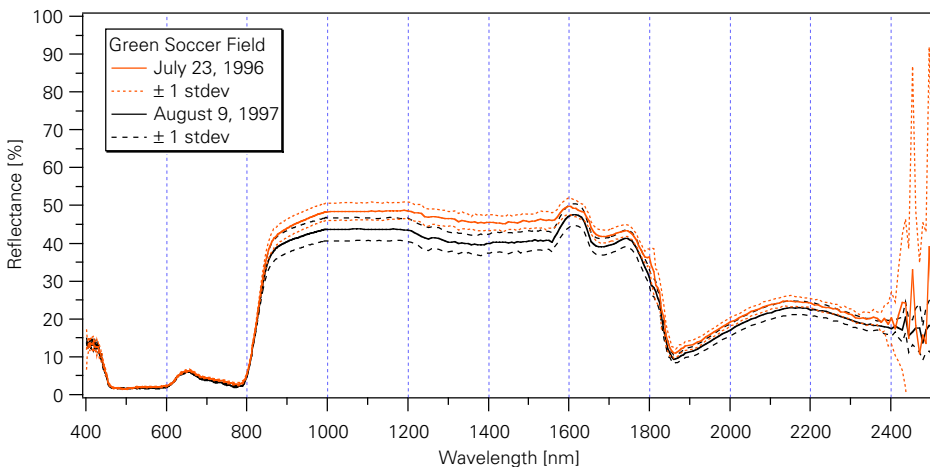


Figure 7.4: Green soccer field measured in two different calibration campaigns.

soccer field surrounded by a red (tartan) race track. The reflectance differences

depicted in Figure 7.4 are a result of the calibration effort between the two years. This soccer field has been used for the validation of the sensor performance in general. The selection of this field is optimized according to a suggestion of Richter [77] on the selection of small ground targets for calibration purposes. The spatial extent of such a reference area should be 7 x 7 GIFOV's, (i.e. in the case of the DAIS 7915 in Switzerland approx. 36 x 36 m), spatial homogenous (i.e. < 2.5%), a high temporal stability and 'flat' reflectance properties over the whole spectrum [91].

The target is also located close to the nadir pixel of the imaging sensor. The flight path is adapted accordingly to minimize uncertainties introduced by off-nadir looking angles.

7.3.2 Modelling the At-Sensor-Radiance

The measured reflectance data for the green artificial soccer field (e.g. the spectrally most flat spectrum) are modeled to at-sensor-radiances. A sensitivity analysis is carried out to determine the uncertainty of the modeling approach. Four approaches are compiled for the input in the RTC for comparison of the model with the calibrated DAIS 7915 data [91]. The four approaches include the input of

- the measured radiosonde data and the field observer estimated horizontal visibility [Model 1],
- the use of a predefined RTC setting (e.g. midlatitude summer) and the field observer estimated horizontal visibility [Model 2],
- the measured radiosonde data and the sun-photometer data (e.g. this is the complete measurement approach) [Model 3], and
- the predefined RTC setting (e.g. midlatitude summer) and the sun-photometer data [Model 4].

The results are convolved with the DAIS spectral response function [94][111] and are plotted in Figure 7.5. Model 3, because of its best reproducibility, is chosen for the final comparison with the DAIS 7915 sensor on the selected reference targets.

An atmospheric correction of the adjacency effect of the 59 DAIS 7915 pixels identified within the green artificial soccer field is performed [76]. This correction is finally compared with the associated uncertainties of both the laboratory calibration of the DAIS 7915, and the modeling approach. The final comparison of the modeled at-sensor-radiance of the DAIS (see Figure 7.6) and the laboratory calibrated and adjacency corrected DAIS data are within the expected $\pm 10\%$ uncertainty for this kind of measurement (see Figure 7.7).

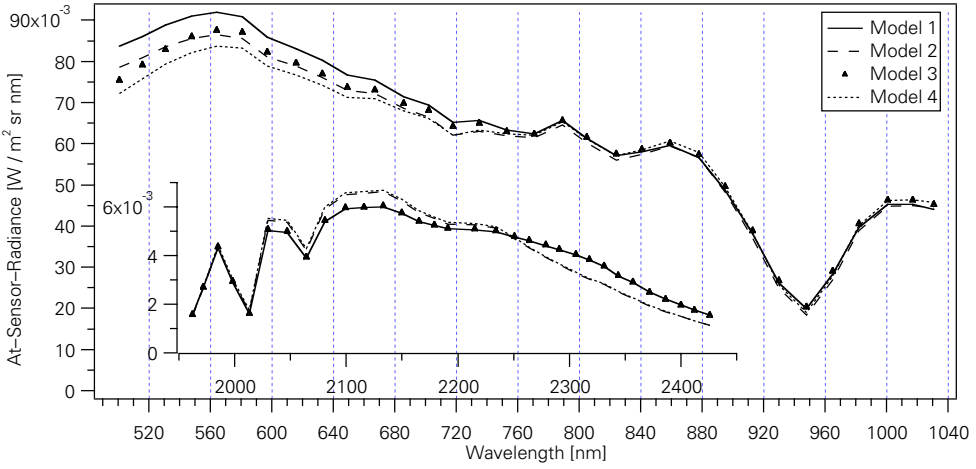


Figure 7.5: Four modeling approaches for the prediction of at-sensor-radiance of the DAIS 7915 in selected spectral channels [91].

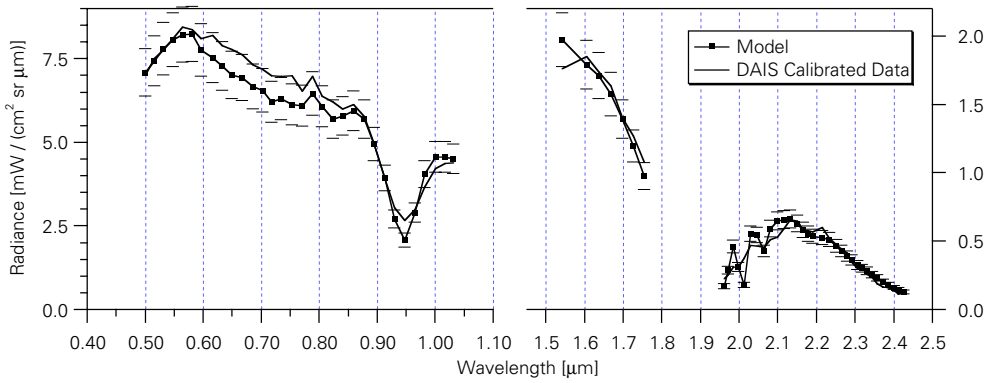


Figure 7.6: Comparison of DAIS calibrated radiance data and MODTRAN predicted at-sensor-radiance of an artificial green soccer field [111].

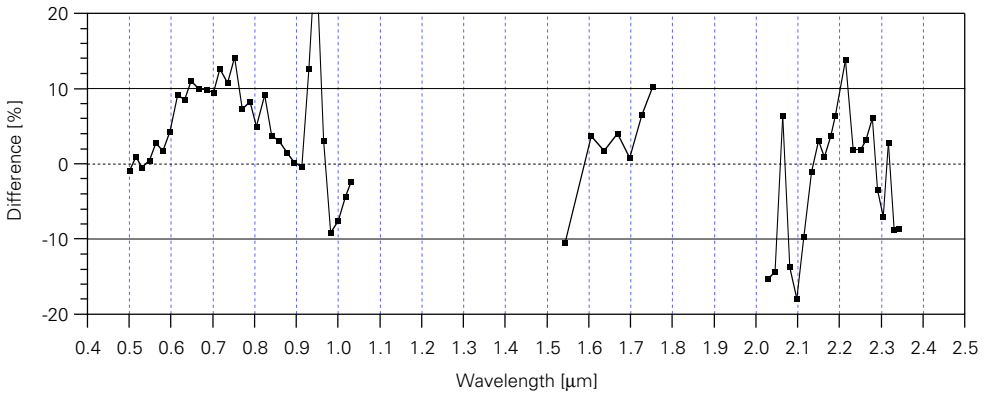


Figure 7.7: Percent deviation of the comparison in Figure 7.6, omitting bands with a SNR < 5 [111].



Figure 7.8: Partial DAIS 7915 scene (recorded August 9, 1997) over Central Switzerland (VIS left image, thermal IR right image; data processing courtesy by P. Strobl, DLR).

A part of a recorded scene by the DAIS 7915 is displayed in Figure 7.8. The left part is a composite using the DAIS channels 12, 6, and 2 (0.689 , 0.587 , and $0.517 \mu\text{m}$), whereas the right image is a false color combination using the channels 76, 73, and 38 (10.482 , 4.371 , and $1.678 \mu\text{m}$). The image dimensions are 512 pixels in scan direction and 1500 lines in flight direction. The flight line heads from East to West equalling top to bottom on this image. The upper part of the image is covered by Lake Zug, and in the center of the image the village of ‘Küssnacht am Rigi’ is located, where the reference areas are measured.

Chapter 8:

APEX – Airborne PRISM Experiment

8.1 Introduction

After having discussed the radiometric calibration of non-imaging spectroradiometers and their use for vicarious calibration purposes, the radiometric requirements for an imaging spectrometer are defined. The design of the imaging spectrometer itself is based on an ESA initiated study for the definition of an airborne imaging spectrometer [24].

The design of the instrument presented is based on a feasibility study carried out by a number of industrial partners [28]. A specific sensor model and a discussion of the radiometric requirements for an airborne imaging spectrometer finalize this chapter.

8.2 The Airborne PRISM Experiment

After the successful operation of ERS–1 and ERS–2, the European Space Agency has set the scene for an environmental mission by preparing the satellite ENVISAT–1 [30].

In formulating European Earth Observation missions beyond this, ESA is considering the development and launch of four explorer missions, including a high resolution Land Surface Processes and Interactions Mission (LSPIM) [31]. During this mission it is intended to develop a system to investigate land surface processes and their interactions with the atmosphere. This includes the implementation of data acquisition from an advanced high resolution spectrodirectional space sensor, and support of development of the tools and techniques of data interpretation to:

- increase understanding of biophysical processes and land/atmosphere interactions at the local scale; and
- exploiting the increase in knowledge of (small scale) processes, and to advance the understanding of these interactions on a global scale by extrapolating through time and space using process models.

The space segment would be characterized by:

- a single satellite in a near-polar orbit capable of enabling the payload to access all land areas with the required geometric and temporal characteristics; and
- a hyperspectral imager with the required spatial and spectral resolution covering the optical range of the electromagnetic spectrum with good radiometric accuracy and with the capability to perform directional measurements providing the required accessibility and revisit characteristics [25].

A preliminary design at system level of satellite instrumentation fulfilling this goal started under the name Process Research by an Imaging Space Mission (PRISM). This instrument will combine the main features of a visible/short wave infrared imaging spectrometer and a thermal infrared multi-channel imager. PRISM would cover two main wavelength regions, namely the visible-short-wave infrared from 0.45 to 2.35 μm , where the instrument works as an imaging spectrometer with a spectral resolution of about 10 nm, and the thermal infrared range from 8 to 12.3 μm , divided into 3 spectral bands with a typical width of 1 μm , where the instrument works as an imaging radiometer. The spatial resolution at nadir is about 50 m over a swath (image size) of 50 km. Access to any site on earth could be provided within three days.

In order to support such activities, ESA has identified the necessity to initiate appropriate studies and measurement campaigns. In this frame, this work discusses a study that concentrates on the definition of an airborne imaging spectrometer which could represent a precursor of the spaceborne instrument and which will therefore be named APEX (**A**irborne **P**RISM **E**xperiment) [24]. APEX is a project to develop an airborne PRISM simulator which will contribute to the

- preparation,
- calibration,
- validation,
- simulation, and
- application development

of the PRISM mission. In addition, APEX will be an advanced imaging spectrometer serving as a testbed for other imaging spectroscopy applications [44]. The schematic block diagram of the APEX system is depicted in Figure 8.1.

8.3 APEX – The Instrument

APEX will be an instrument with the following unique capabilities from a technical, usage and applications standpoint [24]:

- pushbroom imager with ≤ 1000 pixels across track and a swath width of 2.5 – 5 km
- spectral wavelength range covering 450 – 2500 nm
- 200 programmable or 300 predefined bands, adapted to the specific mission and application

- a spectral sampling interval < 15 nm at a spectral sampling width < 1.5 times the sampling interval
- ability to provide calibrated data and a suite of user oriented products up to fully geocoded and calibrated data.

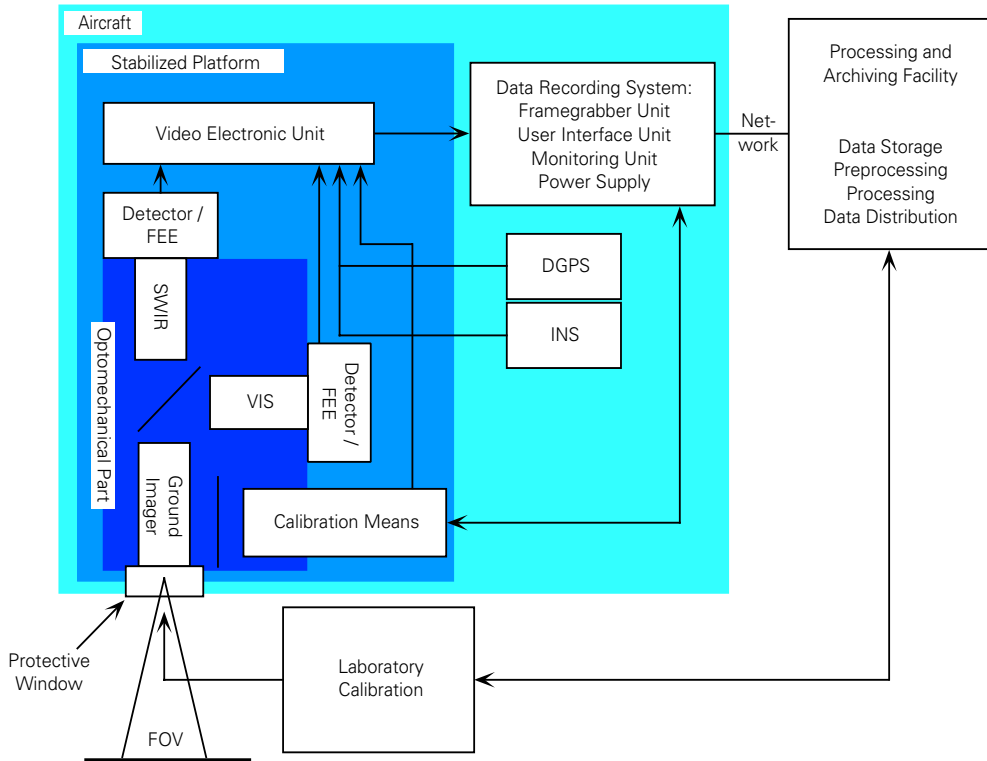


Figure 8.1: Schematic APEX block diagram [44].

8.3.1 The Imaging Spectrometer Optomechanical Subsystem

The ground imager maps the ground (swath of $\pm 14^\circ$) on the spectrometer slit of 50 mm height and 0.05 mm width. High image performance is required in order to provide maximum energy throughput at the slit and to define the swath width precisely. The ground image has to be color corrected in the total spectral range between 450 and 2500 nm. Behind the ground imager a beam splitter will be placed to separate the spectral range into a visual and an IR channel. The use of a beam splitter in front of the collimators allows the choice of more suitable glasses for the color correction and for improving the transmission within the reduced number of spectral bands. The two collimators project the light coming from the slit towards the dispersive elements of the spectrometers.

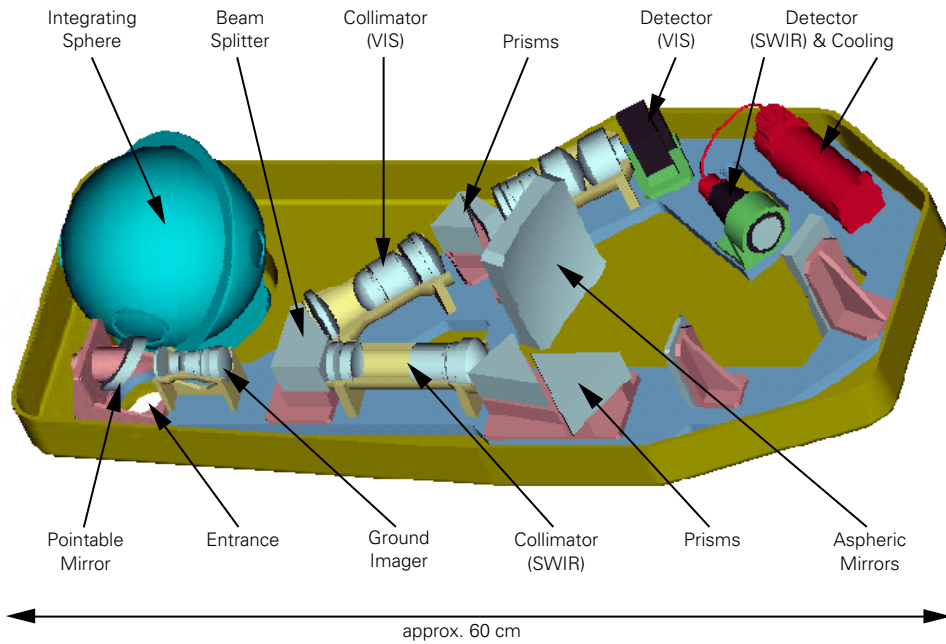


Figure 8.2: APEX instrument layout (visualization courtesy OIP n.v.) [28].

Prisms will be selected as dispersing elements. Light scattering in a system containing gratings is considered to be a risk that cannot be taken. For the visual channel, the prism materials CaF_2 / ZnS are selected. For the IR channel the prism materials are CaF_2 and Sapphire.

Finally detector lenses are selected to provide spatially and spectrally resolved images on the matrix detectors. The VIS detector is tilted by 30° to correct for image height differences at the individual wavelengths. The IR detector lens consists of three off-axis aspheric mirrors. The use of reflective elements simplifies the color correction, supports the compensation for image bending and improves the total throughput for better signal to noise ratios.

The APEX instrument layout as finalized in the Phase A study [28] is visualized in Figure 8.2.

8.3.2 Detectors and Front End Electronics

In the APEX instrument, two detectors are needed to cover the specified spectral range:

- a VIS detector, sensitive in the spectral range 450 - 950 nm (Si CCD), and
- a SWIR detector, sensitive in the spectral range 900 - 2500 nm (HgCdTe).

The detectors for the APEX instrument have to be two dimensional array detectors. To meet the initial specifications, the detector arrays must have ≤ 1000 pixels in the spatial, and ≤ 200 pixels in the spectral direction.

The FEE for the VIS detector will be realized by using photocopacitors and CCD readout structures. The analogue output signal of the CCD is sampled and converted to digital data by an A/D converter.

The HgCdTe detector will be read out by a CMOS circuit. The array consists of a number of addressable pixels using MOS transistors as switches, controlled by an x and y multiplexer. The detectors will be glued in their holders. Alignment (translation) will be done making use of shims. To reduce dark current noise, the IR detector needs to be cooled to a temperature of -80° C. The cooling is achieved by means of a cooling engine. Care has to be taken that no vibrations caused by the cooling engine disturb the image quality of the system.

8.3.3 Electronics Unit

The electronics unit consists of the video electronics unit, the framegrabber unit, the data storage unit, and the user interface unit which incorporates four basic operating modes to control the APEX instrument:

- mission preparation – before a data acquisition mission, all parameters and sequences are determined and stored in the system,
- calibration mode – the calibration sequence is initiated and the calibration data stored,
- acquisition mode – the instrument stores the data being transferred from the detectors to the electronics, and
- stand-by mode – all the values stored or transferred into the instrument stay active but no acquisition is performed.

The proposed video chain of the system consists of an analogue ASIC that assures the necessary stability. The next device is an internal offset loop correcting the offset recorded from some darkened border pixels of the detectors. This allows for subtraction of the dark current of the system in near real time. The calibration effort might therefore be reduced substantially (e.g. the offset of the system is not to be considered). Finally the A/D converter will take care of the signal conversion for feeding into the framegrabber. The framegrabber itself is capable of transferring 200 lines of 1000 12 bit pixels each 41.55 ms. This throughput corresponds to a data-rate of 57.8 Mbit/sec. for each channel.

In the mission preparation phase, the operator of the instrument must select 200 channels that will be recorded out of 400 lines accumulated by the detectors. The channel selection is stored in a PROM, and multiple PROM's can be selected within one data acquisition flight. Other concepts foresee a fixed readout of 300 simultaneously recorded bands.

The calibration mode will be used in the laboratory where the operator has the choice to address basically all moving parts and controls in the APEX system. During a real data flight, the instrument will be first in calibration mode and over the desired test site in acquisition mode. A moving window display will be used in the APEX control unit to monitor the functionality of the detectors. Two hundred frames corresponding to one scan line will be recorded continuously every

41.55 ms. The framegrabber unit, the data storage unit and the user interface unit are mounted in racks that are located in the cabin of the aircraft. The video electronics unit is a part of the APEX instrument.

8.3.4 Auxiliary Components

In order to make the APEX imaging spectrometer system operational, the following auxiliary components must be available:

- an aircraft platform
- a closed environment for the APEX instrument
- a stabilized platform
- a differential GPS and accelerometers
- in flight calibration means
- laboratory calibration hardware
- equipment for temperature and pressure control
- vibration and shock absorbers.

8.3.5 The Aircraft and Navigation

The APEX instrument, when installed in an aircraft, will be in a protected and closed and temperature stabilized environment. The pod or box containing the APEX instrument has an optical window made of sapphire. During takeoff and landing a mechanical shutter will be closed in order to protect the window from dust and other contaminants.

The PILATUS PC XII Eagle is the proposed survey aircraft for the operational missions of APEX. The crew will consist of an aircraft pilot and the APEX operator. In order to guarantee the geometric quality of the recorded scenes, accurate navigation data have to be provided. At present, the concept is to use the autopilot of the aircraft plus differential GPS and an inertial navigation system, and to record this data simultaneously for each scanline to the actual scene.

The vibration decoupling of the APEX instrument and the aircraft mounts shall be effected by means of shock mounts.

8.3.6 The Calibration

The primary goal of the calibration strategy is to achieve absolute radiometric calibration traceable to an established standard such as NIST for the acquired data. It is necessary to achieve the best possible radiometric accuracy performance in order to be able to validate PRISM and other imaging spectrometers. It is furthermore considered to use standard hardware technology to reduce the amount of calibration costs for in-flight characterization. In general, there is no in-flight calibration foreseen during data acquisition, but in-flight pre- and postdata acquisition calibration activities allow for monitoring of the instrument's performance.

a) Laboratory Calibration

An integrating sphere will be used in the laboratory as the calibration standard for characterizing the radiometric response function. The sphere is used as a secondary calibration standard, traceable to NIST standards. An irradiance lamp source will be used in conjunction with a (double) monochromator to calibrate the spectral response function. The spectral response function for each channel covering the whole wavelength range (450 – 2500 nm) will be measured in 0.5 nm intervals using different diffraction gratings. The calibration of the geometric response function will be done using an illuminated slit that is projected perpendicular to the slit in the focal plane of a collimator. The calibration hardware will also include a PC that controls all the necessary devices and collects the calibration data.

In the laboratory, the system will be able to scan both the internal sphere and the laboratory sphere using a switchable mirror in the optical path. Built into the electronic part of the APEX, the compensation offset loop will subtract dark current estimated from the darkened border pixels of the respective detector lines during any data recording with the instrument. The traceability between the laboratory sphere and the APEX sphere can be established during these measurements.

The pre-flight calibration will be more a general functionality test of the instrument than a calibration traceable to a standard. It is suggested to use a homogenous, diffuse artificial lamp source to illuminate the instrument from below the aircraft. The instrument must be fully operational and ready for data acquisition.

The in-flight calibration is divided into three parts. The pre-scene calibration will take place just before the data acquisition. The shutter of the sphere will be closed, and dark current frames are to be recorded while pointing the FOV into the integrating sphere. Then the shutter of the instrument opens and the built in integrating sphere illuminates a mirror that deflects the beam of the FOV towards the ground imager. After these calibration tasks, image data from the scene can be acquired. Similar to the laboratory calibration hardware, the in-flight calibration hardware of the APEX system consists of an integrating sphere calibration standard. The features associated to this sphere will be similar to the one evaluated for laboratory use, but due to space constraints in the pod must be smaller in total diameter.

There will be no in-flight calibration during ground data collection. The image data acquired are only dark current subtracted. After having recorded one scene or a sequence of scenes, the internal mirror will switch and deflect the FOV towards the internal integrating sphere again.

Vicarious calibration experiments are performed on selected test flights according to the description in Chapter 7. For data takes in other test sites, provisions must be made to provide on site reference measurements of selected targets and the atmosphere.

8.3.7 Data Handling

The data acquired will be processed with a given number of intermediate steps. Each of these processing steps will produce an output that represents a defined processing level (i.e. 0 to 3) that will be distributed to the customer, or undefined levels that are for internal use and archiving purposes of raw data and intermediate processing steps only.

After downloading the data from the aircraft they will be transferred to the processing facility (Level 0). The first analysis of the data incorporates the generation of quicklooks. The data will then be reformatted to the scenes level (Level 1). After the predefined calibration is applied to the data, the sensor specific calibrated data are archived as Level 1A. The final Level 1D includes the spectral and geometric calibration. Level 2 data products include parametric geocoding and atmospheric correction. The final processing step (Level 3) will depend on user-defined processing requests and require application-specific analysis methods. An overview of the processing levels is listed in Table 8.1.

Action	Comment	Processing Level
Downloading of the flight recording media	Raw data	Level 0
Assessment of raw data quality Generation of quick-look product		Quick-look
Reformatting and archiving of the raw data Formatting the housekeeping channel data Geolocating and archiving of scene attribute data	'Scene'-level	Level 1
Calibration processing Sensor specific calibration Geometric response function Spectral response function, absolute calibration	Sensor geometry (+1A) Sensor radiometry (+1B)	Level 1A Level 1B Level 1C
Value added product generation		Level 2
Geocoding using a parametric approach	DEM required	Level 2A
Atmospheric correction using RTC	Atmospheric data required	Level 2B
Scientific product to be distributed (absolute radiance calibrated data)	Level 1C+2A+2B	Level 2C
Application of special analysis methods	Processed upon request	Level 3

Table 8.1: Processing levels of the APEX processing and archiving facility (PAF) [28].

8.3.8 Operationalization

After a successful development phase of the APEX system, the experiment will be made available for an operational phase for a wide remote sensing community interested in hyperspectral imaging. During this realization phase of the APEX, assessments of the following points must be undertaken:

- definition of a concept for a reference mission
- estimation of the costs associated for such a mission
- identification of potential customers
- planning of the APEX utilization phase.

To a customer, APEX will not only be an instrument but will consist of the remote sensing project team. This team is responsible for marketing the services and applications provided by APEX, assuring the technical performance of the instrument, managing the missions, and providing the customer with the data according to the requested processing level. The aircraft operator is responsible for items such as flight planning, clearances, flight execution, etc. The flight crew will consist of the aircraft pilot and an operator associated with the correct recording of the requested scenes and the proper operation of the instrument during data acquisition.

8.4 Radiometric Specifications for APEX

8.4.1 Introduction

Radiometric specifications for an airborne imaging spectrometer rely on different measures and requirements. These are mainly derived from user's requests to meet their application, reaching from measuring water leaving radiance of eutrophic lakes to top-of-the-cloud BRDF measurements.

In a first step, the modeling process will focus on the total radiometric dynamic range based upon the expected operating range of the imaging spectrometer, its operating altitude, and the requested applications. The major driving factors for the radiometric performance are the expected lowest and highest radiance levels before noise and saturation. The operation range in addition defines the expected position in azimuth and zenith of the sun relative to the sensor depending on geographical extent. The flying altitude of the instrument affects the amount of path scattered radiance.

The modeled at-sensor-radiances will include three definitions: The expected minimum radiance present at the foreoptics, the maximum radiance just before the saturation level is reached, and finally the validation radiance, using a constant albedo of 0.4 over the whole wavelength range covered. The validation radiance is used to compute the mean SNR over all detector channels to be compliant with the final SNR specifications.

8.4.2 Specifications

The initial specifications for APEX are listed in Table 8.2.

Instrument	Specification	Remarks
Spectral range	450–2500 nm	Including absorption bands
Spectral bands	> 200	Electronically selectable
Sampling interval	< 15 nm	VIS/NIR 2.5 nm SWIR 8 nm
Spectral sampling width	< 1.5 Sampling interval	
Spectral misregistration	< 0.15 Sampling interval	
FOV	$\pm 14^\circ$ (28° total)	Across track
IFOV	0.5 mrad	
Swath width	3.7 km	at 7.5 km altitude
GIFOV	7.5 m	at 7.5 km altitude
S/N	average = 100	For each channel, including absorption bands
Pixels across track	≤ 1000	

Table 8.2: Initial APEX specifications [28].

8.5 Radiometric Modelling of At-Sensor-Radiances

8.5.1 PRISM Specifications

The radiometric specifications defined for the PRISM instrument include the definitions for minimum, typical, and maximum spectral radiances as well as the NEAR for a given set of spectral channels. The wavelength ranges in the water vapor absorption bands are omitted and the resulting gaps are between 1120–1150 nm, 1410–1480 nm, and 1800–2010 nm. The wavelength range between 1320–1400 nm has been included in the specifications because of possible applications requiring water vapour [55][69][70].

The three levels that have been defined are a maximum, typical, and minimum level. The maximum is defined assuming a 110% reflecting target on ground. The typical level is chosen according to a typical land surface with reflectances $\rho = 0.2$, $450 \leq \lambda < 600$ nm; $\rho = 0.4$, $600 \leq \lambda < 1900$ nm; and $\rho = 0.2$, $1900 \leq \lambda < 2350$ nm. Finally, the minimum level is defined using a typical dark land scene, wet mud. This spectrum has a linear increasing reflectance from 2–7% between 450–1850 nm and a constant reflectance of 7% for $\lambda \geq 1850$ nm. The model input parameters for PRISM are listed in Table 4 on page 134, and

are visualized in Figure 8.3.

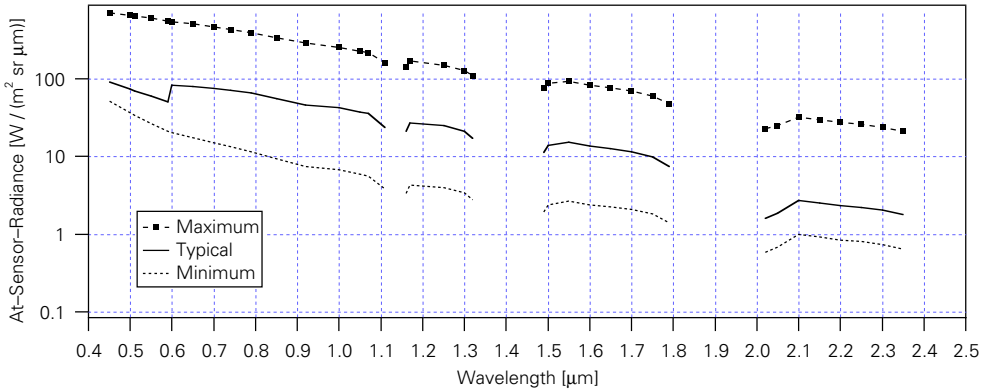


Figure 8.3: PRISM radiometric specifications for minimum, typical and maximum at-sensor-radiances (solid dots indicate modeling points) [55].

8.5.2 Selection of Radiative Transfer Code and Model Comparison

Two fully automated RTC’s for calculation of the atmospheric properties are available for this pretest. MODTRAN [6][48] (MODTRAN3.5, version 1.1) is used, updated to run with unlimited spectral bands as reference background and a graphical user interface [94], and 6S [115] (version 4.1) is used, updated to accept any response function from a given set of parameter [92].

The comparison of both models is performed using the three levels defined as minimum, validation, and maximum. The differences in functionality and the treatment of atmospheric parameters of these two models are discussed in Schläpfer [95].

The spectral response function used for 6S is adopted to the spectral resolution of MODTRAN. The 6S runs are performed using a constant filter function of one (i.e. a rectangular filter) with the same FWHM as in the MODTRAN model. The most obvious differences between the two models can be seen in the blue region of the spectrum, where the spectral resolution of the 6S model is coarser than MODTRAN resulting in fewer different values calculated and differences within the major water vapour absorption bands. The basis for the model input for the 6S and MODTRAN comparison are the radiance levels defined for APEX discussed in the following chapter. The results are plotted for the whole spectral wavelength range of APEX between 0.4 and 2.5 μm. Based on these results, MODTRAN is preferred to model the at-sensor-radiances because of its finer spectral resolution. 6S would be a favorite if BRDF modeling must be considered. The sensor’s performance evaluation is done without the consideration of the BRDF. The 920 bands calculated for each level of the modeling process on a UNIX based workstation (see section b) on page 133) took 35 min. for a complete 6S run and 8 min. for a complete MODTRAN run. The model comparison

is given in Figure 8.4 and Figure 8.5, where the latter is a zoom into the wavelength range between 1900–2500 nm for the validation level only.

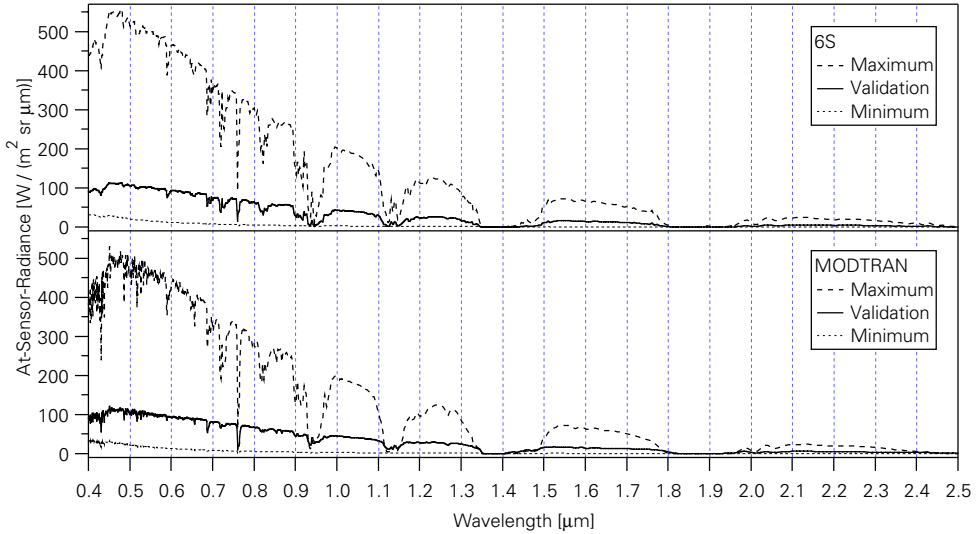


Figure 8.4: Comparison of 6S and MODTRAN radiative transfer codes using equivalent input parameters.

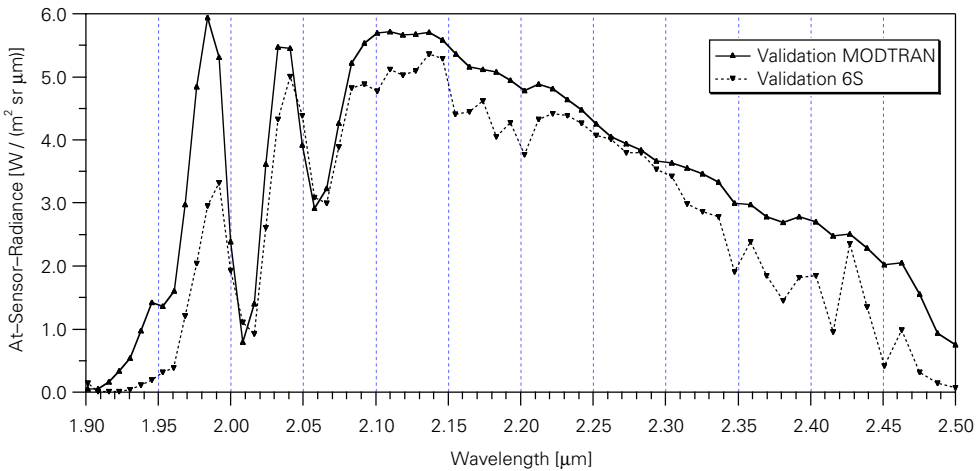


Figure 8.5: Differences between 6S and MODTRAN in the 1.9–2.5 μm region using the same atmospheric conditions and a constant albedo of 0.4.

8.5.3 Input Parameters for the APEX Model

The modeling of the APEX specifications is based on MODTRAN at-sensor-radiances. Three different situations are modeled using an albedo of 1 as the *maximum* level to determine the detector saturation, a constant albedo of 0.4 is cho-

sen as the SNR *validation* level and a 0.01 albedo as the *minimum* level.

The maximum level, using the model parameter listed in Table 3 on page 134, is suited to measure very high reflecting targets, such as snow or high reflecting artificial objects. The maximum level will most probably saturate over clouds, hot spot situations, and glitter resulting from reflections on the water surface (see Figure 8.6). Applications related to these saturation problems (e.g. top-of-the-cloud BRDF measurements) are explicitly excluded from the range of applications foreseen for APEX. An update to include these applications would require a remodelling process including an albedo of 1.1 over clouds at altitudes up to the sensor's operating altitude.

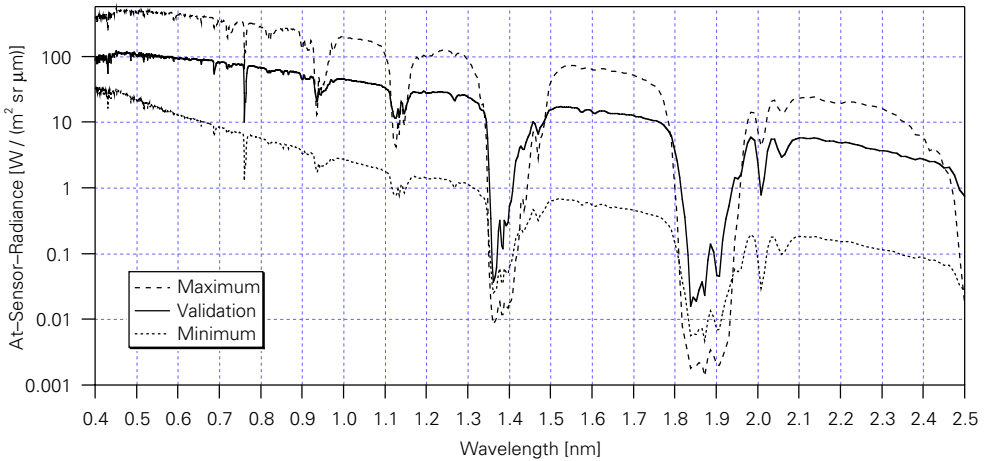


Figure 8.6: APEX radiometric specifications for minimum, validation and maximum at-sensor-radiances.

The validation level is used to verify the SNR specifications. The requirements for SNR are defined as ≥ 100 of the average SNR over all channels covered by one detector (e.g. VIS or SWIR), including the band positions in the water vapour absorption bands. Atmospheric applications and accurate atmospheric corrections are an important goal of APEX and therefore the specifications include all band positions inside the absorption bands.

The minimum level is defined as 0.01 albedo. This is at the same time the expected uncertainty of the RTC. Any research for albedos < 0.01 would mainly reflect the path scattered radiance without any significant information in the signal itself. Inland water monitoring is an application requiring such low ground albedos. Therefore the lower end of the dynamic range is defined by this 0.01 albedo.

The comparison of the radiometric dynamic range defined for both instruments shows a good agreement for the validation (APEX) and typical (PRISM), in the range where the albedo is the same (0.4, 600–1900 nm, see Figure 8.7). The APEX minimum level is as expected generally lower as the PRISM minimum level due to different approaches defining this albedo.

The comparison of the maximum levels of both instruments (e.g. APEX and PRISM) incorporates a much higher difference due to fact that top-of-the-cloud measurements for APEX are excluded while defining this level.

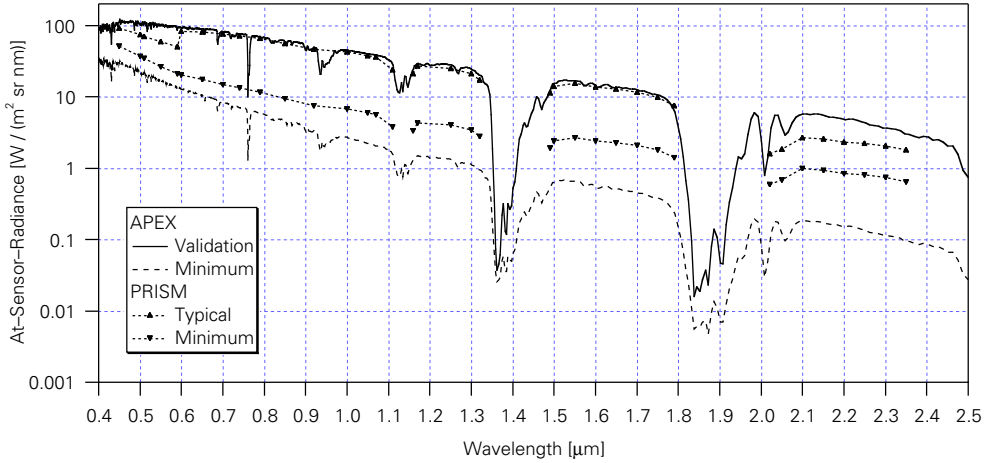


Figure 8.7: Comparison of PRISM [55] and APEX radiometric specifications at the typical, validation and minimum levels.

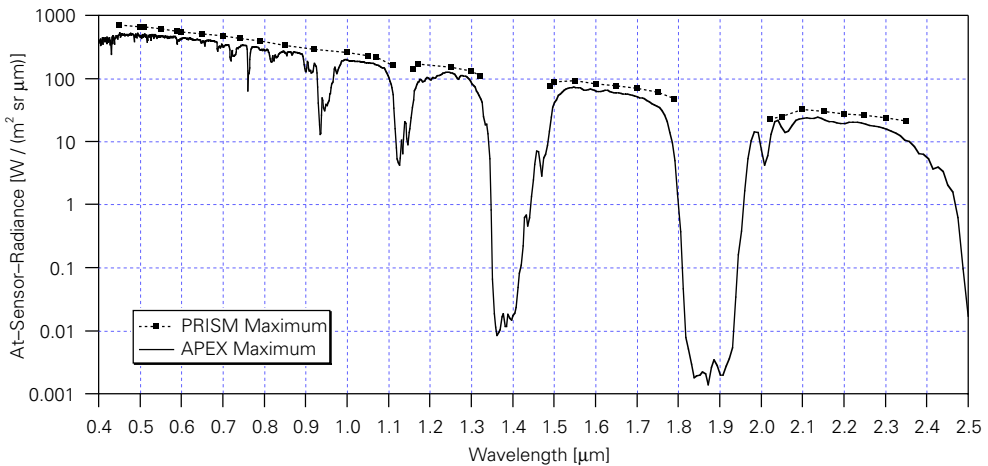


Figure 8.8: Comparison of PRISM [55] and APEX radiometric specifications at the maximum level.

8.6 Determination of SNR and $NE_{\Delta\rho}$ for APEX

A major figure of interest in the expected performance of an airborne imaging spectrometer is the signal-to-noise ratio and the noise equivalent reflectance dif-

ference. The SNR is defined as the ratio between signal and noise electrons recorded by the detector. Based on the input parameter given (see Appendix, Table 5 on page 135), the signal is calculated using the following relation [28][73][75]:

$$S = e_s = A_e \cdot \omega \cdot \tau \cdot \int_{\lambda_1}^{\lambda_2} \eta(\lambda) \cdot \tau_0(\lambda) \cdot \frac{\lambda}{hc} \cdot L(\lambda) \cdot d\lambda \quad (8.1)$$

where

e_s	Total number of electrons arriving at one detector element (signal)
A_e	Area of the entrance aperture
τ	Pixel integration time (dwell time)
ω	Solid angle of the GIFOV
λ_1, λ_2	Spectral bands
$\eta(\lambda)$	Quantum efficiency, or the ratio of the number of countable output events to the number of incident photons (e.g. photoelectrons per photon)
$\tau_0(\lambda)$	Optical transmittance
h	Planck's constant
c	Speed of light
$L(\lambda)$	Radiance (obtained from MODTRAN)
λ	Wavelength of the simulated channel.

This allows the determination of the total number of electrons arriving per detector pixel based on the modeled at-sensor-radiance using MODTRAN. The final estimation of the noise is calculated using the manufacturer information of the detector and the electronic noise parameters:

$$N = e_n = \sqrt{(N_i)^2 + (N_s)^2} \quad (8.2)$$

where

e_n	Total number of electrons determining the noise
N_i	Residual noise electrons (gain, quantization, A/D converter, dark current, etc.)
N_s	Shot noise electrons.

The SNR can be derived using the total number of electrons divided by the noise-contributing electrons:

$$SNR = \frac{e_s}{e_n} \quad (8.3)$$

The model input parameter used for this calculation are listed in Table 5 on page 135 in the Appendix. The initial specification requires a SNR of ≥ 100 for the average of all channels for each detector. In this case the SNR can be listed as (see Table 8.3 and Figure 8.9):

Detector	SNR(Max)	SNR(Val)	SNR(Min)
Si (VIS)	974	226	30
HgCdTe (SWIR)	1322	414	19

Table 8.3: Average SNR for each detector and level.

The calculation of $NE\Delta\rho$ is based on the formula (modified after [51]):

$$NE\Delta\rho = \frac{4 \cdot \sqrt{\pi} \cdot \frac{f}{d_A} \cdot \sqrt{\frac{v}{h}}}{(\theta_f)^2 \cdot d_A \cdot \int_{\lambda_1}^{\lambda_2} E(\lambda) \cdot \tau_0(\lambda) \cdot D^*(\lambda) \cdot d\lambda}, \quad (8.4)$$

or can be rewritten in a simpler form as:

$$NE\Delta\rho = \frac{\rho}{SNR} \quad (8.5)$$

where

$NE\Delta\rho$ Noise equivalent reflectance difference

f Focal length

d_A Aperture diameter

v Aircraft speed

h Aircraft altitude (above ground)

θ_f IFOV

$D^*(\lambda)$ Detectivity

$E(\lambda)$ Incident radiant power per projected area of a surface.

Based on eq. (8.5), the noise equivalent reflectance difference for each channel can be plotted and again, the averages for all the levels are also calculated and given as (see Table 8.4 and Figure 8.10):

Detector	$NE\Delta\rho$ (Max)	$NE\Delta\rho$ (Val)	$NE\Delta\rho$ (Min)
Si (VIS)	0.24%	0.36%	0.11%
HgCdTe (SWIR)	24.92%	0.71%	0.13%

Table 8.4: Average $NE\Delta\rho$ for each Detector and Level

The electronics support a 12 bit (or $Q = 4096$) quantization rate. The resulting digital numbers in the final image are dependent on saturation level and electronic gain used [74]:

$$DN = G_e \cdot \frac{S}{S_{sat}} \cdot Q - 1 \quad (8.6)$$

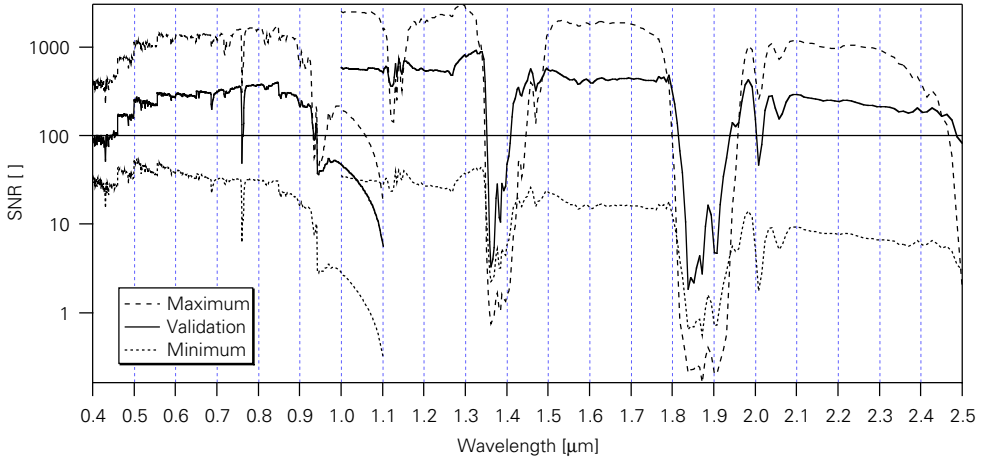


Figure 8.9: SNR for all APEX channels for the maximum, validation and minimum levels.

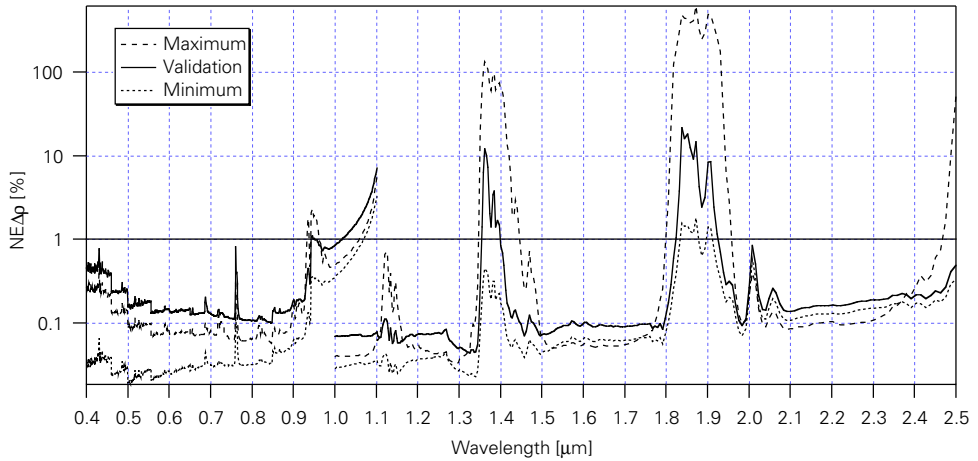


Figure 8.10: $NE\Delta\rho$ for each APEX channel.

where

- DN Digital number (or gray levels)
- G_e Electronic gain
- S_{sat} Detector saturation electrons
- Q Quantization levels.

Finally, the MTF is included in the determination of the usable digital numbers using the following equation:

$$\bar{D}_j = G_e \cdot \frac{S_i + (S_j - S_i) \cdot MTF(v)}{S_{sat}} \cdot Q - 1 \tag{8.7}$$

where

- \bar{D}_j Digital numbers including the MTF
- i, j Adjacent pixel positions (having a 5% different signal)
- $MTF(\nu)$ Modulation transfer function defined using the spatial frequency.

The MTF can be approximated for expected performance limits for a polychromatic lens system by ([5], p. 1.41):

$$MTF(\nu) \approx e^{-2(\pi\sigma\nu)^2} \quad (8.8)$$

where

- ν Spatial frequency ($\nu = 1/f\lambda$)
- σ Standard deviation of the irradiance distribution (set to 1).

Using eqs. (8.7) and (8.8), for each channel the digital numbers (or gray levels) can be plotted (see Figure 8.11). The electronic gain is adjusted, so that the VIS and SWIR detector saturate only slightly ($G_e(VIS) = 1, G_e(SWIR) = 0.14$).

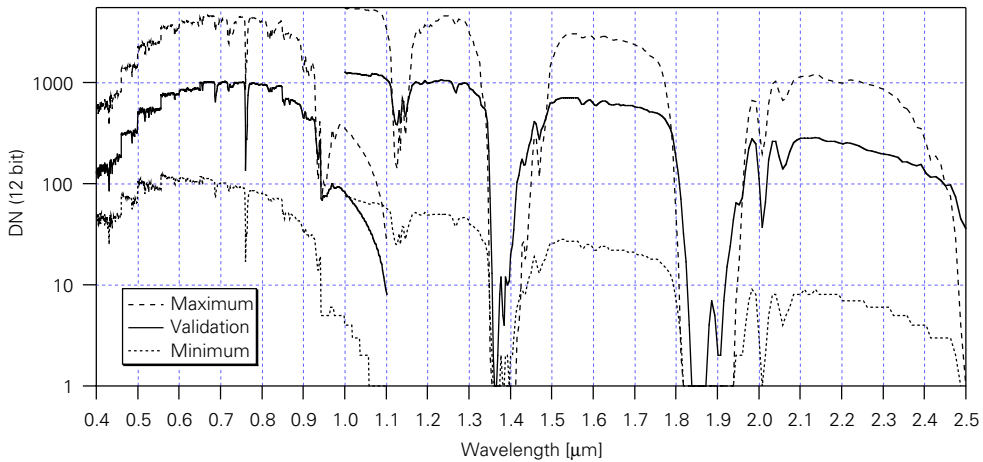


Figure 8.11: Digital numbers (or grey levels) for the three specified radiance levels.

8.7 Conclusions

The presented sensor model is capable of deriving figures of merit for APEX. The basis for the performance determination is the definition of the three levels: maximum, validation, and minimum. The maximum level determines the saturation of the system and is in compliance with the PRISM specifications given the restrictions on certain applications. The minimum level verifies whether applications dealing with very low energies such as water leaving radiances are still within the scope of APEX. Dealing with a SNR around 20–30 for the lowest signal is acceptable given the narrow bandwidth of the APEX sensor. The validation level

is a more or less an artificial construct to determine a testbed for the acceptance tests with a predefined figure of merit (e.g. SNR). The APEX sensor defined after this model may be capable to model all the reflective channels of PRISM and therefore is best suited as a precursor instrument as well as a vicarious calibration instrument during the operational phase of PRISM.

Chapter 9:

Conclusions and Outlook

9.1 Conclusions

It has been the goal of this work to add ground spectroradiometric measurement uncertainties to the modeling process and so contributing to the application and geophysical algorithm development in imaging spectroscopy.

Calibration as an integral part of the operation of any remote sensing system is a must if the goal is to derive absolute quantities from spectroscopic measurements. The calibration effort is determined by the desired calibration uncertainty and is therefore dependent on the user requirements and the planned application of the data. Uncertainties of up to 10% are tolerable while collecting field reflectance measurements. Spectral libraries most often represent the natural variability of such collection efforts, and therefore are representative for their specific application. But if the measurements are used for a vicarious calibration experiment of an imaging spectrometer, uncertainties below 1% of the ground based measurements are required. Both cases nevertheless require an accurate characterization of the specific measurement equipment used.

A calibration procedure aiming for a $\leq 1\%$ calibration uncertainty is much more expensive and requires the use of laboratory standards that are in many cases too expensive to support and maintain in light of the overall instrumentation costs. Sometimes this calibration accuracy requires the simultaneous measurement of many parameters in order to prevent the measurement of drift over time, or ageing of calibration parameters. The required calibration accuracy has also an additional impact on the recalibration frequency. Permanent monitoring of possible drifts of calibration parameters is necessary to allow their extrapolation from the laboratory to the operating environment.

Many problems can be relaxed while aiming at a 10% calibration accuracy. Given the example of the temperature dependency of the PbS detectors, it has not been investigated if the temperature difference also causes a shift of center wavelengths inside the instrument, thereby requiring a simultaneous calibration of temperature dependence of the signal and center wavelengths. Such a complex characterization procedure is definitely required if the calibration accuracy must be in the magnitude of 1% or less.

The discussion of the limitations associated with a calibration always starts at one point: calibration will never be able to substitute or compensate for a poor system performance or design. Calibration is the process of introducing the possible sources of errors and defining the uncertainties associated with the measurement instrument. It never suffices to calibrate an instrument in the laboratory using the current environment temperature and operating the instrument under a different pressure and temperature regime, hoping to be able to extrapolate the calibration parameters accordingly. It is therefore a promising approach to define the associated uncertainties and pass these measurements on to the next modeling step with a defined level of confidence. Unfortunately, this calibration step for ground spectroradiometric equipment has been neglected and underestimated in remote sensing.

In-flight calibration means for airborne and spaceborne imaging spectrometers are the best way to establish a comparison basis with ground based measurements. Vicarious calibration experiments support both the calibration parameter drift analysis and even the updating of existing calibration parameters. Other approaches such as adapting the laboratory environment to the operating environment (or vice versa) of the investigated sensor are also promising.

The proper selection of well suited calibration targets for airborne systems remains critical in a Mid-European environment. Approaches using human-made, artificial targets that are easily deployable might support the search for the ultimate calibration target.

9.2 Outlook

As technology advances, ground-based spectroradiometers will increasingly incorporate better and more advanced technologies. The potential of imaging spectroscopy is not only limited to the reliable measurement of information located in wavelength ranges with a high signal to noise ratio. Future instruments will significantly contribute to measurements within spectral regions having larger uncertainties and lower atmospheric transmittance, such as the water vapor absorption bands.

From a technological point of view, it has been argued in imaging spectroscopy that data dimensionality reduction is based on correlation of adjacent bands. The reason for this is understandable since most of the data analysis relies on one central figure of merit, the SNR. With upcoming new technologies, ground-based spectroradiometers as well as imaging spectrometers will have better performances and therefore make better use of all the channels they initially are equipped with.

In addition, calibration procedures must be viewed as an integral part of any airborne or spaceborne earth observation project. Recent advances in sensor technology development demonstrate that calibration is generally accepted as a high priority part of the system. Most of the upcoming systems, whether airborne or

spaceborne, therefore have a well defined calibration strategy (e.g. APEX [44], ENVISAT (MERIS) [30], MODIS [57], etc.).

The combination of well calibrated ground equipment, a sampling strategy adapted to the specific task, radiative transfer codes and sensor models, all associated with a predefined uncertainty, will help to better identify applications and their contribution in imaging spectroscopy. The total contribution of measurement uncertainties associated with ground measurements being used as reference input for sensor models and validation purposes has been neglected in many applications so far.

Glossary

Variables and constants are listed in order of their appearance in the thesis. Once defined, they are not listed a second time. The definition of the terms used are derived from Bass [4][5], Colwell et al. [17], Deschamps et al. [26], and Schowengerdt [98].

a) Chapter 2

R	Responsivity	[-]
S	Output signal	[DN]
Φ	Radiant power, flux	[W]

b) Chapter 4

L	Radiance	$[W/(m^2 \cdot sr)]$
L_λ	Spectral radiance	$[W/(m^2 \cdot sr \cdot nm)]$
λ	Wavelength	[nm]
A	Area (entrance aperture)	$[m^2]$
σ	Standard deviation	[-]
τ	Integration time (of a spectroradiometer)	[s]
NES	Noise equivalent signal	[DN]
NER	Noise equivalent radiance	$[W/(m^2 \cdot sr \cdot nm)]$
C_{gain}	Calibration gain	$[W/(m^2 \cdot sr \cdot nm \cdot DN)]$
k_n	Fit parameters	[-]
λ_{FWHM}	Full width at half maximum	[nm]
K_{ab}	Nonlinearity correction factor	[-]
$i_a, i_b, i_{(a+b)}$	Individual and combined sources	[DN]
θ_f	Field-of-View	[rad]
f	Focal length	[mm]
r_d	Detector radius	[mm]
r_t	Spot radius of the target	[cm]
h	Measurement altitude	[m]
ω	Solid angle defined by the FOV	[sr]
d_t	Target diameter	[m]
A_t	Target area	$[m^2]$
A_a	Area of the lens	$[m^2]$
P_n	Polarizer states	[DN]
m_{ij}	ij 'th element of the Mueller matrix	[-]

s_i	s 'th element of the Stokes vector	[-]
T	Temperature	[K]
c) Chapter 5		
$\rho(\lambda)$	Spectral reflectance factor	[%]
$\Phi_{\lambda r}$	Reflected spectral radiant flux	[W]
$\Phi_{\lambda i}$	Incident spectral radiant flux	[W]
$\rho(\lambda)_{corr}$	Spectral reflectance (non-lambertian)	[%]
$\rho_{\lambda s}$	Spectral reflectance factor of the field reference	[%]
d) Chapter 6		
$u_c^2(y)$	Estimated variance	[-]
k	Coverage factor	[-]
y	Measurement result	[-]
Y	Measurand	[-]
$y_{max}; y_{min}$	Upper and lower limits of measurement	[-]
$u_i(y)$	i 'th standard uncertainty	[-]
ν_i	Degrees of freedom	[-]
n	Data points measured	[-]
m	Parameters estimated	[-]
U	Expanded uncertainty (high level)	[%]
U_p	Expanded uncertainty (specified level)	[%]
e) Chapter 7		
L_λ	Calibrated at-sensor-radiance	[W/(m ² · sr · nm)]
C_{gain}	Calibration gain	[W/(m ² · sr · nm · DN)]
C_{offset}	Calibration offset	[W/(m ² · sr · nm)]
$L_{\lambda, T}$	Temperature calibrated radiance	[W/(m ² · sr · nm)]
k_n	Temperature model fit parameters	[-]
T_{PbS}	Temperature reading of the PbS1 detector	[K]
f) Chapter 8		
e_s	Total number of electrons	[e]
A_e	Area of the entrance aperture	[m ²]
$\eta(\lambda)$	Quantum efficiency	[%]
$\tau_0(\lambda)$	Optical transmittance	[%]
h	Planck's constant	[Js]
c	Speed of light	[m/s]
N_i	Residual noise electrons	[e]
N_s	Shot noise electrons	[e]
$NE\Delta\rho$	Noise equivalent reflectance difference	[%]
d_A	Aperture diameter	[mm]

Glossary

v	Aircraft speed	[m/s]
h	Aircraft altitude (above ground)	[m]
D^*	Detectivity	[($m \cdot \sqrt{Hz}$)/ W]
DN	Digital number (or gray levels)	[DN]
G_e	Electronic gain	[-]
S_{sat}	Detector saturation electrons	[e]
Q	Quantization level	[bit]
\bar{D}_j	Digital numbers including the MTF	[-]
i, j	Adjacent pixel positions	[-]
MTF	Modulation transfer function	[$cycles/mm$]
v	Spatial frequency	[$cycles/mm$]

Appendix

a) Acronyms

GS	Second Simulation of the Satellite Signal in the Solar Spectrum
A/D	Analog—Digital converter
APEX	Airborne PRISM Experiment
ASD	Analytical Spectral Devices, Inc.
ATO	Ambient Temperature Operation
AVIRIS	Airborne Visible/Infrared Imaging Spectrometer
BaSO ₄	Barium Sulfate
BRDF	Bidirectional Reflectance Distribution Function
BRF	Bidirectional Reflectance Factor
CASI	Compact Airborne Spectrographic Imager
CCD	Charge Coupled Device
CCRS	Canada Center for Remote Sensing
CIPM	Comité International des Poids et Mesures
D*	Detectivity (of a detector)
DAIS (7915)	Digital Airborne Imaging Spectrometer (7915)
DLR	Deutsches Luft- und Raumfahrtzentrum
DN	Digital Numbers
DOCP	Degree of Circular Polarization
DOLP	Degree of Linear Polarization
DOP	Degree of Polarization
DC	Direct Current
EGO	European Goniometer Facility
ENVI	Environment for Visualizing Images (RSI Inc.)
ENVISAT	ESA Envisat-1 satellite
ESA	European Space Agency
FEE	Front End Electronics
FEL	Spectral Irradiance Calibration Standard
fL	Footlambert (Luminance, 1 fL = 3.426 nit = 3.426 cd/m ²)
FIGOS	Field Goniometer System
FOV	Filed of View
FWHM	Full Width at Half the Maximum
GER	Geophysical and Environmental Research Corp.
GER3700	GER 704 channel portable spectroradiometer (SN# 3700-1002)
GIFOV	Ground Instantaneous Field of View

GMT	Greenwich Mean Time
GPS	Global Positioning System
HYDICE	Hyperspectral Digital Imagery Collection Experiment
IDL	Interactive Data Language (RSI Inc.)
IR	Infrared
IFOV	Instantaneous Field of View
JPL	Jet Propulsion Laboratory
Laser	Light Amplification by Stimulated Emission of Radiation
LSPIM	Land Surface Processes and Interactions Mission
MISR	Multi–Angle Imaging Spectroradiometer
MODIS	Moderate Resolution Imaging Spectrometer
MODTRAN	Moderate Resolution Model for LOWTRAN7
MTF	Modulation Transfer Function
NASA	National Aeronautics and Space Administration
NER	Noise Equivalent Radiance
NE $\Delta\rho$	Noise Equivalent Reflectance Difference
NES	Noise Equivalent Signal
NIR	Near–infrared part of the electromagnetic spectrum
NIST	National Institute of Standards and Technology
NSR	Noise to Signal Ratio
PbS	Lead Sulfide
PbS1	First Lead Sulfide detector of the GER3700 (128 channels)
PbS2	Second Lead Sulfide detector of the GER3700 (64 channels)
PCI	PCI Geomatics Inc.
PDL	Polarization Dependent Loss
PRISM	Process Research by an Imaging Space Mission
PROM	Programmable Read Only Memory
PSF	Point Spread Function
PTFE	Polytetrafluoroethylene
RSI	Research Systems Inc.
RSL	Remote Sensing Laboratories
RSS	Root–Sum–Squares law (law of propagation of uncertainties)
RTC	Radiative Transfer Code
SENSAT	Sensor–Atmosphere–Target Model
SI	Système International (d’Unités)
Si	Silicium
SNR	Signal to Noise Ratio
SVAT	Soil–Vegetation–Atmosphere–Transfer
SWIR	Short–Wave Infrared part of the electromagnetic spectrum
US	United States (of America)
UV	Ultraviolet
VIS	Visible part of the electromagnetic spectrum

b) Hard- and Software

This work is completed using mainly a Sun Sparc workstation (SUN Ultra 2, 2 x 200 Mhz CPU's, 45 GByte SCSI storage array, 512 MByte RAM, Creator 3D Z-buffered graphic plane) running under Sun Solaris 2.5.1 operating system, and an Apple Macintosh computer (Apple PowerMac 7600, 132 Mhz PPC, 2 GByte disk, 48 MByte RAM), running under MacOS 8.1. The software used for the scientific part is RSI IDL 5.0.3 (<http://www.rsinc.com>), RSI ENVI 3.0 (<http://www.envi-sw.com>), PCI Easi/Pace 6.2 (<http://www.pcigeomatics.com>), the GNU C compiler (<http://www.fsf.org>), and Wavemetrics Igor Pro 3.12 (<http://www.wavemetrics.com>).

Typesetting is done on a Apple Macintosh Powerbook 1400c, using Adobe FrameMaker 5.5.3 (<http://www.adobe.com>) using Adobe Garamond and Univers family typefaces. Graphics are all produced using the abovementioned software (and stored as Tagged Image File Format (TIFF) or Encapsulated Postscript (EPS)), annotations are added using Adobe Photoshop 4.0 (<http://www.adobe.com>) and Daneba Canvas 5.0.3 (<http://www.daneba.com>).

c) Vicarious Calibration Experiment

Spectrometer	No. of Bands	Detector	Wavelength Range	Spectral Resolution
VIS/NIR	32	Si	450–1050 nm	15–30 nm
SWIR I	8	InSb	1500–1800 nm	45 nm
SWIR II	32	InSb	1900–2500 nm	35 nm
MIR	1	MCT	3.0–5.0 μm	2 μm
THERMAL	6	MCT	8.7–12.3 μm	0.9 μm

Table A.1: DAIS characteristics (radiometric).

Parameter	Quantity
IFOV	3.3 mrad
Swath angle	52° ($\pm 26^\circ$, aircraft limited)
Pixels per line	512
Quantization	15 bit
Lines per scene	approx. 2700
Operating altitude	Flight level 120 (3600 m a.s.l.)

Table A.2: DAIS characteristics (spatial).

d) APEX At-Sensor-Radiance Model Parameter

Model Parameter	Maximum	Validation	Minimum
Atmosphere	Tropical	Subarctic Winter	Subarctic Winter
Mode	Radiance	Radiance	Radiance
Scattering	Multiple	Multiple	Multiple
Temperature Boundary	293.15° K	293.15° K	293.15° K
Ground Albedo	1.0	0.4	0.01
Rural Extinction, Visibility	23 km	23 km	23 km
Background	Normal Volcanic	Normal Volcanic	Normal Volcanic
Clouds	none	none	none
Aircraft Altitude	7.5 km	7.5 km	7.5 km
Zenith Angle	180°	180°	180°
Observer Lat.	0°	60° N	60° N
Observer Lon.	0°	0°	0°
Day of Year	182	82	82
Time	11:20 GMT	11:20 GMT	11:20 GMT

Table A.3: APEX atmospheric model input parameter.

Model Parameter	Maximum	Validation	Minimum
Atmosphere	Tropical	Subarctic Winter	Subarctic Winter
Ground Albedo	1.1	0.2 / 0.4 / 0.2	0.02 – 0.07
Continental aerosols, Visibility	23 km	23 km	23 km
Satellite Altitude	800 km	800 km	800 km
Zenith Angle	-30 to + 30 deg	-30 to + 30 deg	-30 to + 30 deg
Observer Lat.	0°	60° N	60° N
Day of Year	182	82	82
Time	11:20 GMT	11:00 GMT	11:00 GMT
Spectral resolution	10 nm	10 nm	10 nm

Table A.4: PRISM atmospheric model input parameter.

Parameter	Quantity
Spectral range	450–2500 nm
Spectral resolution	10 nm
FOV	28°
IFOV	0.5 mrad
f#	2
Focal length	40 mm
Aperture diameter	10 mm
Entrance aperture	7.85E-05 m ²
Reflectivity of optical surfaces	1%
Optical transmission	variable (15–40%, 70%)
Pixel size VIS	20 μm
Pixel size SWIR	20 μm
Spatial pixels VIS	1000
Spatial pixels SWIR	1000
Spectral pixels VIS	200
Spectral pixels SWIR	200
Quantum efficiency VIS	variable, 15–40%
Quantum efficiency SWIR	70%
Flight altitude	7500 m
Aircraft speed	90 m/s
Swath width	3739.9 m
GIFOV	3.74 m
Integration time	0.04155 s
Scanning frequency	24.06 Hz
Solid angle	2.49E-07 sr
Saturation VIS	2'000'000e
Saturation SWIR	670'000e
Dark current VIS	56e
Dark current SWIR	66e
Electronic noise	531e
Quantization level	12bit
Albedo	variable (1, 0.4, 0.01%)

Table A.5: APEX sensor model input parameter.

References

- [1] Arecci A.V., Illuminance from Uniform Lambertian Sources, in: *Labsphere catalog*, North Sutton, NH, pp. 146–148, 1994
- [2] Bahrenberg G., and E. Giese, *Statistische Methoden und ihre Anwendung in der Geographie*, Teubner, Stuttgart, pp. 308, 1975
- [3] Basedow R.W., D.C. Carmer, and M.E. Anderson, HYDICE System, Implementation and Performance, *Proc. SPIE*, 2480:258–267, 1995
- [4] Bass M. ed., *Handbook of Optics: Fundamentals, Techniques, and Design*, Optical Society of America, Vol. I, 2nd ed., McGraw–Hill Inc., New York, 1995
- [5] Bass, M. ed., *Handbook of Optics: Devices, Measurement, and Properties*, Optical Society of America, Vol. II, 2nd ed., McGraw–Hill Inc., New York, 1995
- [6] Berk A., L.S. Bernstein, and D.C. Robertson, *MODTRAN: A Moderate Resolution Model for LOWTRAN7*, Report GL–TR–89–0122, Geophysics Lab., pp. 38, Bedford, USA, 1989
- [7] Bruegge C.J., A.E. Stiegman, D.R. Coulter, and A.W. Springsteen, Reflectance Stability Analysis of Spectralon Diffuse Calibration Panels, *Proc. SPIE*, 1493:132–142, 1991
- [8] Cathomen C., Nachbarschaftseffekte und Bildspektrometrie, Master Thesis, Dept. of Geography, University of Zürich, unpublished, pp. 122, 1997
- [9] Chang, S.H., M.J. Westfield, F. Lehmann, D. Oertel, and R. Richter, 79–Channel Airborne Imaging Spectrometer, *Proc. SPIE*, 1937:164–172, 1993
- [10] Chen H.S., *Remote Sensing Calibration Systems: An Introduction*, Deepak Publishing, Hampton, pp. 238, 1997
- [11] Chipman, R.A., Polarimetry, in: *Handbook of Optics*, ed. M. Bass, Vol. II, 2nd ed., McGraw–Hill Inc., New York, pp. 22.1–22.37, 1995
- [12] Chrien T.G., and T. Rubin, Calibration and Validation of Imaging Spectrometer Data, ERIM, 2nd Conference on Airborne Remote Sensing, Workshop Notes, San Francisco, 1996
- [13] Chrien T., R.O. Green, C. Chovit, M.L. Eastwood, and C. Sarture, Calibration of the Airborne Visible/Infrared Imaging Spectrometer in the Laboratory, *JPL Publication*, 96–4(1):39–48, 1996
- [14] CIPM, *BIPM Proc.–Verb. Com. Int. Poids et Mesures*, 54:14, pp. 35, 1986
- [15] Clark R.N., G.A. Swayze, A.J. Gallagher, T.V. King, and W.M. Calvin, The U.S. Geological Survey, Digital Spectral Library: Version 1: 0.2 to 3.0 mm, U.S. Geological Survey, Open File Report 93–592, Denver, pp. 1326, 1993.
- [16] Coherent, CR–699 Ring Dye Laser, Coherent Laser Product Division, Chap. 2, Palo Alto, CA, p. 1–25, 1977
- [17] Colwell R.N., and D.S. Simonett, *Manual of Remote Sensing Volume 1: Theory*,

- Instruments, and Techniques*, Am. Soc. of Phot., Virginia, 1983
- [18] Congalton R.G., A Comparison of Sampling Schemes Used in Generating Error Matrices for Assessing the Accuracy of Maps Generated from Remotely Sensed Data, *Phot. Eng. and Rem. Sens.*, 54(5):593–600, 1988
- [19] Corl T., Personal Communication, GER, Millbrook, NY, 1993–1998
- [20] Cosnefroy H., M. Leroy, and X. Briottet, Selection and Characterization of Saharan and Arabian Desert Sites for the Calibration of Optical Satellite Sensors, *Rem. Sens. Env.*, 58:101–114, 1996
- [21] Curran P.J., Polarized Visible Light as an Aid to Vegetation Classification, *Rem. Sens. Env.*, 12:491–499, 1982
- [22] Curtiss B., A.F.H. Goetz, Field Spectrometry: Techniques and Instrumentation, *Proc. of ISSSR*, 1995
- [23] Dangel S., P. Eschle, B. Röhrich, U. Rusch, H. Schmid, and R. Holzner, Dynamics of Laser Beam Switching in Sodium Vapor, *J. Opt. Soc. Am. B*, 12:681–686, 1995
- [24] Del Bello U., Statement of Work for the Definition of an Airborne Imaging Spectrometer, ESA JP/95.10.440/UDB, Noordwijk, pp. 9, 1995
- [25] Del Bello U., R. Meynart, Hyperspectral Imager for the Future ESA Land Surface Processes Earth Explorer Mission, *Proc. SPIE*, 2957, 1996
- [26] Deschamps P.Y., M. Hermann, and D. Tanre, Definitions of Atmospheric Radiance and Transmittances in Remote Sensing, *Rem. Sens. Env.*, 13:89–92, 1983
- [27] Dickerhof C., Geologische Analyse von Bildspektrometriedaten in Naxos, Master Thesis, Dept. of Geography, University of Zürich, unpublished, 1998
- [28] DSS–OIP, IMEC, VITO, RSL, OC, and CIR, *APEX – Final Report*, ESA 11848/96/NL/CN, Noordwijk, pp. 158, 1997
- [29] Duggin M.J., The Field Measurement of Reflectance Factors, *Phot. Eng. and Rem. Sens.*, 46(5):643–647, 1980
- [30] ESA, *ENVISAT–1*, <<http://envisat.estec.esa.nl/>>, 1997
- [31] ESA–ESAC, The Evaluation of the Nine Candidate Earth Explorer Missions–The Report of the Earth Science Advisory Committee, <http://www.estec.esa.nl/vrwww/explorer/EXPLORER_ESAC_report.html>, 1996
- [32] Flasse S.P., M.M. Verstraete, B. Pinty, and C.J. Bruegge, Modeling Spectralon’s Bidirectional Reflectance for In–Flight Calibration of Earth–Orbiting Sensors, *Proc. SPIE*, 1938:100–108, 1993
- [33] Fries J., R. Böhl, and D. Oertel, Report on the Spectral Calibration of the DAIS–7915, DLR, IB 552–3/95, pp. 39, 1995
- [34] Gao B., and A.F.H. Goetz, Column Atmospheric Water Vapor and Vegetation Liquid Water Retrievals from Airborne Imaging Spectrometer Data, *J. Geophys. Res.*, 95(D4):3549–3564, 1990
- [35] GER, GER 3700: Highest Resolution, Photodiode & Photoconductor Array–Based Spectroradiometer, GER Corp., 1993
- [36] Goetz A.F.H., *Imaging Spectrometry for Earth Remote Sensing*, in: *Imaging Spectroscopy: Fundamentals and Prospective Applications*, eds. F. Toselli and J.

- Bodechtel, Kluwer Academic Publishers, pp. 1–20, 1992
- [37] Green R.O., J.E. Conel, J. Margolis, C. Chovit, and J. Faust, In-Flight Calibration and Validation of the Airborne Visible/Infrared Imaging Spectrometer (AVIRIS), *JPL Publication*, 96–4(1):115–126, 1996
- [38] Green R., Spectral Calibration Requirement for Earth-Looking Imaging Spectrometers in the Solar-Reflected Spectrum, *J. Opt. Soc. Am.*, 37(4):683–690, 1998
- [39] Grove C.I., S.J. Hook, and E.D. Paylor II, *Laboratory Reflectance Spectra of 160 Minerals, 0.4 to 2.5 Micrometers*, JPL Publication, 92–2, pp. 398, 1992
- [40] Guzman C.T., J.M. Palmer, P.N. Slater, C.J. Bruegge, and E.A. Miller, Requirements of a Solar Diffuser and Measurements of some Candidate Materials, *Proc. SPIE*, 1493:120–131, 1991
- [41] Haggett P., A.D. Cliff, and A. Frey, *Locational Analysis in Human Geography*, Edwards Arnold, London, pp. 605, 1977
- [42] Holecz F., *Postprocessing von SAR-Satellitenbilddaten, Remote Sensing Series*, Vol. 23, Dept. of Geography, University of Zürich, pp. 149, 1993
- [43] ISO, *Guide to the Expression of Uncertainty in Measurement*, Intl. Org. for Standardization, Switzerland, pp. 101, 1995
- [44] Itten K.I., M. Schaepman, L. De Vos, L. Hermans, H. Schlaepfer, and F. Droz, APEX–Airborne PRISM Experiment: A New Concept for an Airborne Imaging Spectrometer, in: *3rd Intl. Airborne Remote Sensing Conference and Exhibition*, Vol. 1, pp. 181–188, 1997
- [45] Jacobs S.F., *Nonimaging Detectors*, in: *Handbook of Optics*, ed. W.G. Driscoll, McGraw–Hill Inc., New York, pp. 4.1 – 4.69, 1978
- [46] Jahn H., and R. Reulke, *Systemtheoretische Grundlagen optoelektronischer Sensoren*, Akademie Verlag, Berlin, pp. 298, 1995
- [47] Kneubühler M., M. Schaepman, and T. Kellenberger, Comparison of Different Approaches of Selecting Endmembers to Classify Agricultural Land by Means of Hyperspectral Data (DAIS-7915), *Proc. IGARSS'98*, p. 4, 1998
- [48] Kneisys F.X., L.W. Abreu, G.P. Anderson, J.H. Chetwynd, E.P. Shettle, and A. Berk, *The MODTRAN 2/3 and LOWTRAN Model*, eds. L.W. Abreu and G.P. Anderson, Appendix C, Ontar Corporation, North Andover, MA, pp. 267, 1995
- [49] Koepke P., Vicarious Satellite Calibration in the Solar Spectral Range by Means of Calculated Radiances and its Application to Meteosat, *J. Opt. Soc. Am.*, 21:2845–2854, 1982
- [50] Kostkowski, H.J., *Reliable Spectroradiometry*, Spectroradiometry Consulting, La Plata, MA, pp. 609, 1997
- [51] Kraus K., and W. Schneider, *Fernerkundung: Physikalische Grundlagen und Aufnahmetechniken*, Vol. 1, Dümmler Verlag, pp. 158, 1988
- [52] Kruse F.A., G.L. Raines, and K. Watson, Analytical Techniques for Extracting Geologic Information from Multichannel Airborne Imaging Spectrometer Data, *Proc. Intl. Symp. Rem. Sens. Env.*, 4th Thematic Conf. on Rem. Sens. for Exploration Geology, pp. 309–324, 1985
- [53] Labsphere, Calibration Data: Reflectance Calibration Standards, Report–No.

- 13610–A, pp. 4, 1995
- [54] Labsphere, Integrating Sphere Theory and Applications, in: *Labsphere catalog*, Sphere Systems and Instrumentation, pp. 103–116, 1996
- [55] Meynart R., Radiometric Specifications for PRISM, ESA, EOOP Internal Paper, unpublished, pp. 10, 1994
- [56] Milton E.J., and A.F.H. Goetz, Atmospheric Influences on Field Spectrometry: Observed Relationships between Spectral Irradiance and the Variance in Spectral Reflectance, *Proc. 7th Intl. Symp. on Phys. Measurements and Signatures in Rem. Sens.*, Balkema, Vol. I, pp. 109–114, 1997
- [57] NASA, MODIS, <<http://ltpwww.gsfc.nasa.gov/MODIS/>>, 1998
- [58] Nee S.F., C. Yoo, T. Cole, and D. Burge, Characterization for Imperfect Polarizers under Imperfect Conditions, *J. Opt. Soc. Am. B*, 37(1):54–64, 1998
- [59] Nicodemus F.E., J.C. Richmond, and J.J. Hsia, *Geometrical Considerations and Nomenclature for Reflectance*, NBS Monograph 160, NBS, 1977
- [60] Noser G., Spektrale Charakterisierung von Weiden in der montanen Stufe anhand von DAIS 7915 Bildspetrometer–Daten, Master Thesis, Dept. of Geography, University of Zürich, unpublished, 1998
- [61] Oertel D., and B. Zhukov, On–ground Calibration Facility and Calibration Algorithms for Wide–angle Imaging and Videospectrometric Airborne Sensors in the VIS–TIR Spectral Range, DLR Forschungsbericht, DLR–FB 93–44, pp. 55, Ober-pfaffenhofen, 1993
- [62] Oertel D., The High Resolution Imaging Spectrometer DAIS: A Status Report, in: 2nd EARSEC Status Seminar, ed. A.J. Sieber, JRC, Ispra, 1994
- [63] Optronic, Operation Manuals OL450, Rev. D., Orlando, pp. 15, 1993
- [64] Optronic, Luminance and Color Temperature Calibration Certificate, Report–No. 902–844, pp. 9, 1994
- [65] Palmer C., *Diffraction Grating Handbook*, Milton Roy Company, 2nd Edition, New York, pp. 66, 1994
- [66] Palmer J.M., *The Measurement of Transmission, Absorption, Emission, and Reflection*, in: Handbook of Optics, ed. M. Bass, McGraw–Hill, Vol. II, pp. 25.1–25.25, 1995
- [67] Physics Department, Quantum Optics, <<http://www.physik.unizh.ch/groups/grouposterwalder/laser/>>, University of Zürich, 1998
- [68] Porter W.M., and H.T. Enmark, A System Overview of the Airborne Visible/Infrared Imaging Spectrometer (AVIRIS), *Proc. SPIE*, 834:22–31, 1987
- [69] Posselt W., P. Kunkel, E. Schmidt, U. Del Bello, and R. Meynart, Processes Research by an Imaging Space Mission, *Proc. SPIE*, 2957, 1996
- [70] Readings C.J., and M.L. Reynolds, *Land–Surface Processes and Interactions Mission*, ESA SP–1196(2), Noordwijk, pp. 86, 1996
- [71] Reulke N., R. Reulke, M. Schaepman, D. Schläpfer, P. Strobl, and A. Mueller, Combined Processing and Evaluation of Simultaneously Acquired Stereo and Hyperspectral Data, in: 3rd Intl. Airborne Remote Sensing Conference and Exhibition, ERIM, Vol. 2, pp. 329–336, 1997

- [72] Reulke N., R. Reulke, M. Schaepman, D. Schläpfer, P. Strobl, and A. Müller, Geometric Correction of Hyperspectral Scanner Data with Simultaneously acquired Stereo Data, in: *ISPRS*, Vol. 32, 3-4W2, 3D Reconstruction and Modeling of Topographic Objects, Stuttgart, pp. 9–14, 1997
- [73] Richter R, and F. Lehmann, MOMS-02 Sensor Simulation and Spectral Band Selection, *Int. J. Rem. Sens.*, 10(8):1429–1435, 1989
- [74] Richter R., Model SENSAT: A Tool for Evaluating the System Performance of Optical Sensors, *Proc. SPIE*, 1312:286–297, 1990
- [75] Richter R., Model Sensat-5—Sensor-Atmosphere-Target, DLR, IB 552-01/94, pp. 27, 1994
- [76] Richter R., A Spatially Adaptive Fast Atmospheric Correction Algorithm, *Intl. J. Rem. Sens.*, 17(6):1201–1214, 1996
- [77] Richter R., On the Inflight Absolute Calibration of High Spatial Resolution Spaceborne Sensors Using Small Ground Targets, *Intl. J. Rem. Sens.*, 18(13):2827–2833, 1997
- [78] Roberts D.A., Y. Yamaguchi, and R.J.P. Lyon, Calibration of Airborne Imaging Spectrometer Data to Percent Reflectance using Field Spectral Measurements, *Proc. 19th Intl. Symp. Rem. Sens. Env.*, 1985
- [79] Roberts D.A., Y. Yamaguchi, and R.J.P. Lyon, Comparison of Various Techniques for Calibration of AIS Data, *Proc. 2nd AIS Workshop*, JPL Publication, 86-35:21–30, 1985
- [80] Robinson B.F., and D.P. de Witt, *Electro-Optical Non-Imaging Sensors*, in: Manual of Remote Sensing, Am. Soc. of Phot., pp. 293–333, 1983
- [81] Rubin T., ed., *Calibration Guide from the First Intl. Airborne Imaging Spectrometer Calibration Workshop*, ASPRS, pp. 38, 1993
- [82] Sanders C.L., Accurate Measurements of and Corrections for Non-linearities in Radiometers, *J. Res. Natl. Bur. Stand.*, A76:437, 1972
- [83] Sandmeier S., W. Sandmeier, K.I. Itten, M.E. Schaepman, and T.W. Kellenberger, The Swiss Field-Goniometer System (FIGOS), in: *Proc. of IGARSS'95*, Firenze, Vol. III, pp. 2078-2080, 1995
- [84] Sandmeier S., W. Sandmeier, K.I. Itten, M.E. Schaepman, T.W. Kellenberger, Acquisition of Bidirectional Reflectance Data Using the Swiss Field-Goniometer System (FIGOS), in: *Proc. of EARSeL Symposium*, Basel, pp. 55–62, 1995
- [85] Sandmeier S., and W. Sandmeier, Prototypen für die Wissenschaft - Satellitenfernerkundung: Zusammenarbeit von Industrie und Forschung, Technische Rundschau Nr. 49, Hallwag Verlag, 1996
- [86] Sandmeier S., B. Hosgood, C. Müller, and G. Andreoli, Sensitivity Studies of Bidirectional Reflectance Data using the EGO/JRC Goniometer Facility, *Proc. 7th Intl. Symp. on Phys. Measurements and Signatures in Rem. Sens.*, Balkema, Vol. I, pp. 357–364, 1997
- [87] Santer R., X.F. Gu, G. Guyot, J. Deuze, C. Devaux, E. Vermote, and M. Verbrugghe, SPOT Calibration at the La Crau Test Site, *Rem. Sens. Env.*, 41:227–237, 1992
- [88] Santer R.P., C. Schmechtig, and K.J. Thome, BRDF and Surface-Surround Ef-

- fects on SPOT–HRV Vicarious Calibration, *Proc. EUROPTO*, 2960:344–354, 1996
- [89] Schaepman M., S. Sandmeier, K.I. Itten, P. Meyer, and T. Kellenberger, Spectral Signature Analysis Using a Field Goniometer Mounted Spectroradiometer, *1st Intl. Airborne Remote Sensing Conference*, ERIM, Strasbourg, 1994
- [90] Schaepman, M., P. Keller, D. Schläpfer, C. Cathomen, and K.I. Itten, Experimental Determination of Adjacency Effects over an Eutrophic Lake using a Helicopter mounted Spectroradiometer for the Correction of Imaging Spectrometer Data, in: *3rd Intl. Airborne Remote Sensing Conference and Exhibition*, ERIM, Vol. 2, pp. 497–504, 1997
- [91] Schaepman, M., D. Schläpfer, A. Müller, and P. Strobl, Ground Spectroradiometric Measurements in Support of the Validation of the Calibration of Airborne Imaging Spectrometer (DAIS 7915) Data, in: *3rd Intl. Airborne Remote Sensing Conference and Exhibition*, ERIM, Vol. 2, pp. 217–223, 1997
- [92] Schaepman M., sixs_multi.pl, <ftp://ftp.geo.unizh.ch/pub/schaep/sixs>, 1998
- [93] Schaepman M., M. Kneubühler, E. Meier, A. Mueller, P. Strobl, R. Reulke, and R. Horn, Fusion of Hyperspectral (DAIS 7915), Wide-angle (WAAC), and SAR (E-SAR) Data Acquisition Methods – The MultiSwiss'97 Campaign, *Proc. SPIE*, Vol. 3438, 1998
- [94] Schläpfer D., modo, ftp://ftp.geo.unizh.ch/pub/dschlapf/Mod_util, 1998
- [95] Schläpfer D., *Differential Absorption Methodology for Imaging Spectroscopy of Atmospheric Water Vapor*, Ph.D. Thesis, Dept. of Geography, University of Zürich, pp. 126, 1998
- [96] Schneider W.E., and D.G. Goebel, Standards for Calibration of Optical Radiation Measurement Systems, *Laser Focus/Electro–Optics*, Vol. 9, Orlando, pp. 5, 1984
- [97] Schneider W.E., Fundamentals of Measuring Optical Radiation, in: *Lasers & Optronics*, Orlando, pp. 4, 1993
- [98] Schowengerdt R.A., *Remote Sensing: Models and Methods for Image Processing*, 2nd ed., Academic Press, pp. 522, 1997
- [99] Shurcliff W.A., *Polarized Light—Production and Use*, Harvard Univ. Press, Cambridge, 1962
- [100] Slater P.N., *Remote Sensing, Optics and Optical Systems*, Addison–Wesley Publishing, pp. 575, 1980
- [101] Slater P.N., Variations In–flight Absolute Radiometric Calibration, *Proc. ISLSCP Conf.*, Rome, Italy, ESA, SP–248, 1986
- [102] Slater P.N., S.F. Biggar, R.G. Holm, R.D. Jackson, Y. Mao, M.S. Moran, J.M. Paler, and B. Yuan, Reflectance– and Radiance Based Methods for the In–flight Absolute Calibration of Multispectral Sensors, *Rem. Sens. Env.*, 22:11–37, 1987
- [103] Slater P.N., and S.F. Biggar, Suggestions for Radiometric Calibration Coefficient Generation, *J. Atm. & Oceanic Tech.*, 13:376–382, 1996
- [104] Snell J.F., *Radiometry and Photometry*, in: Handbook of Optics, ed. W.G. Driscoll, McGraw–Hill Inc., New York, pp. 1.1–1.29, 1978

- [105] Sokolowski J.K., K. Witcher, B.A. Davies, and R.O. Green, The Hyperspectral Imager aboard the SSTI's Lewis Spacecraft: A Comparison with AVIRIS, *JPL Publication*, 96-4(1):pp. 219-222, 1996
- [106] Springsteen A.W., A Guide to Reflectance Spectroscopy, Tech Guide, Labsphere, pp. 36, 1994
- [107] Springsteen A.W., Properties of Spectralon Reflectance Material, in: *Labsphere catalog*, Reflectance Standards and Targets, pp. 130-139, 1994
- [108] Springsteen A.W., J. Leland, and T. Ricker, A Guide to Reflectance Coatings and Materials, in: *Labsphere catalog*, Diffuse Reflectance Coatings and Materials, p. 32-56, 1996
- [109] Spyak P.R., and C. Lansard, Reflectance Properties of Pressed Aglofon F6: A Replacement Reflectance-Standard Material for Halon, *J. Opt. Soc. Am.*, 36(13):2963-2970, 1997
- [110] Staenz K., R.P. Gauthier, D.P. Witz, M.E. Schaepman and K.I. Itten, GER 3700 - A new array-based Instrument for Field Spectroscopy in the VNIR/SWIR Wavelength Regions, in: *Proc. of ISSSR*, Kauai, Hawaii, 1995
- [111] Strobl P., A. Mueller, D. Schläpfer, and M. Schaepman, Laboratory Calibration and Inflight Validation of the Digital Airborne Imaging Spectrometer DAIS 7915 for the 1996 Flight Season, *Proc. SPIE*, 3071:225-236, 1997
- [112] Strub G., Spektrometrische Untersuchungen an Wiesengesellschaften, Master Thesis, Dept. of Geography, University of Zürich, unpublished, 1998
- [113] Taylor B.N., and C.E. Kuyatt, Guidelines for Evaluating and Expressing the Uncertainty of NIST Measurements Results, NIST, TN 1297, pp. 20, 1994
- [114] Thome K.J., C.L. Gustafson-Bold, P.N. Slater, and W.H. Farrand, In-flight Radiometric Calibration of HYDICE using a Reflectance-Based Approach, *Proc. SPIE*, 2821:311-319, 1996
- [115] Vermote E., D. Tanré, J.L. Deuzé, M. Herman, and J.J. Morcette, *Second Simulation of the Satellite Signal in the Solar Spectrum*, 6S User Guide Version 0, NASA-Goddard Space Flight Center, Greenbelt, USA, pp. 182, 1994
- [116] Walker J.H., R.D. Saunders, K.D. Jackson, and D.A. McSparron, Spectral Irradiance Calibrations, NBS, Special Publication, 250-20, U.S. Govt. Printing Office, 1987
- [117] Walker J.H., R.D. Saunders, J.K. Jackson, and K.D. Mielenz, Results of a CCPR Intercomparison of Spectral Irradiance Measurements by National Laboratories, *J. Res. Natl. Inst. Stand. Technology*, 96(6):647-668, 1991
- [118] Walter-Shea E.A., C.J. Hays, M.A. Mesarch, and R.D. Jackson, An Improved Goniometer System for Calibrating Field Reference-Reflectance Panels, *Rem. Sens. Env.*, 43:131-138, 1993
- [119] Weidner V.R., and J.J. Hsia, Reflection Properties of Pressed Polytetrafluoroethylene Powder, *J. Opt. Soc. Am.*, 71(7):856-861, 1981
- [120] Weidner V.R., J.J. Hsia, and B. Adams, Laboratory Intercomparison Study of Pressed Polytetrafluoroethylene Powder Reflectance Standards, *J. Opt. Soc. Am.*, 24 (14):2225-2228, 1985
- [121] Witz D., Personal Communication, GER, Millbrook, NY, 1994-1998

- [122] Wolfe W.L., *Introduction to Imaging Spectrometers*, SPIE, TT25, pp. 148, 1997
- [123] Zalewski E.F., *Radiometry and Photometry*, in: Handbook of Optics, ed. M. Bass, McGraw-Hill Inc., Vol. II, pp. 24.1–24.51, 1995
- [124] Zissis G.J., and A.J. Larocca, *Optical Radiators and Sources*, in: Handbook of Optics, ed. W.G. Driscoll, McGraw-Hill Inc., New York, pp. 3.1–3.83, 1978

Acknowledgements

This work has been carried out with the support of scientists in our lab and from several other individuals working at different institutions.

My special thanks go to Prof. Dr. Klaus I. Itten, supervising this work between October 1993 and April 1998, and Dr. Konrad Schmid for continuous support. Many thanks go also to Prof. Dr. Harold Haefner, Prof. Dr. Kurt Brasel, and Prof. Dr. Robert Weibel for additional feedback on this work.

The laboratory measurement team supported me with hundreds of measurements and extensive laboratory experience—without their help, I would still be busy measuring something somewhere: Carli Cathomen, Stefan Dangel, Marcel Singer, and Gaby Noser.

It is impossible to compile a full list of people contributing to this work. Anyhow without the principal support of Sandra Rethage and everyone listed below, this might have taken another few years:

Christian Bachmann, Michael Berger, Peter Bitter, Guido Brandt, Frank Brazile, Ralph Brühlmann, Manuela Catalini, Tom Corl, Stefan Dangel, Ali Darvishsefat (and his family), Umberto Del Bello, Lieve De Vos, Corinna Dickhof, Fabien Droz, Cornel Ehrler, Fred Fischer, Joachim Hagger, Markus Heuer, Francesco Holecz, Stefan Imfeld, Johannes Keller, Peter Keller, Tobias Kellenberger (and his family), Mathias Kneubühler, Ivo Leiss, Martin Liechty, Peter Meyer, Andreas Müller (and certainly Wilma!), Christoph Müller, Markus Nolting, Daniel Nüesch, Dieter Oertel, Jens Piesbergen, Michael Rast, Götz Reinhäkel, Ralf Reulke, Irene Reutlinger, Rolf Richter, Tobi Rothfuss, Tod Rubin, Stefan Sandmeier, Daniel Schläpfer, Hansjörg Schläpfer, Barbla Schmid, Peti Schmid, Wolf Schweitzer, Marcel Singer, Fridolin Steinmann, Martin Steinmann, Karl Staenz, Peter Strobl, Gabi Strub, Andrej Vckovski, Martin Wagen, Bruno Weber, Thomas Werschlein, <blink>Caroline Westort</blink>, Othmar Wigger, Dennis Witz, and Peter Zurbrügg—Thank you all!

This page intentionally left blank.